Physik-Department E13
Technische Universität München

# Structure and Dynamics of Al and Ni Based Melts Studied by Inelastic Neutron Scattering

Suresh Mavila Chathoth

Vollständiger Abdruck der von der Fakultät für Physik der
Technischen Universität München zur Erlangung des akademischen
Grades eines
Doktors der Naturwissenschaften (Dr. rer. nat.)
genehmigten Dissertation.

Vorsitzender: Univ.-Prof. Dr. M. Kleber

Prüfer der Dissertation:
1. Univ.-Prof. (komm. L.) Dr. A. Meyer
2. Univ.-Prof. Chr. Pfleiderer, Ph. D.

Die Dissertation wurde am 19.05.2005 bei der Technischen Universität München eingereicht und durch die Fakultät für Physik am 30.06.2005 angenommen.

# Summary

Microscopic dynamics in dense metallic liquids and liquid alloys with chemical short-range order has been investigated by the inelastic neutron scattering technique. Dense metallic liquids are characterized by a high packing fraction that exceeds 0.5 at their melting points. On the other hand, thermophysical and thermodynamic properties of liquid alloys that exhibit chemical short-range order behave the same way as in a highly non ideal solution.

The present study is an attempt to understand (1) the mixing behavior on the microscopic dynamics in dense hard-sphere like systems and (2) the influence of the chemical short-range order on the atomic diffusion. The systems studied are dense liquid Ni and glass forming NiP, PdNiP and PdNiCuP melts as well as liquid Al-Ni alloys, in the concentration range 25 to 90 atomic percent of Al, that display an intermediate-range order.

The alloys were prepared by arc melting and induction melting techniques. The prepared alloys are then characterized by differential scanning calorimetry (DSC). The DSC measurements on glass forming alloys show different thermodynamic properties. In these alloys the increasing number of components lead to a continuous decrease of the liquidus temperature and the critical cooling rate for the glass formation. The microscopic dynamics in these liquids is in good agreement with the Mode Coupling theory of the liquid-to-glass transition. The Ni diffusivities are derived from the $q^2$ dependence of the mean relaxation time $1/\langle\tau_q\rangle$, and this dependence is found to hold even at intermediate $q$ values. At a given temperature the observed Ni self-diffusivities are similar, irrespective of the alloy compositions. These results show that in hard-sphere like dense liquids packing fraction dominate in the mass transport process.

The Al-Ni melts were investigated as a function of composition and temperature by inelastic neutron scattering techniques. The chemical short range order (CRSO) present in the melts is visible through a prepeak in the structure factor. With increasing Ni content, the prepeak intensity is increasing and its maximum is shifting towards higher $q$ values in Al rich side of Al-Ni composition. The measured Ni self-diffusivities as a function of composition exhibit a non-linear dependence. The Ni self-diffusivities show a pronounced increase with increasing Al content only on the

Al rich side, while the Ni self-diffusivity remains constant on the Ni rich side. The non-linear dependence of Ni self-diffusivities is due to the change in the packing fraction which is in turn changes with CSRO while increasing the Al content. Ni rich A-Ni alloys exhibit a dense packing of atoms similar to pure Ni. The self diffusivities are equal within error bars.

An investigation of microscopic dynamics in hard-sphere like dense metallic liquids and liquid alloys with CSRO indicate that the packing fraction is the major governing factor in determining the self-diffusion in liquids.

# Zusammenfassung

Die mikroskopische Dynamik von dichten metallischen Flüssigkeiten als auch von flüssigen Legierungen, welche eine chemische Nahordnung der Atome zeigen, wurde mittels inelastischer Neutronenstreuung untersucht. Die dichten metallischen Flüssigkeiten sind am Schmelzpunkt durch Packungsdichten grösser als 0.5 ausgezeichnet. In flüssigen Legierungen mit chemischer Nahordnung verhalten sich die thermophysikalischen und thermodynamischen Eigenschaften in hohem Grade wie die nicht idealer Flüssigkeiten.

Die vorliegende Arbeit soll zwei Punkte näher beleuchten und zu einem weiterführenden Verständnis derselben führen: (1) Einfluss des Mischungsverhaltens auf die mikroskopische Dynamik hartkugelähnlicher dichter Flüssigkeiten. (2) Einfluss der chemischen Nahordnung auf die atomare Diffusion. Dazu wurde flüssiges Ni und die glasbildenden metallischen Schmelzen NiP, PdNiP und PdNiCuP untersucht. Die zweite Frage nach dem Einfluss chemischer Nahordnung wird anhand von AlNi Legierungen in einen Konzentrationsbereich von 25% Al bis 90% Al gezeigt.

Die Proben wurden im Lichtbogen und mittels induktivem Aufschmelzens hergestellt. Die Legierungen wurden anschliessend mittels differentieller Wärmeflussmessungen charakterisiert. Aus den Wärmeflussmessungen kann gezeigt werden, dass die glasbildenden Verbindungen unterschiedliche thermodynamische Eigenschaften besitzen. Mit steigender Anzahl der Komponenten nimmt die Temperatur des Liquidus stetig ab. Gleichzeitig sinkt die kritische Kühlrate für Glasbildung. Es wird gezeigt, dass die mikroskopische Dynamik dieser Systeme im Rahmen der Modenkopplungstheorie des Flüssig-Glas-Übergangs beschrieben werden kann. Selbstdiffusionskoeffizienten für Nickel werden im hydrodynamischen Limes aus der $q^2$ Skalierung der Relaxationsrate $1/\langle\tau_q\rangle$ bestimmt. Für die dichten Metallschmelzen wird gezeigt, dass diese Abhängigkeit auch bei Wellenzahlen gilt, die intermediären Längenskalen entsprechen. In den mehrkomponentigen massivglasbildenden Legierungen ohne chemische Nahordnung werden bei derselben Temperatur gleiche Diffusionskonstanten für Ni beobachtet. Dies bestätigt, dass in dichten hartkugelähnlichen Flüssigkeiten Massentransport durch die Packungsdichte bestimmt wird.

AlNi Schmelzen weisen im Gegensatz zu reinem Ni und den untersuchten mehrkomponentigen Massivglasbildnern chemische Nahordnung auf. Die chemische Nahordnung manifestiert sich experimentell in einem Prepeak im Strukturfaktor bei Wellenzahlen kleiner als der Wellenzahl, die Abstände benachbarter Atome aufzeigt. Die chemische Nahordung und deren Auswirkung auf mikroskopische Transportprozesse über einen weiten Temperatur und Ni Konzentrationsbereich wurden untersucht. Mit zunehmender Ni Konzentration nimmt der Prepeak ab. Auf der Al reichen Seite schiebt das Maximum des Prepeaks zu größeren Wellenzahlen. Die über die Neutronenstreuung ermittelten Ni Selbstdiffusionskoeffizienten verhalten sich nicht-linear mit der Zusammensetzung. Auf der Ni reichen Seite bleiben die Selbstdiffusionskoeffizienten annähernd konstant. Auf der Al reichen Seite wird die Ni Selbstdiffusion mit steigendem Al Anteil schneller. Die Packungsdichte in AlNi Schmelzen ändert sich, beeinflusst durch die chemische Nahordnung mit der Ni Konzentration. Dies erklärt das nicht-lineare Verhalten der Ni Selbstdiffusion. Auf der Ni reichen Seite bleibt die Packungsdichte konstant. Sie korrespondiert mit der Packungsdichte von dichtgepacktem reinen Nickel. Die Ni Selbstdiffusion ändert sich nicht.

Die Untersuchungen der mikroskopischen Dynamik in einfachen und mehrkomponentigen dichten Flüssigkeiten, sowie Flüssigkeiten mit chemischer Nahordnung zeigen, dass Transportprozesse in metallischen Flüssigkeiten im hohen Mass durch die Packungsdichte bestimmt werden.

# Contents

**1 Introduction** **1**

1.1 Metallic alloys . . . . . . . . . . . . . . . . . . . . . . . . . . . . 1

1.2 Structure and diffusion . . . . . . . . . . . . . . . . . . . . . . . . 2

1.3 Present work . . . . . . . . . . . . . . . . . . . . . . . . . . . . . 4

**2 Liquid metals and alloys** **7**

2.1 General properties . . . . . . . . . . . . . . . . . . . . . . . . . 7

2.1.1 Structure . . . . . . . . . . . . . . . . . . . . . . . . . 7

2.1.2 Density . . . . . . . . . . . . . . . . . . . . . . . . . . 9

2.1.3 Viscosity . . . . . . . . . . . . . . . . . . . . . . . . . 12

2.2 Theoretical aspects of diffusion . . . . . . . . . . . . . . . . . . . 16

2.2.1 Chemical or mutual diffusion . . . . . . . . . . . . . . . 16

2.2.2 Self-diffusion or random walk . . . . . . . . . . . . . . . 17

2.2.3 Diffusion based on hard sphere models . . . . . . . . . . . 18

2.2.4 Corresponding state principle . . . . . . . . . . . . . . . 19

2.2.5 Free volume theory . . . . . . . . . . . . . . . . . . . . 20

2.2.6 Diffusion in liquid alloys . . . . . . . . . . . . . . . . . . 20

2.3 Mode-coupling theory (MCT) . . . . . . . . . . . . . . . . . . . 21

2.4 Molecular dynamics simulation . . . . . . . . . . . . . . . . . . . 26

**3 Sample preparation and characterization** **29**

3.1 Sample materials . . . . . . . . . . . . . . . . . . . . . . . . . . 29

3.2 Arc melting . . . . . . . . . . . . . . . . . . . . . . . . . . . . . 29

3.3 Induction melting . . . . . . . . . . . . . . . . . . . . . . . . . . 30

3.4 Melt spinning . . . . . . . . . . . . . . . . . . . . . . . . . . . . 31

3.5 Differential scanning calorimetry . . . . . . . . . . . . . . . . . . 31

3.6 Sample holder . . . . . . . . . . . . . . . . . . . . . . . . . . . . 34

**4 Inelastic neutron scattering** **37**

4.1 Introduction . . . . . . . . . . . . . . . . . . . . . . . . . . . . . 37

4.2 Neutron scattering - Theory . . . . . . . . . . . . . . . . . . . . . 37

4.2.1 Diffusive motion . . . 39
4.3 Time-of-flight spectroscopy . . . 40
4.4 Experiments at IN6 and FOCUS . . . 41
4.4.1 Neutron wavelength . . . 43
4.4.2 Sample environment . . . 44
4.4.3 The samples . . . 44

**5 Data reduction 47**
5.1 Raw data reduction . . . 47
5.2 Self-absorption correction . . . 50
5.3 Quasielastic structure factor . . . 51
5.4 Self-diffusion coefficient . . . 52

**6 Dynamics in dense metallic liquids 55**
6.1 Introduction . . . 55
6.2 Thermophysical properties . . . 56
6.2.1 Density . . . 56
6.2.2 Viscosity . . . 57
6.3 Thermodynamic properties . . . 57
6.4 Microscopic dynamics . . . 58
6.4.1 Scattering law . . . 58
6.4.2 Phonons . . . 59
6.4.3 Structural relaxation . . . 60
6.4.4 Self-diffusion . . . 62
6.5 Atomic transport mechanism . . . 65
6.6 Entropy and self-diffusion . . . 67

**7 Dynamics in liquids with CSRO 69**
7.1 Chemical short range order (CSRO) . . . 69
7.2 Al-Ni phase diagram . . . 69
7.3 Density and viscosity of Al-Ni melts . . . 70
7.4 Structure of Al-Ni melts . . . 72
7.5 Composition dependence of CSRO . . . 73
7.6 Microscopic dynamics . . . 77
7.7 Atomic transport . . . 77
7.8 Al-Ni and Al-Cu melts . . . 79
7.9 Al-Ni and Al-Ni-Ce melts . . . 80

**8 Conclusions 83**
8.1 Microscopic dynamics in dense liquids . . . 83
8.2 Dynamics in melts with CSRO . . . 85

8.3 Future prospects . . . . . . . . . . . . . . . . . . . . . . . . . . . . 86

**A Alphabetic list of quantities and abbreviation 89**

**B List of neutron scattering experiments 91**

**C Ni self-diffusion in dense metallic melts 93**

**D Ni self-diffusion in Al-Ni, Al-Cu and Al-Ni-Ce melts 95**

**E Acknowledgments 97**

**F Publications 99**

# List of Figures

2.1 The radial distribution function of liquid Sodium at near to the melting point [Wa75]. . . . . . . . . . . . . . . . . . . . . . . . . . . . 8

2.2 The structure factor of liquid Sodium close to the melting point [Wa75]. 9

2.3 Relaxation in liquids, a schematic plot of $\Phi(q,t)$ versus $\log(t)$. $\Phi(q,t)$ shows two step relaxation in viscous liquids, a fast $\beta$ relaxation and a slow $\alpha$ relaxation. . . . . . . . . . . . . . . . . . . . . . . . . . . 23

3.1 This picture shows the inside of an arc melting chamber. A needle pointing down is the W anode used to generate the arc and beneath is the Cu cathode with provisions to keep the elements. Different geometries of these slots are used to make samples with different shapes. . . . . . . . . . . . . . . . . . . . . . . . . . . . . . . . . 30

3.2 This figure shows induction melting of $Pd_{43}Ni_{10}Cu_{27}P_{20}$ sample. The induction coil (made of copper) and melting of the sample inside the quartz tube are also seen. The white patches inside the quartz is $B_2O_3$. 31

3.3 The melt spin process: The alloy is induction melted in a quartz tube and injected on a Cu disc using highly purified Argon. The disc and quartz tube are kept inside in a He filled chamber. The melts come out from the disc in the forms of ribbons. . . . . . . . . . . . . . . . 32

3.4 The DSC scan of $Al_{90}Ni_{10}$. It shows exothermic liquidus temperature $T_{liq}$ at 1033 K and is in excellent agreement with the phase diagram. The peak on cooling shows the endothermic recrystallization temperature. . . . . . . . . . . . . . . . . . . . . . . . . . . . . . . . . 33

3.5 [A]The characteristic temperatures of $Pd_{43}Ni_{10}Cu_{27}P_{20}$ metallic glass shows the glass transition temperature, $T_g$ at 578 K, a sharp crystallization peak at 671 K and a liquidus temperature at 883 K. [B] The heat flow characteristic between $T_x$ and $T_{liq}$ change drastically because of a small variation in the Phosphorus content. . . . . . . . . 33

3.6 The sample holder used for neuron scattering experiments. It is made of alumina($Al_2O_3$) and has the shape of a hollow cylinder. The sample filling area is the region between the inner and outer cylinders. . . . . 35

3.7 The interface between the $Al_2O_3$ sample holder and the $Al_{80}Ni_{20}$ sample after the experiment investigated by a microscope (magnification = 5X). A clean interface indicates that there is no reaction between the sample and $Al_2O_3$ at high temperatures. . . . . . . . . . . . . . . 35

4.1 Inelastic neutron scattering spectra: a sharp elastic peak and broad peak at smaller time of flight shows that neutrons gained energy from phonons. The elastic peak is broadened ($Al_{70}Ni_{30}$ = 1795 K) due to quasielastic contributions from diffusive motions. . . . . . . . . . . . 39

4.2 An over view of time and space covered by various time of flight neutron scattering techniques (source: NIST neutron scattering center). 42

4.3 Schematic of IN6 at ILL, Grenoble . . . . . . . . . . . . . . . . . . . 43

4.4 The $q$-$\omega$ domain of the ILL time-of-flight spectrometer IN6 at a wavelength 5.1 Å. . . . . . . . . . . . . . . . . . . . . . . . . . . . . . 44

5.1 Shows the time of flight spectrum of $Al_{70}Ni_{30}$ and that of Alumina sample container. The sharp peak at 1.3 ms $m^{-1}$ is the elastic peak. The wavelength $\lambda = 5.1$ Å. . . . . . . . . . . . . . . . . . . . . . . 48

5.2 A Bragg peak from the sample container at $2\theta = 95°$. The blue spectrum is the sample plus container and the green is that of the sample container only. . . . . . . . . . . . . . . . . . . . . . . . . . 50

5.3 $A_{S,SC}(\omega)$ for $Al_{90}Ni_{10}$ at a scattering angle $2\theta = 80^0$ versus energy transfer $\hbar\omega$. . . . . . . . . . . . . . . . . . . . . . . . . . . . . 51

5.4 $S(q,\omega)$ for $Pd_{43}Ni_{10}Cu_{27}P_{20}$. The room temperature indicate the instrumental energy resolution. At high temperature the spectra are broadened due to quasielastic contributions from the diffusive motion of atoms . . . . . . . . . . . . . . . . . . . . . . . . . . . . . . . 52

5.5 Quasielastic structure factors of $Al_{70}Ni_{30}$ and $Pd_{43}Ni_{10}Cu_{27}P_{20}$ melts at 1795 K. . . . . . . . . . . . . . . . . . . . . . . . . . . . . . 52

5.6 The figure shows the intermediate scattering function. The red curve is the instrumental energy resolution function measured at 300 K. . . 53

5.7 The figure shows the density correlation function $\Phi(q,t)$ of $Pd_{40}Ni_{40}P_{20}$ and $Al_{80}Ni_{20}$ at different temperatures fitted with the exponential function. . . . . . . . . . . . . . . . . . . . . . . . . . . . . . . 54

5.8 The figure shows the inverse of mean relaxation time $\langle\tau_q\rangle$ plotted against $q^2$. The data points are fitted with straight line and the slope of the line gives the self-diffusion coefficient $D$. . . . . . . . . . . . . 54

6.1 Scattering law $S(q,\omega)$ of liquid $Pd_{43}Ni_{10}Cu_{27}P_{20}$ obtained from IN6 neutron time of flight spectrometer. The data at 300 K represent the instrumental energy resolution. Measurement at higher temperatures show a broad quasielastic signal. . . . . . . . . . . . . . . . . . . . . . . 59

6.2 Vibrational density of states $g(\omega)$ representing mainly Ni and Cu vibrations in liquid $Pd_{43}Ni_{10}Cu_{27}P_{20}$. The maximum of $g(\omega)$ around 17 meV corresponds to 0.04 ps. The vibrations are fairly separated from relaxational dynamics above 1 ps and also exhibits a weak temperature dependence [Me02]. . . . . . . . . . . . . . . . . . . . . . . . . 59

6.3 Self correlation function $S(q,t)$ of liquid Ni at different $q$ values as obtained by Fourier transform of $S(q,\omega)$ and deconvolution with instrumental energy resolution. Structural relaxation causes the finial decay of $S(q,t)$. The data are fitted with an exponential function . . 60

6.4 Normalized density correlation function $\Phi(q,t)$ of liquid $Pd_{40}Ni_{40}P_{20}$ at $0.97\text{Å}^{-1}$. The data points are fitted with stretched exponential function. [Eq. (2.53)]. . . . . . . . . . . . . . . . . . . . . . . . . 61

6.5 The rescaled density correlation function in the $\alpha$ relaxation regime (for $t > 1$ ps). All the data in the structural relaxation fall into a single master curve: a time temperature superposition of structural relaxation holds. The lines are fitted with a stretched exponential function [Eq 2.53] with $\beta = 0.75\pm0.02$. . . . . . . . . . . . . . . . . . 61

6.6 The mean relaxation time $\langle\tau_q\rangle$ is plotted against $q$. The straight line is a power law fit $\langle\tau_q\rangle \propto q^{-n}$, with $n = 2$. . . . . . . . . . . . . . . . 62

6.7 The inverse of mean relaxation time $\langle\tau\rangle$ is plotted against $q^2$. The straight line is a power law fit $1/\langle\tau_q\rangle \propto q^2$ and the slope of the line gives the self-diffusion constant $D(T)$. . . . . . . . . . . . . . . . . . . . 63

6.8 Ni self-diffusivity in the liquids Ni, $Ni_{80}P_{20}$, $Pd_{40}Ni_{40}P_{20}$ and $Pd_{43}Ni_{10}Cu_{27}P_{20}$ in a semilogarithmic plot, over 1000 degrees. Irrespective of the liquid composition and thermodynamic properties, the Ni self-diffusivites are similar within 20% . . . . . . . . . . . . . . . . . . . . . . . . . 64

6.9 Atomic transport in Ni, NiP, PdNiP and PdNiCuP melts: At high temperatures diffusivities are similar to the diffusivities in liquid Sn and Na close to their melting temperature $T_m$ [Me02, Zo03]. . . . . . 66

7.1 Al-Ni phase digram: The blue marks indicate the composition and temperature chosen for investigating the microscopic dynamics. . . . 70

7.2 The red diamonds indicate the density [Ay69] and the blue squares, the molar volume calculated from the density data of Al-Ni melts at 1795 K, respectively. The open diamond represent the sample is in the crystalline state. . . . . . . . . . . . . . . . . . . . . . . . . . . 71

7.3 The viscosity of Al-Ni melts as function of Ni content as reported by Petrushevskii *et. al.* [Pe71]. . . . . . . . . . . . . . . . . . . . . . . . . 71

7.4 (a) The structure factors of $Al_{80}Ni_{20}$ observed by Maret *et. al.* in the neutron diffraction experiments. (b) The Bhatia-Thornton (BT) partial structure factors for liquid $Al_{80}Ni_{20}$ [Ma90]. . . . . . . . . . . 72

7.5 $S_{quel\_coh}$ quasielastic structure factor obtained from time of flight neutron scattering. The prepeak shows increasing intensity with increasing Ni content. . . . . . . . . . . . . . . . . . . . . . . . . . . . . . 73

7.6 Structure factor $S_n(q)$ of Al-Ni melts as calculated from the partial structure factors of the simulation weighted with neutron scattering lengths. Inset: Atomic volume from the simulation compared to the experimental data as a function of composition [Da04]. . . . . . . . . 74

7.7 Partial structure factors (a) $S_{AlAl}(q)$, (b) $S_{AlNi}(q)$ (c)$S_{NiNi}(q)$ of Al-Ni melts obtained from the simulation at 1525 K [Da04]. . . . . . . . 75

7.8 Pair correlation function $g_{\alpha\beta}(r)$ of Al-Ni melts as obtained from the simulation. . . . . . . . . . . . . . . . . . . . . . . . . . . . . . . . 76

7.9 The $1/q^2$ dependence of mean relaxation time $\langle\tau_q\rangle$ in $Al_{90}Ni_{10}$ and in $Ni_3Al$ melts. As compared to dense liquids, the $q^2$ dependence deviates at smaller $q$ values. But in $Ni_3Al$ the deviation is comparatively at larger $q$ value. . . . . . . . . . . . . . . . . . . . . . . . . . . . 77

7.10 Ni self-diffusion in Al-Ni melts at 1795 K and 1525 K observed by neutron scattering and calculated from viscosity data [Pe71, Ya93]. . 78

7.11 A comparison of Ni self-diffusion in Al-Ni melts at 1795 K and 1525 K observed by neutron scattering and MD simulation [Da04]. . . . . . 79

7.12 A snapshot of $Al_{80}Ni_{20}$ from the MD simulation at 1750 K. The blue spheres represent Ni atoms and green one the Al atoms. It is clear from the figure that the atoms are not distributed randomly because of the CSRO. . . . . . . . . . . . . . . . . . . . . . . . . . . . . . . 80

7.13 The quasielastic structure factor of $Al_{80}Ni_{20}$ and $Al_{80}Cu_{20}$ melts at 1525 K. . . . . . . . . . . . . . . . . . . . . . . . . . . . . . . . . 81

7.14 Activation energy for Ni self-diffusion in $Al_{80}Ni_{20}$ $E_{Ni} = 35.15\pm0.15$kJ mol$^{-1}$ and for Cu self-diffusion in $Al_{80}Cu_{20}$ melts $E_{Cu} = 33.28\pm0.12$kJ mol$^{-1}$. . . . . . . . . . . . . . . . . . . . . . . . . . . . . . . . 81

7.15 Ni self-diffusivities in Al-Ni melts (red squares) and in Al-Ni-Ce melts. Ni self-diffusiviy decreases with increasing Ce content. . . . . . . . . 82

8.1 The experimental setup for the levitated neutron scattering techniques. A bright spot in the figure shows the levitated Ni droplet in a He filled chamber. . . . . . . . . . . . . . . . . . . . . . . . . . 86

8.2 Results of neutron scattering on a levitated undercooled liquid Ni. The Ni self-diffusivity obtained from fitting the data points with a Lorentzian function and by the formula $D = \Gamma/2\hbar q^2$ was found to be $2{\pm}1 \times 10^{-9}\mathrm{m}^2\mathrm{s}^{-1}$ at 1577 K. . . . . . . . . . . . . . . . . . . . . . . . . 87

# List of Tables

2.1 Self-diffusion coefficient $D$ from the equation 2.30 and experiments. The results show that the values of $D$ agree well with the experimental ones for simple liquid metals. . . . . . . . . . . . . . . . . . . . . . . . 19

3.1 Transition temperatures of alloys observed by differential scanning calorimetry. . . . . . . . . . . . . . . . . . . . . . . . . . . . . . . . . 34

4.1 Neutron coherent $\sigma_{coh}$, incoherent scattering cross sections $\sigma_{inc}$ and absorption cross sections $\sigma_{abs}$ of elements [Be88]. . . . . . . . . . . . . 45

6.1 The packing fraction of the alloy liquids just above the liquidus temperatures calculated from the density data by equation 2.5. . . . . . . 57
6.2 Viscosity of the liquid alloys at some temperature of interest. . . . . . 57
6.3 Thermodynamic properties of liquid Ni and the alloys obtained from DSC measurements and reported in [Lu99] . . . . . . . . . . . . . . . 58
6.4 Ni self-diffusivities obtained from the inelastic neutron scattering and those calculated from the viscosity data via Stokes-Einstein relation. . 65

7.1 Activation energy for Ni self-diffusion in Al-Ni melts . . . . . . . . . . 79
7.2 Activation energy for Ni self-diffusion in Al-Ni-Ce melts . . . . . . . . 82

# Chapter 1

# Introduction

*Summary : The motivation and outline of the present thesis work are discussed in this chapter*

## 1.1 Metallic alloys

The progress of science and technology is inevitably related to the development of new materials. Bulk amorphous metallic alloys (metallic glasses) [In01, Jo99, Ma95] are such a category of materials which have attracted scientists and technologists for the past three decades, during which these materials passed from being of basic research interest to the status of practical materials for industrial applications. This is because of their excellent combination of mechanical properties resulting from their disordered structure. For example, the Zr-based bulk metallic glass exhibits an extremely high tensile strength which is about two times higher than that of crystalline alloys [Pe93]. Some of the amorphous alloys are exceptionally corrosion resistant and behave as very soft magnetic materials [Ma95].

The realization of metallic amorphous alloys by very low cooling rates, comparable to those of oxide glasses, have been a long-cherished desire of material scientists. This aim was realized at the beginning of the nineties by the discovery of new families of multicomponent glass forming alloys such as Pd-Ni-Cu-P, Zr-Ni-Al-Cu, and Zr-Ti-Cu-Ni-Be. These alloys show a high thermal stability of their supercooled liquid state when heated above calorimetric glass transition temperature $T_g$. Moreover, cooling rates as low as 1 to 100 K $s^{-1}$ are sufficient to reach high levels of undercooling. Consequently, it becomes possible to produce bulk samples of about 90 mm (cm class) size by conventional casting processes. This has opened a new era for amorphous alloys because now one can overcome earlier limitations of shape and size which have been the most serious disadvantages for a broader use of these alloys.

These new bulk amorphous alloys are excellent advanced engineering materials due to their excellent wear properties, low coefficient of friction and high corrosion resistance. Viscosities in the range of $10^7$ to $10^8$ poise can be reached in the undercooled region below the crystallization temperature $T_x$. Therefore they can be easily deformed by pressing, drawing and blowing, processes known for the working of oxide glasses. Furthermore, the high thermal stability of these alloys makes for the first time possible a detailed exploration of the kinetics, thermodynamics and microscopic dynamics in the supercooled region, up to glass the transition temperature $T_g$.

On the other hand, the bulk properties of crystalline alloys originate from their microscopic structure. A basic understanding how the microscopic structure develops during solidification is important for developing alloys that have a better performance. The knowledge of intermediate structure and dynamics in the liquid state are essential to understand the underlying solidification process. For example, to perform a reliable simulation on the solidification processes of metallic alloys, an accurate self-diffusion coefficient in the liquid state is an important input parameter [La86].

Al-Ni based superalloys are used in load-bearing structures to the highest homologous temperature of any common alloy system (90% of their melting point). Among the most demanding applications for such materials are those in the hot sections of turbine engines. The pre-eminence of superalloys is reflected in the fact that they currently comprise over 50% of the weight of advanced aircraft engines. The widespread use of superalloys in turbine engines coupled with the fact that the thermodynamic efficiency of turbine engines increases with increasing turbine inlet temperatures. This has, in part, provided the motivation for increasing the maximum operational temperature of superalloys. In fact, during the past 30 years the turbine airfoil temperature capability has increased on average by about 5 degrees per year. The operational temperature increase by more than 40% has benefited from material improvements.

A continuing research and better understanding of the microscopic structure formation and the atomic transport mechanism contributes significantly to the development of such materials [Su72].

## 1.2 Structure and diffusion

The atomic transport mechanism in simple expanded metallic liquids at high temperatures is well understood [Kr87]. Microscopically, transport in the hydrodynamic regime is governed by uncorrelated binary collisions of atoms. All atoms contribute continuously to the mean square displacement, and the diffusion takes place via viscous flow, as described by the Stokes-Einstein relation. This hard-sphere collision picture is applicable at low to moderate densities [Ra83, Le91]. However, as the density increases, even in simple hard-sphere like systems, the real particle dynamics are more complicated and controlled by complex correlations and collisions.

Additionally, the hard-sphere collisions ruling the particle motion depends on the thermodynamic state of the liquid, and the density dependence of the transport coefficients deviates considerably from the prediction of hard-sphere collision models. For example, a qusielastic neutron scattering study on liquid Sodium (Na) shows that the particle dynamics at low density *i.e* at high temperature (1773 K) can well described by binary collision picture as predicted by simple hard-sphere theory [Ch39]. But as density increases the Na self-diffusivity considarably deviate from this theoretical predictions [Pi03]. The density of the liquid Sodium varies only 0.98 g cm$^3$ at 371 K ($T_m$) to 0.58 g cm$^3$ at 1773 K. Kinetic models predict a temperature dependence of the type $D \propto T^n$, where $n$ is found to be close to 2 according to molecular-dynamic simulations and neutron-scattering experiments [Fr97, Wi93].

A better understanding of underlying microscopic process was achieved by the development of the mode-coupling theory (MCT) [Go92]. In simple liquids, where the diffusion takes place within the binary collision process, the temperature dependence of diffusivity can be well described by the $D \propto T^n$ law. In dense liquids the concept of binary collisions no longer applies. Instead there is a tendency towards localization of atoms in a metastable state. Upon cooling the liquid viscosity increases continuously, and the atoms become more and more trapped in their nearest-neighbor "cages" for times much longer than the vibration time. The MCT predicts that this cage effect leads to a freezing of the viscous flow at a critical packing fraction $\varphi_c$ or a critical temperature $T_c$ and the atomic transport mechanism changes from liquid like flow to glass like hopping. The diffusivities obey a power law dependence $D \propto [(T - T_c)/T_c]^\gamma$.

The recent neutron scattering [Me02] and tracer diffusion[Zo03] studies in dense PdNiCuP alloy shows that the transport mechanism above $T_c$ is highly collective and the temperature dependence of the transport coefficients are in good agreement with the $\tau$ scaling law of the mode coupling theory. Below $T_c$, the diffusivities decouple from the viscous flow and shows an Arrhenius temperature dependence.

The alloy that has attracted perhaps the greatest interest in the view point of diffusion is the five component alloy $Zr_{46.7}Ti_{8.2}Cu_{7.5}Ni_{10}Be_{27.5}$, also known as Vitreloy 4. The temperature dependence of diffusion in Vitreloy 4 has been measured for a variety of elements, including Be [Re01], B [Fi99], Fe [Fi99], Ni [Me03, Ko99, Ko00], Co [Eh99], Al [Bu97], Zr [Ko00] and Hf [Zu01]. An important observation is that the diffusivities of several elements exhibit a "non-linear" Arrhenius behavior. A similar break in the Arrhenius diagram is also found in several other bulk metallic glasses [Me02, Fr03].

In Zr-based bulk glass forming alloy melts, $Zr_{41.2}Ti_{13.8}Cu_{12.5}$ $Ni_{10}Be_{22.5}$(V1) and $Zr_{46.8}Ti_{8.2}Cu_{7.5}Ni_{10}Be_{27.5}$(V4) it was reported that the viscosity differs up to two orders of magnitude. The diffusivities decoupled from the viscous flow and show similar Ni and Ti mobilities in these two alloy liquids well above its liquidus temperatures [Me03]. It is an open question whether the smaller atoms which move faster in an relatively immobile Zr matrix might be the reason for these results. Zr based bulk glass forming alloys are well known for their glass forming ability and are characterized by a high packing density. The microscopic dynamics in these melts are in accordance with the MCT of the liquid to glass transition [Me98].

## 1.3 Present work

This thesis work aims on elucidating the following two aspects of atomic transport in metallic liquids:

- The effect of composition and hence the thermodynamic properties on structural relaxation and self-diffusion in dense metallic liquids.
- Influence of chemical short range order (CSRO) on atomic self-diffusion in metallic liquids.

The microscopic dynamics of dense glass forming metallic liquids can be well described by the MCT [Me98, Me99, Me02, Me03, Zo03]. However, it is still not explored experimentally, how the dynamics in dense glass forming metallic liquids changes with varying composition. What is the effect of thermodynamics on the self-diffusion in dense metallic liquids?. To understand the effect of composition and thermodynamic properties on the microscopic dynamics in dense metallic liquids we have investigated Ni self-diffusivities in Ni, NiP, PdNiP and PdNiCuP above their liquidus temperatures. Pure Ni and the dense glass forming alloys, NiP, PdNiP and PdNiCuP are characterized by different thermodynamic properties. For example, the liquidus temperature changes from 1726 K for pure Ni to 863 K for $Pd_{43}Ni_{10}Cu_{27}P_{20}$ and melting enthalpy of pure Ni is 17.2±0.51 KJ/mol but it is only 7.01±0.04 KJ/mol for the four component melt. Liquid Ni and glass forming melts exhibit similar packing fractions and is as high as 0.50 at their respective melting temperatures.

In alloy melts like Al-Ni, Al-Mn [Ma90], Al-Fe [Ji98, Il02], and glass forming Al rich alloys [Li99], the structure distinctly deviates from random hard-sphere packing and exhibits a chemical short range order (CSRO). It appears as a pre-peak in its structure factor. The CSRO causes anomalies in the composition dependence of the thermodynamic and thermophysical properties like enthalpy of mixing, chemical activity, entropy, atomic volume and viscosity. These are characteristic for highly non-ideal solution. The microscopic dynamics in these genre of liquids is still not understood. It is not yet clear, how the dynamics is correlated with the intermediate structure in the liquids. How does the CSRO affect the mass transport in these liquids?. To apprehend the underlying microscopic processes, we have investigated Ni self-diffusion in Al-Ni melts as a function of composition and temperature.

We used incoherent, inelastic neutron scattering (time-of-flight) to investigate the microscopic dynamics in these liquid alloys. Since the Ni atom has a high incoherent neutron scattering cross section, this technique is very suitable for investigating the Ni dynamics in these melts. The time window for the dynamics in metallic liquids is about 0.1 to 100 picoseconds. Quasielastic neutron scattering on cold neutron time of flight spectrometers is the most suitable technique to cover this dynamic window.

There are several experimental techniques to measure the self-diffusion in liquid metals, namely the radio tracer method, secondary ion mass spectroscopy (SIMS), Auger electron spectroscopy (AES), Rutherford back scattering (RBS) and Nuclear-reaction analysis (NRA). The radio tracer method has the disadvantage of convection and SIMS is limited by the natural abundance of the stable isotope in the material. AES is applicable to the diffusion of foreign atoms, since it does not allows for the isotopic analysis. RBS is particularly suitable for detecting heavy elements in the matrix and NRA needs a depth calibration, which is not always based on accurate data of the stopping power in the matrix for those particles emitted by the nuclear reaction. The *in situ* inelastic neutron scattering technique is a versatile technique to investigate dynamics in liquids especially in liquid metals and alloys. Since the measuring time scale is in the picoseconds range, convection does not influence the data, an accurate self-diffusion coefficient can be measured using this techniques.

The main aim of the present work is to study the microscopic structure and the relaxational dynamics in Al and Ni based alloy melts. The aim includes several tasks, sample preparation and characterization, neutron scattering, data analysis and visualization of microscopic dynamics. The outline of the work is as follows:

Chapter 2 gives an introduction to the general properties of liquid metals and alloys. The properties like structure, density, viscosity and thermodynamic properties are presented. This chapter also discusses the basic theoretical understanding of the microscopic liquid dynamics. Chapter 3 enumerates sample preparation and characterization techniques and precautions taken to get clean samples. Chapter 4 describes the instruments and the measurement technique. This chapter also shows theoretically, how to observe the microscopic dynamics by inelastic neutron scattering. Chapter 5 focuses on raw data reduction and visualization of the dynamics from the measured data. Chapter 6 presents results on the microscopic dynamics and the atomic transport mechanisms in dense liquids. The CSRO in Al-Ni melts and its influence on the microscopic dynamics and atomic transport are presented in chapter 7. Chapter 8 gives the conclusions and the scope for the future work.

# Chapter 2

# Liquid metals and alloys

*Summary : This chapter summarizes the general properties of liquid metals and alloys, theoretical studies on self-diffusion and the molecular dynamics simulation methods.*

## 2.1 General properties

### 2.1.1 Structure

How do metallic liquids look like on the microscopic scale? It is clear that all the atoms must be in rapid motion so that the environment of each one must be changing continuously. Considering one single atom and recording the position of its neighbors at successive instants of time the emerging picture of the average environment can be considered as the structure of the liquid. Models like the quasi-crystalline model or the random closed packed model could not explain the structure of metallic liquids satisfactorily.

It was Debye, who in 1915 first demonstrated that in the discussion of X-ray diffraction of liquids, the interference pattern obtained depends crucially on the relative separation of the two atoms or the pair function. The structure and properties of liquids in equilibrium are best described in terms of the pair distribution function $g(r)$. $g(r)$ is defined as the probability of finding another atom at the same instant at a distance $r$ from the reference atom located at $r = 0$. However, it should be kept in mind that $g(r)$ is averaged over time and over all atoms, and does not give a 'snapshot' of an atomic distribution at any particular point of time. The function $4\pi r^2 n_0 g(r)$ is called radial distribution function, where $n_0$ is the number density, and the area under the main peak of this curve can be interpreted as the number of nearest neighbor atoms and the so called the first coordination number. Since the properties of liquids crucially depends on the first coordination number, it is frequently used as an important parameter.

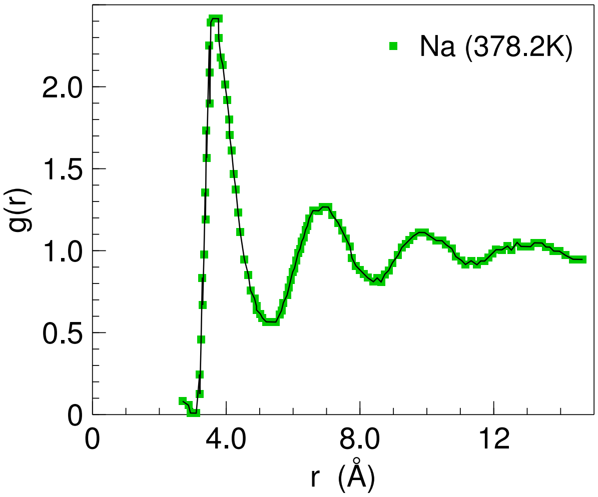

Figure 2.1: The radial distribution function of liquid Sodium at near to the melting point [Wa75].

A typical curve for the pair distribution function $g(r)$ is given in the figure 2.1. There are few maxima and minima in the $g(r)$ and their amplitude decreases rapidly towards unity with increasing $r$. The departure from unity shows the existence of short range order around the reference atoms. Experimentally $g(r)$ can be measured by neutron scattering or x-ray diffraction. The pair distribution function can be obtained from the measured intensity

$$I(q) = Nf^2(q)S(q) \tag{2.1}$$

where $S(q)$ is the structure factor and $f^2$ is the atomic scattering form factor. $g(r)$ is related to the $S(q)$ by

$$g(r) = 1 + \frac{1}{2\pi^2 n_0 r} \int_0^\infty q[S(q) - 1] \sin(qr) dq \tag{2.2}$$

where $q = (4\pi/\lambda)\sin(\theta)$, $\theta$ is the scattering angle, $\lambda$ is the wavelength of the incident beam and $n_0$ is the number density of the liquid. Several thermodynamic quantities can be calculated from the $g(r)$, *e.g.* total internal energy, heat capacity and enthalpy.

In a binary alloy of components 1 and 2, three pair distribution functions, *i.e.* the partial distribution functions $g_{11}(r)$, $g_{22}(r)$ and $g_{12}(r)$ are required for a complete description of its structure. The partial pair distribution functions $g_{\alpha\beta}(r)$ correspond to the probability of finding an atom of type $\beta$ at a distance $r$ from the atom of type $\alpha$ at the origin. The pair distribution function of a binary system is defined by

$$g_{\alpha\beta}(r) = 1 + \frac{1}{2\pi^2 n_0 r} \int_0^\infty q[S_{\alpha\beta}(q) - 1] \sin(qr) dq \tag{2.3}$$

where the $S_{\alpha\beta}$ represent the partial structure factors. One can define a global structure factor of a binary alloy system obtained from scattering experiments, *i.e.* the total structure factor $S(q)$. It can be expressed in terms of its three partial structure factors:

$$S(q) = W_{11}S_{11}(q) + W_{22}S_{22}(q) + 2W_{12}S_{12}(q) \tag{2.4}$$

where $W_{\alpha\beta} = x_\alpha x_\beta f_\alpha f_\beta / \langle x_\alpha f_\alpha + x_\beta f_\beta \rangle^2$. Here $x$ is the atomic fraction and $f_{\alpha,\beta}$ are the atomic scattering form factor. A considerable amount of structural information on liquid metals has been accumulated during the past decades. All of the distribution curves have the same general shape. The structure factor of liquid Sodium is shown in the figure 2.2. In many experimental investigations of the structure of liquid metals it has been found that the hard-sphere like model gives a good description [Fu60, Ar66]. The hard-sphere potential, though a crude approximation, with a suitable choice of hard-sphere diameter and packing fraction (or packing density) reproduces the measured structure factors. The packing fraction is defined as

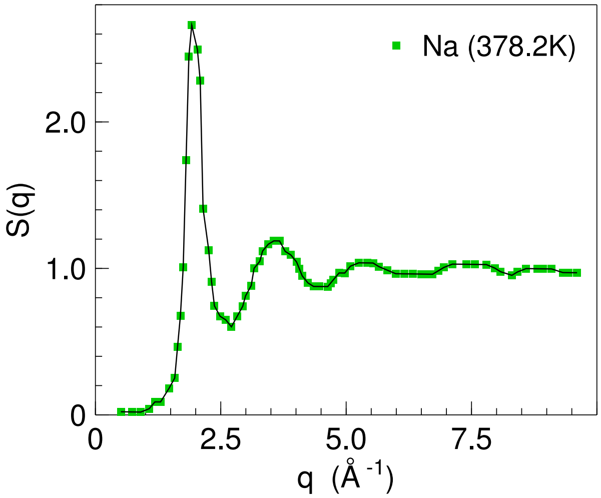

Figure 2.2: The structure factor of liquid Sodium close to the melting point [Wa75].

$$\varphi = \frac{\pi}{6} n_0 \sigma^3 \tag{2.5}$$

where $n_0$ is the number of atoms per unit volume (or number density) and $\sigma$ is the hard-sphere diameter. The results imply that the characteristic features of the structure factor of liquid metals are largely determined by ion-ion repulsions, and that the effect of the long-range oscillation in the pair potential on the structure factor is small for liquid metals and alloys. In practice, even though liquid metals have very complex inter-atomic interactions, the hard-sphere approximation can well describe the structure of liquid metals and alloys.

### 2.1.2 Density

In discussing the nature and behavior of liquid metals and alloys, density is an important quantity. From a practical point of view, density data for liquid metals and alloys provide essential information for topics ranging from mass balance calculations in refining operations or the kinetic of slag/metal reactions to thermal natural convection phenomena in furnaces and ladles. The density data also provide a detailed knowledge of volume changes in metals and alloys at their melting points which is of critical importance in the understanding of the solidification processes. From a more fundamental point of view, the density or specific volume of a liquid enters in to the description of the radial distribution function $g(r)$. Since the determination of $g(r)$ and other basic properties of the liquid metals and alloys require density data, the property of density is of primary importance.

Various methods exist for measuring the density of liquid metals and alloys. These techniques are the Archimedean, the Pycnometric method, the Dilatometric method, the Maximum bubble pressure methods, the Manometric method, the Liquid drop method (Sessile drop method, Levitation method) and the Gamma radiation attenuation method. These methods are reported to be used for the evaluation of the density of liquid Ni, NiP, PdNiP, PdNiCuP and Al-Ni alloy melts.

In the direct Archimedean, a sinker or bob of known weight $w_1$ is suspended by a wire attached to the arm of a balance. When the sinker is immersed into the liquid metals, the new weight $w_2$, or an apparent loss of weight (buoyancy) $\Delta w = w_1 - w_2$ is observed. The density $\rho$ of the liquid metals is then

$$\rho = \frac{\Delta w + s}{g(V + v)} \tag{2.6}$$

where $s = 2\pi r \gamma \cos\theta$, $g$ is the gravitational acceleration, $V$ is the volume of the sinker, $v$ is the volume of the immersed suspension wire of radius $r$, $\gamma$ is the surface tension, $\theta$ is the contact angle between the wire and the liquid and $s$ is the surface tension correction.

In the Dilatometric Method, an accurately weighed specimen is contained in a dilatometer. This is a calibrated vessel fitted with a long, narrow neck. Changes in the volume of the specimen with temperature are continuously monitored via the liquid meniscus height. By calibrating the dilatometer beforehand with the liquid of known density the specimen's density and the thermal expansivity are obtained. The merits of the method are that large amounts of specimen are not required and it provides continuous density measurements. Density data obtained by this method are very accurate, and the direct observation method provides particularly accurate and reliable values. According to Williams and Miller [Wi50] McGonigal and Groose [Mg63] experimental errors in the dilatometric techniques were ± 0.2 %.

In a maximum bubble pressure method an inert gas is passed through a capillary tube immersed to a certain depth in a liquid. A bubble of gas is detached from the tip of the capillary. The density of the liquid specimen can be determined by measuring the over pressure required to just detach a babble of inert gas from the tip of the capillary. The maximum bubble pressure $P_{m1}$ at depth $h_1$ is equal to the sum of the pressure $\rho gh$ needed to maintain the column of the liquid, and the pressure needed to create a bubble's new surface, $2\gamma/r$, where $\gamma$ is the surface tension. If the maximum bubble pressure at a different depth of immersion $h_2$ is $P_{m2}$, then the density of the liquid specimen is given by

$$\rho = \frac{P_{m1} - P_{m2}}{g(h_1 - h_2)} \tag{2.7}$$

Lucas has determined the density values of various liquid metals [Lu70] from their melting points up to 2100 K using this method. He concluded that the accuracy of the techniques was ±0.3 %. A typical maximum bubble pressure experimental setup is given by Veazey and Roe [Ve72]. To obtain reliable density data from these techniques, the depth measurement must be accurate and a correction must be made for any expansion of the capillary tube.

The liquid drop methods involve photographing the profile of a liquid metal drop. After solidification, the metal specimen is then weighed and the volume of the liquid drop is calculated through geometrical analysis of the photograph. Two methods are used for maintaining a stable liquid metal drop: the first employs the sessile drop method, the second uses levitation technique. In the Sessile drop method, a liquid drop rests on a plate or substrate of a smooth horizontal surface. The volume of the drop is calculated from the numerical table of Bashforth and Adam [Ba83]. To prevent asymmetrical shape forming, Vertman and Filippov proposed a so called "large drop method" [Vr64]. According to him the accuracy of the measurement is of the order of 0.5 %. In the levitation technique, the droplet is levitated by electromagnetic induction and the volume is measured by taking a photograph. This method basically eliminates the problem of any chemical reaction between the liquid drops and the substrate or the vessel.

The basic principle of the Gamma radiation attenuation method is based on the attenuation of a gamma ray beam passing through the matter. For a Gamma ray beam of intensity $I_0$ penetrating a specimen of length $x$, the emergent radiation intensity $I$ is given by

$$I = I_0 \exp(-\alpha\rho x) \tag{2.8}$$

where $\alpha$ is the absorption coefficient per unit mass which must be determined first by an absorption measurement on the metal in its solid form. The accuracy of this technique depends on the sensitivity of the radiation counter.

The densities of liquid alloys are generally found to be a linear function of composition [Cr74]. Many liquid alloys show small deviations from this relationship, the maximum deviation usually within ±2 %. But eutectic density minima and a rapid change in density with composition has been reported in a few systems.

Conceptually, the terms atomic volume and molar volume are frequently used in describing the density of liquid metals. The atomic volume of the pure metals, $V$ is defined as the ratio of its atomic weight $M$ to the density $\rho$:

$$V = \frac{M}{\rho} \tag{2.9}$$

For binary systems, the atomic volume $V_A$ is defined by

$$V_A = \frac{x_1 M_1 + x_2 M_2}{\rho_A} \tag{2.10}$$

where $x_1$, $x_2$, $M_1$ and $M_2$ are the atomic fraction and the atomic weight of the components 1 and 2, respectively, and $\rho_A$ is the measured alloy density. In studies of real alloys systems, the excess volume is frequently used. For binary alloys systems, $V^E = V_A - V_{ideal}$, or

$$V^E = \frac{x_1 M_1 + x_2 M_2}{\rho_A} - \left( \frac{x_1 M_1}{\rho_1} + \frac{x_2 M_2}{\rho_2} \right) \tag{2.11}$$

In addition, large difference in atomic volume of two metals forming a liquid alloy can have an important effect on its properties. A negative value of $V^E$ indicates an attractive interaction between dissimilar kinds of atoms. Consequently, excess thermodynamic functions *i.e.* excess entropy and enthalpy of mixing would be expected to show negative values, an example is the Al-Ni system. By contrast, a positive value of $V^E$ indicates repulsive interactions between different kinds of atoms, and entropy and enthalpy are then positive [Ma77]. Alloys systems exhibiting immiscibility are reported to show positive values for free enthalpy of mixing [Ku79].

### 2.1.3 Viscosity

From the microscopic point of view the most characteristic feature of liquids are the high mobility of individual atoms. However, the motion of atoms in liquids are impeded by frictional forces set up by their nearest neighbors. Viscosity is therefore a measure of the friction among atoms. Consequently, liquid metal and alloy viscosities are of great interest in both technology and the liquid metal's properties. From the practical point of view, viscosity plays an important role as a key property to solve quantitatively problems in fluid flow behavior as well as those related to the kinetics of reaction in metallurgical processes. For example, the liquid metal's viscosity is the main factor dominating the penetration of small gas bubbles and non-metallic inclusions.

The definition of the coefficient of shear viscosity or dynamic viscosity is based on the following mathematical expression by Isaac Newton [Bi60]:

$$\tau = \eta \frac{d\nu}{dz} \tag{2.12}$$

where $\tau$ is the shear stress, *i.e.* the force exerted by the fluid per unit area of a plain parallel to the $x$ direction of motion when the velocity $v$ is increasing with distance $z$ measured normal to the plane, at the rate $d\nu/dz$. Thus, the viscosity $\eta$ represents the constant of proportionality. The ratio of viscosity to density (*i.e.* $\nu = \eta/\rho$) is known as the kinematic viscosity $\nu$. The dimension of the kinematic viscosity is equivalent to that of the diffusivity, so that $\nu$ can be considered to represent some thing like the transverse diffusion of momentum down to the velocity gradient.

The viscosities of liquid metals and alloys have been investigated experimentally and theoretically for many decades, and there is an extensive literature available on the subject [Be72, Fa72]. Recently there has been renewed interest in viscosity in connection with glass forming in alloy systems. Glass formation is accompanied by a rapid increasing of viscosity on undercooling [Da76].

The viscosity of pure liquids does show correlation with other quantities. For example, the melting point viscosity of elements varies periodically with atomic number, in the same way as the melting temperature and the surface energy, and oppositely to the molar volume [Ge58, Wi66, Vl74]. Andrade [An52] pointed out that near-equality of the specific heats of solid and liquid at the melting point suggests similar atomic vibrations in both. He derived an expression for the shear viscosity $\eta$ by considering the momentum transfer from one layer of the fluid to another with different velocity. He did not consider the transfer of atoms as in gases, but momentum transfer by contact between atoms in neighboring layers as a result of vibrational displacements from their mean positions. He obtained to the viscosity

$$\eta = \frac{4}{3} v_s \frac{m}{\sigma} \tag{2.13}$$

where $m$ is the mass of atom and $\sigma$ the average inter atomic distance. $v_s$ can be calculated by the Lindemann formula

$$v_s = C_L \sqrt{\frac{T_m}{A \cdot V^{2/3}}} \tag{2.14}$$

where $C_L$ is the constant, $T_m$ is the melting temperature, $A$ is the atomic weight, and $V$ is the molar volume at $T_m$. Combining 2.13 and 2.14, Andrade obtained

$$\eta(T_m) = C_A \sqrt{\frac{T_m}{A \cdot V^{2/3}}} \tag{2.15}$$

where $C_A = C_L \cdot \frac{4}{3} \cdot \frac{m}{\rho}$. The value of $C_A$ is found to be $1.655 \times 10^{-7}$ (J/K mol$^{1/3}$)$^{1/2}$. This formula is found to be applicable in pure metals as well as inter-metallic compounds. In attempting a comprehensive analysis of the viscosity of alloy liquids, the behavior at eutectic compositions is of particular interest because of its association with glass formation [Po78]. The value for $C_A$ falls in to two groups, normal eutectic

$C_A$ has the value of $1.85 \pm 0.4 \times 10^{-7}$ (J/K mol$^{1/3}$)$^{1/2}$, very similar to that for pure metals. For deep eutectic the value of $C_A$ are much higher, $6.52 \pm 1.0 \times 10^{-7}$ (J/K mol$^{1/3}$)$^{1/2}$.

The Stokes-Einstein relation is often used to relate the atomic self-diffusivity $D$ and the viscosity of the liquid metals. Sutherland presented a correction for the Stokes-Einstein relation using a hydrodynamic theory

$$D = \frac{k_B T}{6\pi\eta a} \frac{(1 + 3\eta/\beta_s a)}{(1 + 2\eta/\beta_s a)} \tag{2.16}$$

were $a$ is the radius of diffusing particle and $\beta_s$ is the coefficient of sliding friction between the diffusing particle and media, which is depending on the size of the diffusing particle. When the diffusing particles are large compared to the particle of the medium, $\beta_s$ equal to infinity, when it is equal to the that of the medium, $\beta_s$ becomes 0.

$$D = \frac{k_B T}{6\pi\eta a} \quad \text{when} \quad \beta_s = \infty \tag{2.17}$$

$$D = \frac{k_B T}{4\pi\eta a} \quad \text{when} \quad \beta_s = 0 \tag{2.18}$$

The equation 2.17 and 2.18 are generally known as Stokes-Einstein and Sutherland-Einstein formula, respectively. The Sutherland-Einstein relation using the hard-sphere radius provides good results for the self-diffusivity in liquid metals, even though it does not clarify the atomic process of diffusion in liquids [Mo76].

Gebhardt and Köstlin first related the viscosity of alloys to the phase diagram features [Ge58]. Their conclusions are summarized as follows: In systems showing complete miscibility in the solid and the liquid state, the viscosity approximates to the weighted average viscosity of the two components. A simple eutectic shows a negative deviation from this behavior. Systems with inter-metallic compounds show more complex behavior, with maximum viscosity in the liquid state at a composition corresponding to those of crystalline compounds.

The composition dependence of viscosity in more complex systems is very difficult to describe quantitatively. An attempt was made by Moelwyn-Hughes [Mo64] by calculating the viscosity from the inter-diffusion coefficient using the Stokes-Einstein relation. Assuming a composition independent inter-diffusion coefficient, he obtained the formula

$$\eta = (x_A \eta_A + x_B \eta_B) \left(1 - 2x_A x_B \frac{\Omega}{RT}\right) \tag{2.19}$$

where $\eta_A$ and $\eta_B$ are the viscosities of elements a and b, $x_A$ and $x_B$ are the respective mole fractions and $\Omega$ is the regular solution interaction parameter. The Moelwyn-Hughes formula widely used in the literature [Mo64]. For systems having strongly negative enthalpy of mixing $\Delta H_{mix}$, equation 2.19 gives an increased viscosity for concentrated alloys, which may seem to be in accordance with the observed high viscosities at compound forming compositions. However, equation 2.19 could not predict the lower viscosity expected for eutectic compositions between compounds.

The temperature dependence of viscosity in liquid metals and alloys very often obeys an Arrhenius type relationship.

$$\eta = \eta_0 \exp\left(\frac{E_v}{RT}\right) \tag{2.20}$$

where $E_v$ is the activation energy for viscous flow, $\eta_0$ the pre-exponential factor and $R$ is the gas constant. In glass forming systems the behavior is such that the viscosity increases more with decreasing the temperature than equation (2.20) would predict [Ge58]. This rate of increase of the viscosity increases as the the liquid is undercooled below $T_m$, and is of particular importance in glass forming systems (see fig. 6.9). The transition from liquid to a glass has been analyzed in terms of excess entropy of the liquid [Ad65] and its free volume (*i. e.* the excess of its volume over that of ideal closed packed liquid) [Co59, Tu61, Tu70]. In either case, the predicted temperature dependence of viscosity has the Vogel-Fulcher-Tammann form

$$\eta = \eta_0 \exp\left(\frac{D^* T_0}{T - T_0}\right) \tag{2.21}$$

where $D^*$ is called "fragility parameter" [An95] and $\eta_0$ is the high temperature limit of viscosity calculated from the relation, $\eta_0 = N_A h/V$, where $N_A$ is the Avogadro's number, $h$ is the Plank's constant and $V$ is the molar volume of the liquids and $T_0$ is referred to as the VFT temperature. The equation 2.21 does seem to fit measured data on glass forming systems [Ch68, Po72, Ch78, Ts85a, Ts85b]. The Vogel-Fulcher-Tammann relation applies strictly only to the temperature dependence of equilibrium viscosity [Ts85a].

## 2.2 Theoretical aspects of diffusion

Diffusion is the transport of mass from one region to another on an atomic scale. Diffusivities in the liquid state are much higher than that in the solid state. In the case of normal metals and alloys, diffusivities in the two states differ by a factor of 100 to 1000 [Kr87]. One of the most characteristic properties of liquid metals is that the diffusivity of atoms just above the melting points is the order of $10^{-9}\mathrm{m}^2\mathrm{s}^{-1}$.

A knowledge of diffusivities is needed for many fields of engineering. For example, for most metallurgical processes, heterogeneous chemical reactions play an important role. The rate of heterogeneous reactions are limited by the diffusion of the reactant species. Similarly, the distribution of solute elements during solidification also depends upon their diffusive motion. For clear understanding of those phenomena related to diffusion, a study of self diffusion in liquid metals is of critical importance.

Remarkable progress has been made over the last fifteen to twenty years in the development of diffusion theories for liquid metals. The hard-sphere theory in particular seems to be able to provide an accurate means for calculating the self-diffusivities in fairly simple one component liquid metals [Pr73]. However it may be premature to conclude its total success. Corresponding-state methods are another theoretical way to calculate transport coefficient in the liquid metals [Ch66, Pa67, Ri80]. In the dense glass forming liquid alloy metals, the microscopic dynamics found to be well described by mode coupling theory [Go92]. Molecular dynamics simulations is another way to understand the microscopic dynamics of liquids, particularly in liquid metals and alloys. The following sections briefly outlines theories and simulations developed in the past in context with microscopic dynamics in liquid metals and alloys.

### 2.2.1 Chemical or mutual diffusion

The diffusion process in a binary liquid is described by a phenomenological law and it states that, if there is a chemical concentration gradient in a finite volume, the impurity material will tend to move such that the concentration gradient is decreased. If the flow is sustained for a sufficient amount of time, the substance will become homogeneous and diffusion will cease. Fick's first law is an equation describing the flow of an impurity in a substance, showing that the flux of material across a given plane is proportional to the concentration gradient across that plane.

$$J = -\tilde{D}\frac{\partial c}{\partial x} \tag{2.22}$$

where $c$ is the local concentration, $x$ is the distance in the direction in which diffusion occurs, and $\tilde{D}$ is the inter-diffusivity or mutual diffusion coefficient The diffusing particle in a binary system, always flow in the direction of decreasing concentration gradient, and the negative sign is therefore introduced in order to make the diffusivity $D$ positive. On combining 2.22 and the equation of continuity ($\partial c/\partial t = -\partial J/\partial x$), we have

$$\frac{\partial c}{\partial t} = \tilde{D}\frac{\partial^2 c}{\partial x^2} \tag{2.23}$$

is the equation independent of concentration current. This equation is known as Fick's second law [Bo69].

### 2.2.2 Self-diffusion or random walk

The self-correlation function $G_s(\Delta r, \tau)$ is the probability that a particle starting at some position $r_0$ at the initial time $t_0$ is found to be at $R = \Delta r + r_0$ after $\tau = t - t_0$. The transport equation for $g_s$ can be written in the analogous to Fick's second law

$$\frac{\partial G_s(r,t)}{\partial t} + D\Delta^2 G_s(r,t) = 0 \tag{2.24}$$

where $D$ is the self-diffusion coefficient. The equation is microscopic, being equivalent to the Fokker-Plank equation in the mathematical theory of probability. It can be derived by assuming that the motion of a single particle is described as a random walk process, where only two successive values of displacements are correlated to each other in the particle's many-step meandering course. Solving the equation 2.24 subjected to the initial condition that $G_s(r,t) = \delta(r)$, and assuming that the liquid is isotropic, one find

$$G_s(\Delta r, t_0) = \delta(\Delta r, t_0), \int\limits_V G_s(\Delta r, t) d^3 r = 1 \tag{2.25}$$

The finial expression for $g_s(\Delta r, \tau)$

$$G_s(\Delta r, \tau) = (4\pi D\tau)^{-3/2} \exp[-(\Delta r)^2/4D\tau] \tag{2.26}$$

Therefore the mean square displacement of the particle over time $\tau$ is

$$\int\limits_V (\Delta r)^2 G_s(\Delta r, \tau) d^3 \Delta r = 6D\tau \tag{2.27}$$

and the self-diffusion coefficient can be written as

$$D = \lim_{\tau\to\infty} \frac{1}{6} \frac{\langle(\Delta r(\tau))^2\rangle}{\tau} \tag{2.28}$$

where the time $\tau$ is chosen to be so long that the ratio $\langle(\Delta r(\tau))^2\rangle/\tau$ may be constant. This formula is an important equation given by Einstein.

### 2.2.3 Diffusion based on hard sphere models

The simplest approach to the calculation of transport coefficient in liquid metals and alloys is to assume a hard-sphere potential for the inter-atomic interaction which permits one to describe the transport process by modifying the kinetic theory of gases. An equation based on the kinetic theory of gases, the self-diffusion in hard-sphere liquids at high densities was first proposed by Enskog [Ch39]. Enskog's expression for $D$ is of the form

$$D = \frac{8}{3}\frac{v}{\sigma^2}\left(\frac{k_B T}{\pi M}\right)^{1/2}\frac{1}{g_0^2(\sigma)} \tag{2.29}$$

where $v = 1/n$ is the volume per sphere $(V/N)$, $\sigma$ is the diameter of the hard sphere with mass $M$, $g_0^2(\sigma)$ is the equilibrium pair correlation function and it is equal to one for dilute fluids. It has been noted that expression 2.29 for transport coefficient is insufficient to explain the properties of dense hard sphere fluids without the use of correction factors. This is so, because successive collisions and many body interaction in the process of interest have been neglected.

Taking account of the above facts Protopapas, Anderson and Parlee [Pr73] derived a formula for the self-diffusion in liquid metals

$$D = C_{AW}(\varphi)\left(\frac{\pi k_B T}{M}\right)^{1/2}\left(\frac{6}{\pi n_0 \varphi^2}\right)^{1/3}\frac{(1-\varphi)^3}{\varphi(1-\varphi/2)} \tag{2.30}$$

where $\varphi = \frac{\pi}{6} n_0 \sigma^3$ is the packing fraction. According to this model the temperature depended of $D$ comes from the change in $n$ and $\sigma$ in addition to the factor $T^{1/2}$. In many liquid metals values of $\sigma$ fitted to experimental data of $D$ can be summarized empirically by

$$\sigma(T) = 1.126\,\sigma_m[1 - 0.112(T/T_m)^{1/2}] \tag{2.31}$$

$$\sigma_m = 1.41(M/\pi\rho_m N_A)^{1/3} \tag{2.32}$$

in which $\sigma_m$ is the value of $\sigma$ at the melting point $T_m$, where $\varphi$ is taken as 0.472. The equation 2.30 gives good results for the magnitude and temperature dependence of the self-diffusivity for normal and one component liquid metals. A comparison of experimental self-diffusion coefficients at the melting point and the predictions of the present theory is presented in table 2.1. The computed results are in good agreement with experimental data currently available. However, since the experimental errors in diffusivities are of the order of ±40 per cent, it is not fruitful to make a detailed comparison of predicted and observed self-diffusivities.

| *Element* | *Experiment* ($D \times 10^{-9} m^2 s^{-1}$) | *Theory* ($D \times 10^{-9} m^2 s^{-1}$) |
|---|---|---|
| Li | 7.00 ([Na67]) | 7.01 |
| Na | 4.22 ([Na67]) | 4.24 |
| K | 3.82 ([Na67]) | 3.85 |
| Cu | 3.96 ([Na67]) | 3.40 |
| Ni | 3.90 ([Sm04]) | 3.30 |

Table 2.1: Self-diffusion coefficient $D$ from the equation 2.30 and experiments. The results show that the values of $D$ agree well with the experimental ones for simple liquid metals.

### 2.2.4 Corresponding state principle

In the statistical mechanics of fluids [Ch66], the principle of corresponding states can be applied to the case were the pair potential takes the form

$$u(R) = \varepsilon\psi(R/\sigma) \tag{2.33}$$

were $\varepsilon$ and $R$ are scale parameters of the dimension of energy and length. $\psi$ is the universal function that depends only on R/$\sigma$. The reduced variables are-given by

$$T^* = k_B T/\varepsilon, \tag{2.34}$$

$$V^* = V/N\sigma^3, \tag{2.35}$$

$$p^* = p\sigma^3/\varepsilon. \tag{2.36}$$

Helfand and Rice[He60] extended the theory to the transport properties by calculating the time integral of appropriate time-correlation function. Their expression for the self-diffusivity is

$$D^* = DM^{1/2}\varepsilon^{-1/2}\sigma^{-1}. \tag{2.37}$$

These equations were applied by Pasternak [Pa72] to analyze the transport coefficient of liquid metals. From 2.37 and 2.36 it follows that

$$\frac{\eta^* V^*}{D^*} = \frac{\nu}{D}. \tag{2.38}$$

where $\rho$ is the mass density and $\nu$ the kinematic viscosity. He showed that a plot of experimental $\nu/D$ of liquid metals versus 1/T can be superimposed by choosing a suitable value of $\varepsilon$ for each element and plotting $\nu/D$ versus 1/T; then $\varepsilon$ was found proportional to the melting temperature in the form $\varepsilon = 5.2K_B T_m$. A semi-log plot of $D^*(V)^{2/3}$ against $1/T^*$ found to be linear in most of the liquid metals by Waseda and Ohtani [Wa77].

### 2.2.5 Free volume theory

Cohen and Turnbull [Co59] developed a free volume theory of self-diffusion, in which an atom was assumed to be enclosed by a cage formed by its neighboring atoms. The atoms can undergo translational displacement only when statistical distribution of free volume yields a void of critical volume $v^*$ sufficient to accept the atom. Thus, $D$ is given by,

$$D = G_D \sigma (3k_BT/M)^{1/2} exp[-\gamma v^*/v_f] \tag{2.39}$$

where $G_D$ is a geometrical factor, usually taken as 1/6, $\sigma$ is the atomic diameter and $\gamma$ is the correction factor between 0 and 1 due to the overlap of free volume $v_f$, which is approximated by $v_f = \alpha v(T - T_0)$. Here $\alpha$ is the coefficient of thermal expansion, $T_0$ is the temperature where the $v_f$ vanishes. This equation is found to fit reasonably with the experimental $D$ of liquid metals. Moreover Turnbull and Cohen [Tu70] made refinement of their theory in which the correlation effect like gas and solid like diffusion processes are included using continuous distribution functions.

### 2.2.6 Diffusion in liquid alloys

Theories of transport coefficient of pure metals, mentioned in the earlier sections can be extended straightforwardly to those of liquid alloys by making suitable modifications. Starting with Einstein's theory, $D = k_BT/\zeta$, where $\zeta$ is the friction coefficient, one can apply this formula in Enskog's equation (2.29). Then the hard core part of the friction coefficient of component '$i$' in liquid alloys can be written as

$$\zeta_{hi} = \frac{8}{3}\sum_j n_j g^{(2)}_{0ij}(\sigma_{ij})\sigma^2_{ij}\left(2\pi M_{ij}k_BT)\right)^{1/2} \tag{2.40}$$

Here $n_j$ is the number density of atom $j$ with mass $M_j$, $g^{(2)}_{0ij}(\sigma_{ij})$ is the equilibrium pair correlation function for the species $i$ and $j$ at the closest distance of approach, $\sigma_{ij}$ is the distance between the hard sphere of $i$ and that of $j$ and $M_{ij}$ is the reduced mass. The soft part of the friction coefficient is given by [Si66, Ro69].

$$\zeta_{si} = \sum_j n_j \zeta_{ij} \tag{2.41}$$

$$\zeta_{ij} = \frac{M_{ij}}{3}\left(\frac{1}{\zeta_{si}} + \frac{1}{\zeta_{sj}}\right)\int_{R>\sigma_{ij}} \nabla^2 u_{ij}(r) g^{(2)}_{0ij}(R) d^3R \tag{2.42}$$

The resulting self-diffusion coefficient is the form

$$D_i = \frac{k_BT}{\zeta_{hi} + \zeta_{si}} \tag{2.43}$$

In which the cross effect term is ignored, for hard-sphere liquids one can omit $\zeta_{si}$ and a correction factor is added due to many body effect then,

$$D_i = \frac{C_{hi} k_B T}{\zeta_{hi}} \tag{2.44}$$

The value of $C_{hi}$ can be compared to molecular dynamics results of binary hard-sphere mixtures obtained by Alder *et. al.* [Al74]. Enksog's type of expression for transport coefficient of mixed hard-sphere fluids was given by Throne [Ch39]. Most of the diffusion measurement performed for the liquid alloys are concerned with inter-diffusion coefficients, which are associated with the gradient of chemical potential. A detailed comparison with this theory and experimental data are not known.

## 2.3 Mode-coupling theory (MCT)

MCT describes the transition of super-cooled liquids to a non-ergodic state [Be84]. The transition of the super-cooled liquid to the glass state represents a critical slowing down of the particle motion, leading to a structural arrest. A characteristic property of the arrested state is that it has the static structure factor $S(q)$ of the liquid. Apart from the parameters describing the microscopic motion, the static structure factor is the only input to MCT, which aims to give a complete description of the dynamical properties of the system.

The mode coupling theory is developed in the framework of molecular hydrodynamics. In simple liquids, classical hydrodynamics describes the density fluctuations $\delta\rho(r,t)$ by an equation of motion for the normalized density correlation function of $\Phi(q,t)$:

$$\Phi(q,t) = \frac{\langle \rho_q^*(t)\rho_q(0)\rangle}{\langle |\rho_q|^2\rangle} \tag{2.45}$$

as

$$\ddot{\Phi}_q(t) + \gamma_q \dot{\Phi}_q(t) + \omega_q^2 \Phi_q(t) = 0 \tag{2.46}$$

where $\omega_q = c\,q$, $c$ is the adiabatic speed of sound and $\gamma_q \propto q^2$ is the sound attenuation coefficient. Temperature (entropy) fluctuations which are coupled to the density via thermal expansion are ignored here for the sake of simplicity. For liquids possessing the relaxational dynamics, equation (2.46) can be generalized by replacing the frequency dependent part $\gamma_q$ with a more elaborate function (memory function) and replacing $\omega_q$ by a general frequency $\Omega_q$. Then the equation 2.46 becomes

$$\ddot{\Phi}_q(t) + \Omega_q^2 \Phi_q(t) + \int_0^t M_q(t-t')\dot{\Phi}_q(t')dt' = 0 \tag{2.47}$$

$\Omega_q$ can be considered as "phonon frequency" at the wave number $q$. The memory function $M_q(t)$ is a correlation function of force fluctuations, which is in turn functional of density correlations. The equation 2.47 has frequently been used the starting point of the analysis of experimental data, with memory function $M_q(t)$ modeled by various parametrized empirical functions. While such a generalized hydrodynamic approach often fit experimental data, they could not produced any insight into physical processes responsible for the form and the strong temperature dependence of the dynamics. What is missing in these approaches is a theory of $M_q(t)$.

MCT began with equation 2.47, where the memory kernel $M_q(t)$, the correlation function of fluctuating forces $F(q,t)$ is separated into a fast regular component $\gamma_q\delta(t)$ and time dependent part $\Omega_q^2 m_q(t)$. The fluctuating force occurs primarily between pairs of particles, the dominant contribution to $F_q(t)$, the Fourier transform of $F(r_{12})\delta\rho(r_1,t)\delta\rho(r_2,t)$ can be approximated as a sum of density fluctuation pairs $\rho(r_1,t)\rho(r_2,t)$ with $q_1+q_2=q$. Since MCT does not aim to describe the detailed microscopic short-time dynamics, but rather give a universal picture of relaxational dynamics at longer times, the integral kernel is split into

$$M_q(t) = \gamma_q\delta(t) + \Omega_q^2 m_q(t) \tag{2.48}$$

where $\gamma_q$ models the damping by fast modes and $m_q(t)$ accounts for memory effects through the coupling to slow modes. The basic idea of the mode coupling theory of the liquid-to-glass transition is to consider all the slow products of density fluctuation. By derivation, $m_q(t)$ contains no terms linear in $\Phi_q(t)$. Therefore, in lowest order, it is a quadratic functional

$$m_q(t) = \sum_{q1+q2=q} V_q(q1,q2)\Phi_{q1}(t)\Phi_{q2}(t) \tag{2.49}$$

in a further approximation, the coupling coefficient $V_q$ are specified in terms of the static structure of the liquids, *i.e.* the coupling constant $V(q_1,q_2)$ in 2.49 contains only the static structure factor and not the inter-atomic potential. This is a crucial simplification since for some potentials, (*e.g.* hard spheres) potential are singular, but the structure factor is always well behaved.

The $t\to\infty$ limit of $\Phi(q,t)$ is called the non-ergodicity parameter $f_q(T)$. At high temperatures, where the coupling constants $V(q1;q2)$ in equation (2.49) are small, $\Phi(q,t)$ decays to zero rapidly following the initial microscopic transient. The system is ergodic, and $f_q(T)=0$. With decreasing $T$, the coupling constants increase smoothly, until the glass transition singularity is reached where $\Phi(q,t)$ no longer decays to zero, even for infinite time. The density fluctuations are then partially frozen in, since $\Phi(q,t)$ only decays from 1 to $f_q(T)$ with $0 < f_q(T) \le 1$. The system is then non-ergodic with the frozen-in density fluctuations producing elastic scattering. The non-ergodicity parameter $f_q(T)$ is equivalent to the Debye-Waller factor.

A smooth variation of the coupling constants with decreasing $T$ (or increasing packing fraction) leads to a critical temperature $T_c$ at which $f_q(T)$ changes discontinuously from zero to a non-zero critical value $f_c^q$ . Solving the MCT equations for $t \rightarrow 0$ and $T \rightarrow T_c$, one finds that, for $T < T_c$,

$$f_q(T) = f_q^c + h_q^{'} \sqrt{\sigma} \tag{2.50}$$

where $\sigma \propto (T_c - T)/T_c$ is called the separation parameter. This square-root cusp in $f_q(T)$ is the first general prediction of MCT. Since, at $T = T_c$, $\Phi_q(t \rightarrow \infty)$ jumps discontinuously from 0 to $f_c^q$ , the dynamical singularity at $T_c$ constitutes a bifurcation. Because there are many control parameters in the theory (all of the $V_q$ ), many types of bifurcations are technically possible. The type thought to be most relevant to the liquid glass transition, the fold bifurcation, is what occurs in the solution of a polynomial equation when two solutions coalesce [Ar92].

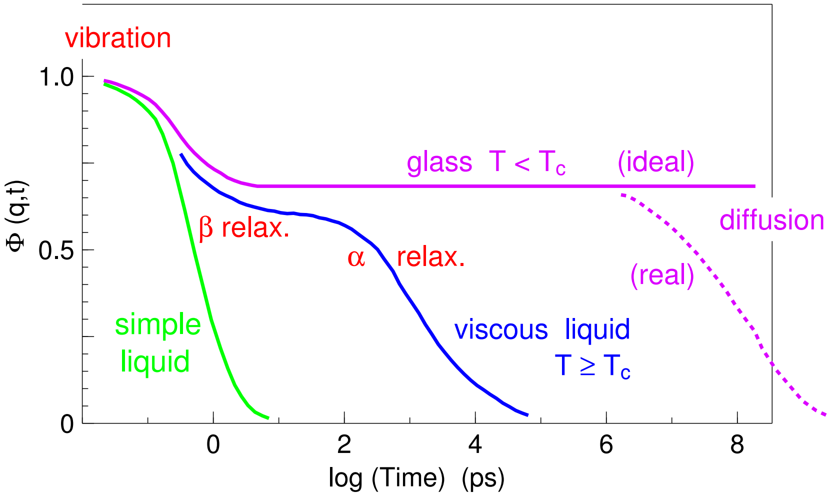

Figure 2.3: Relaxation in liquids, a schematic plot of $\Phi(q,t)$ versus $\log(t)$. $\Phi(q,t)$ shows two step relaxation in viscous liquids, a fast $\beta$ relaxation and a slow $\alpha$ relaxation.

At high temperatures, solutions of the MCT equations have the form illustrated in figure 2.3 for simple liquids (green curve). The short-time microscopic transient decays to zero (with damped oscillation) within a time window of about one decade. As $T$ decreases, the microscopic transient is followed by decay towards a plateau, which is followed by a second decay ending in the familiar $\alpha$ relaxation process. As $T$ decreases further, the plateau extends to longer times as illustrated in figure 2.3 for viscous liquids. This splitting off of the structural relaxation from the initial microscopic transient produces the two-step relaxation scenario in the region between the microscopic dynamics and the $\alpha$ decay which has been observed in many experiments and computer simulations. In MCT, this region is designated the $\beta$ relaxation region.

The development of the intermediate two-step decay as $T$ decreases reflects the growing strength of the cage effect, *i.e.* temporary localization of a particle in the transient cage formed by its neighbors. One can roughly view the sequence of dynamical regimes of the relaxation process as an initial microscopic motion of each particle within its transient cage followed, beyond the plateau region, by collective motion of the cage. The beginning of the decay away from the plateau, called the von Schweidler decay, corresponds to the initial break-up of the cages which is followed, finally, by the long-time $\alpha$ relaxation.

The plateau level for $T \geq T_c$ is $f_c^q$ , the value of $\Phi_q(\infty)$ at $T = T_c$. As $T$ approaches $T_c$, $\Phi(q,t)$ remains close to $f_c^q$ for increasingly longer times. Close to the bifurcation, where $(T - T_c)/T_c \ll 1$, the MCT equations can be expanded in the small parameter $\Phi(q,t) - f_c^q$. Several central MCT predictions can then be derived analytically from this asymptotic analysis. First, one finds that

$$\Phi(q,t) - f_q^c = h_q G(t) \tag{2.51}$$

$G(t)$ is the solution to the equation. Note that $\Phi(q,t)$ given by equations 2.51 matches the full solution of the MCT equations only in the asymptotic region close to $\Phi(q,t) = f_c^q$. This asymptotic beta-correlator solution lacks both the short-time microscopic structure and the long-time $\alpha$ relaxation structure which are, however, present in the full MCT solutions.

The scaling region of the MCT equations can be found analytically from the asymptotic solutions. Also it can be illustrated that the scaling region increases rapidly with increasing $n_0$, *i.e.* as the packing fraction approaches $\varphi_c$, or $T$ approaches $T_c$. The experiments of this work are only concerned with the $\alpha$ relaxation regime, so the $\beta$ scaling law is not further discussed here.

The $\alpha$ scaling law of MCT predicts the time-temperature superposition principle which asserts that relaxation spectra at different temperatures can be superimposed by scaling the time as $t/\tau(T)$ where $\tau(T)$ is the $\alpha$ relaxation time. The long-time asymptotic analysis of the MCT equations for $\sigma < 0$ and $(T - T_c)/T_c \ll 1$ leads to the scaling relation

$$\Phi(q,t) = F_q^\alpha(t/\tau) \qquad (t \gg t_q) \tag{2.52}$$

The master function $F_q$ is independent of $T$. It is determined by the vertices in equation (2.49) evaluated for $T \cong T_c$. Numerical solutions of the MCT equations show that the relaxation can be described, to a good approximation, by the Kohlrausch-

Williams-Watts (KWW) stretched exponential function.

$$\Phi(q,t) = f_q^c \exp[-(t/\tau_q)^{\beta_q}] \tag{2.53}$$

both $\tau_q$ and $\beta_q$ are found to be $q$ dependent in solutions of the MCT equations, a result that is confirmed by computer simulations and neutron scattering experiments. Since the von Schweidler exponent $b$ is independent of q, there cannot be any simple relation, in general, between $b$ and $\beta$ . An exception occurs for $q \to \infty$ where Fuchs [Fu94] has shown that equation 2.53 is exact, with $\beta(q \to \infty) = b$. The range of validity of the asymptotic $\alpha$ relaxation results is much larger than that of the $\beta$ relaxation results, accounting for the general validity of time-temperature superposition for $\alpha$ relaxation. For temperatures far above $T_c$, $\beta$ may either increase or decrease with increasing $T$ without violating the asymptotic MCT predictions.

We consider the temperature dependence predicted by MCT for the $\alpha$ relaxation time, $\tau$. In the von Schweidler regime, one has

$$\Phi(q,t) - f_q^c \propto \sqrt{|\sigma|}\left(\frac{t}{\langle t_q\rangle}\right)^b \tag{2.54}$$

But

$$\sqrt{|\sigma|}\left(\frac{t}{t_q}\right)^b = \left(\frac{t}{t_0}\sigma^{1/2a}|\sigma|^{1/2b}\right)^b \tag{2.55}$$

so the von Schweidler decay region must move to longer times as $T$ decreases following

$$t'_\sigma = \frac{B^{-1/b}t_0}{|\sigma|^\gamma} \tag{2.56}$$

with

$$\gamma = \frac{1}{2a} + \frac{1}{2b} \tag{2.57}$$

(B is a number of order unity) Since the $\alpha$ relaxation must smoothly continue the von Schweidler decay, MCT predicts that the $\alpha$ relaxation time has the same temperature dependence as $t'_\sigma$

$$\tau(t) \propto (T - T_c)^\gamma \qquad (T > T_c) \tag{2.58}$$

Plots of $(1/\tau)^\gamma$ versus $T$ exhibit linear behavior as predicted by equation 2.58 over considerable temperature ranges. Extrapolating to zero at $T_C$ that is generally compatible with the $T_c$ deduced from the $\beta$ relaxation analysis. However, on approaching $T_c$, plots of experimental $(1/\tau)^\gamma$ data generally deviate from the linear extrapolation, exhibiting upward curvature. This observation indicates that, in structural glasses, the complete structural arrest at $T_c$ predicted by the idealized MCT does not occur due to atomic hopping [Go92].

## 2.4 Molecular dynamics simulation

It has been shown that the inelastic neutron scattering experiments on liquid alloys and metals are very important in the understanding of the microscopic atomic motion. However, the present knowledge of such experiments is still limited because of experimental difficulties. For example, the atomic motion is given in terms of the dynamic structure factor. Measurement of this function is made by analyzing the scattering intensity of neutrons from a target sample as a function of momentum $\hbar q$ and energy $\hbar\omega$. We will see in the section 4.3 that the information on the coherent and incoherent contributions in neutron inelastic scattering can be obtained separately by making use of difference in the average value of the scattering length of the nuclei with different isotopes. In most cases either the neutral atoms have very low neutron incoherent scattering cross sections or the isotopes are not stable. Also many alloys melt at very high temperatures. These high temperature are presently not feasible experimentally. Therefore, it is not possible to investigate these liquid metals by neutron scattering methods.

Molecular dynamic simulations (MDS) is a powerful method to determine the quantities which are difficult to access in real experiments or hard to obtain in reasonable precision. The idea is to calculate the forces acting on the atoms in a molecular system and to analyze their motion. When enough information on the motion of the individual atoms have been gathered, it is possible to condense it using the methods of statistical mechanics. These properties include the structure (e.g. correlation functions, predicted x-ray and neutron diffraction patterns), thermodynamics (e.g. enthalpy, temperature, pressure) and the transport properties (e.g. thermal conductivity, viscosity and diffusion). In addition, molecular dynamics can be used to investigate the detailed atomistic mechanisms underlying these properties and to compare them with the theory. It is a valuable bridge between experiment and theory.

To investigate structural and transport phenomena in the liquid state by MD simulation techniques, the system is to be considered as collection of $N$ particle with mass $M$ and potential $u(R_{ij})$ enclosed in a box. The position of the $i^{th}$ particle $R_i(t)$ and its velocity $v_i(t)$ at a time $t$ are described in terms of Newton's equations of motions. A set of variables $(R_1, v_1, R_2, v_2, ...R_N, v_N)$ of all the particles at time $\tau = t - t_0$, $t_0$ is the initial time, can in principle, be determined by solving simultaneously such equations for the motions of $N$ particles.

There are two approaches for molecular dynamics to the calculation of $D$. The first is based on the mean square displacement $\langle|\Delta R|^2\rangle$, which is written in the computer experiment

$$D = \lim_{\tau\to\infty} \frac{1}{6\tau} \langle \Delta(\tau)^2 \rangle \tag{2.59}$$

where the time means the asymptotic time behavior.

The second is performed by integrating the velocity autocorrelation function $\Psi_v(t)$ with respect to $t$,

$$D = (k_B T/M) \int_0^\infty \psi_v(t) dt \tag{2.60}$$

were $\psi_v(t)$ is:

$$\psi_v(t) = \frac{\langle \vec{v}(t).\vec{v}(0) \rangle}{\langle v(0)^2 \rangle} \tag{2.61}$$

The MD method has been extensively developed by Rahman [Ra64] and Verlet [Ve67] for simple liquids with Lennard-Jones type potentials. Numerous MD simulation articles can be found describing liquid metal properties particularly the microscopic dynamics [Ju87].

# Chapter 3

# Sample preparation and characterization

*Summary : This chapter presents the details of the preparation of the samples for neutron scattering, methods used to characterize the prepared alloys and the results of characterization.*

## 3.1 Sample materials

All the samples were prepared from highly pure elements. The pure elements were procured from Chempour chemicals. The purities of these elements are Aluminum 99.98%, Copper 99.99%, Nickel 99.99% , Phosphorus 99.999% and Palladium 99.99%, respectively. Arc and induction melting are employed to prepare the alloys. The prepared alloys are $Al_{90}Ni_{10}$, $Al_{80}Ni_{20}$, $Al_{77}Ni_{23}$, $Al_{70}Ni_{30}$, $Ni_3Al$, $Ni_{80}P_{20}$, $Pd_{40}Ni_{40}P_{20}$ and $Pd_{43}Ni_{10}Cu_{27}P_{20}$. The Al-Ni-Ce alloy samples were obtained from HMI, Berlin.

## 3.2 Arc melting

The arc melting apparatus consists of a chamber, which can be evacuated to a high vacuum. The base, where the elements are placed for melting is made of Copper with water circulation, acts as the cathode. A tungsten rod, which is hanging from the top of the chamber can be moved horizontally and vertically acts as the anode. The arc is discharged between these electrodes. The alloys were prepared in an inert gas atmosphere at a pressure nearly equal to one atmosphere. Before melting the elements, the chamber was evacuated and filled with highly pure Argon gas. This process was repeated several times to get an oxygen-free atmosphere in order to avoid any possible oxidation of the samples during melting at high temperatures.

The temperature in the arc can be varied up to 3000 K by increasing the current. In order to have highly homogeneous alloys, the samples were melted several times by turning upside down. The samples are then weighed to check there is any possible evaporation of materials. This serves as a first check for the correct composition.

Arc melting is mainly used for preparing alloys from elements having high melting temperatures. The Al-Ni alloys were mainly prepared by the arc melting technique. Even though Aluminum is a highly oxidizing element, with a high inert atmosphere and high temperature we could prepare highly homogeneous Al-Ni alloys. It is important to have highly homogeneous alloys because the neutron scattering signal is significantly affected by the element distribution in the melts. High Al content $Al_{90}Ni_{90}$ alloys were found to be in-homogeneously alloyed. Because of this reason, this alloy was prepared by induction melting techniques. In the case of Phosphorus bearing samples, at first we prepared a Phosphorus free pre-alloy which is then melted with Phosphorus by the induction technique.

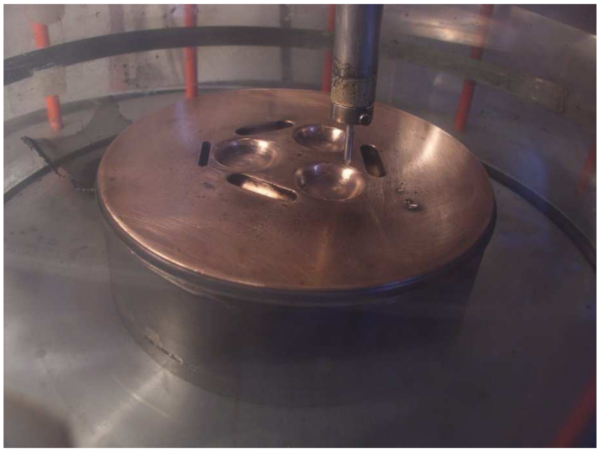

Figure 3.1: This picture shows the inside of an arc melting chamber. A needle pointing down is the W anode used to generate the arc and beneath is the Cu cathode with provisions to keep the elements. Different geometries of these slots are used to make samples with different shapes.

## 3.3 Induction melting

The vacuum induction melting technique was originally developed for the processing of specialized and toxic alloys. Electromagnetic induction is used as the energy source for melting the metals. Induction melting works by inducing eddy currents in the metals. The induction coil is the energy source which carries an alternating current. The eddy current heats and eventually melts the samples.

To prepare PdNiP and PdNiCuP, we used arc melting followed by induction melting. The boiling temperature of Phosphorus is about 533 K and the melting temperature of Ni is 1726 K. The large difference in the melting and boiling temperatures results in evaporation of Phosphorus when it is melted with Nickel. To avoid this problem we first made a pre-alloy (PdNi, PdNiCu) with arc melting. The melting temperatures of these pre-alloys are considerably lower than that of pure Nickel.

The pre-alloy is then induction melted with Phosphorus. The induction melting was done in a quartz tube. The quartz tube can withstand temperatures up to 1400 K. The elements were placed in the quartz tube in such a way that Phosphorus was at the bottom, followed by PdNiCu and $B_2O_3$. $B_2O_3$ serves two purposes: (1) as a flux to clean oxide impurities and (2) to prevent Phosphorus getting out of the melting zone. During induction melting the samples are first melted at high temperatures and then kept for five to seven minutes just above the melting temperature to get a completely homogeneous alloy. The melt is then quenched in cold water. The alloy is then taken out from the quartz tube and weighed and then characterized.

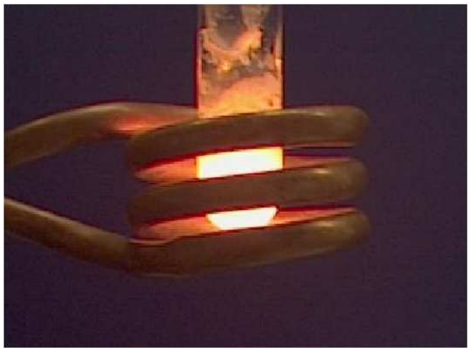

Figure 3.2: This figure shows induction melting of $Pd_{43}Ni_{10}Cu_{27}P_{20}$ sample. The induction coil (made of copper) and melting of the sample inside the quartz tube are also seen. The white patches inside the quartz is $B_2O_3$.

## 3.4 Melt spinning

In the case of $Ni_{80}P_{20}$, the material does not form a glass under the cooling rates of $\sim 10$ K s$^{-1}$ in induction melting and followed by water quenching. Cooling rates as high as $10^6$ K s$^{-1}$ are needed to make a glass [Ni85]. To achieve this cooling rate, we used the melt-spin technique. In this technique, the sample is melted with induction in a quartz tube. The quartz tube has a small opening at the bottom. The melt is then forced by Argon and discharged on to a fast rotating Copper disc. All are kept in an evacuated chamber or filled with Helium at low pressure. With this technique, the melt can be quenched at a high cooling rate. The melt comes out as ribbons (see figure 3.3) and the thickness of the ribbons can be varied with proper choice of the angular velocity of the disc and the diameter of the melt discharge. The melt spin process is shown in the figure 3.3.

## 3.5 Differential scanning calorimetry

The differential scanning calorimetry (DSC) is a technique for measuring the energy necessary to establish a nearly zero temperature difference between a substance and an inert reference material. As the two specimens are subjected to identical temperature regimes in an environment heated or cooled at a controlled rate. We used

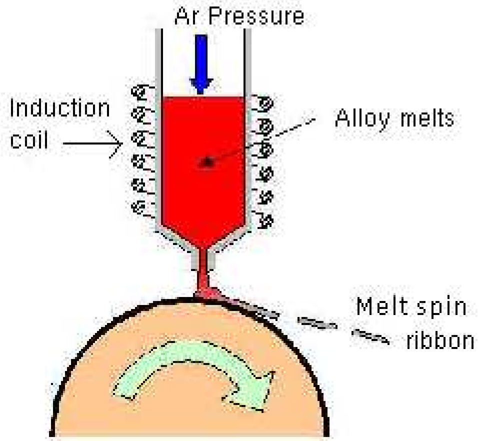

Figure 3.3: The melt spin process: The alloy is induction melted in a quartz tube and injected on a Cu disc using highly purified Argon. The disc and quartz tube are kept inside in a He filled chamber. The melts come out from the disc in the forms of ribbons.

the Rheometric Scientific Thermal analyzer 902-30010 to perform the experiment. This is a dual purpose equipment, it can be used to perform thermogravimetric analysis (TGA) and differential scanning calorimetry (DSC). TGA quantifies the mass with respect to temperature and DSC examines the heat flow as a function of temperature.

The instrument was calibrated before the measurements. Calibration of DSC consists of two parts: the balance calibration (TGA) and calorimetric (DSC). The balance calibration adjusts the analog-to-digital converter in the balance mechanism. The calorimetric calibration generates a calibration of heat flow to a known standard as a set of coefficients to correct for the thermocouple non-linearly. The calorimetric calibration again has two parts, (1) the sensitivity calibration, *i.e.* it calculates the proportionality factor relating the thermocouple voltage to the heat flow and (2) the furnace calibration used to reconcile the temperature difference between the sample and the furnace thermocouple, thereby improving the furnace resonance and linearizing the temperature ramp.

We performed the sensitivity calibration using a Sapphire which has a melting temperature of 2303 K. The crucible to keep the test specimen is made of alumina. The heating rate is set to 40 K/min inorder to compare with literature values. With this heating rate the DSC thermogram reveals the heat flow characteristics of the samples more clearly. The calorimeter was calibrated for the heating rate using the melting transition of indium (In), Tin (Sn), Lead (Pb), Zinc (Zn) and gold (Au) in order to account for the temperature shift on the heating rate. The calibrated temperature ranges from 350 K to 1800 K.

The liquidus temperatures ($T_{liq}$) are compared with the reported values in the phase diagram [Pr03] in the case of binary alloys. For PdNiCuP and PdNiP alloys, which are glass forming, the glass transition temperature $T_g$, the crystallization temperature $T_k$ and liquidus temperature $T_{liq}$ are compared with the literature values [Ni02, Dr82]. These characteristic temperatures mentioned above are very sensitive

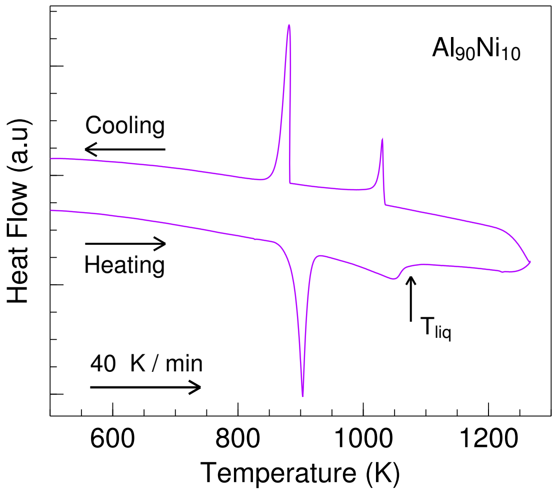

Figure 3.4: The DSC scan of $Al_{90}Ni_{10}$. It shows exothermic liquidus temperature $T_{liq}$ at 1033 K and is in excellent agreement with the phase diagram. The peak on cooling shows the endothermic recrystallization temperature.

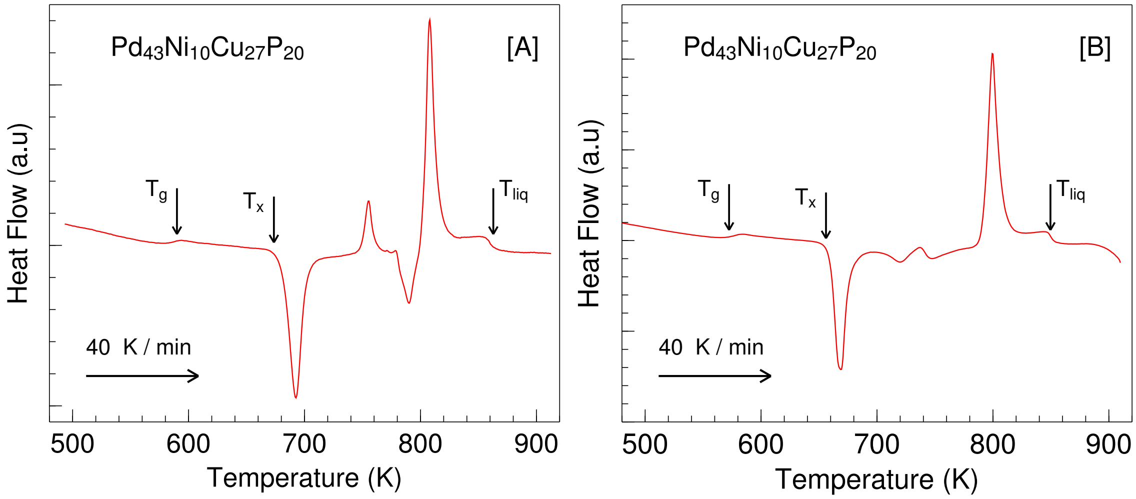

Figure 3.5: [A]The characteristic temperatures of $Pd_{43}Ni_{10}Cu_{27}P_{20}$ metallic glass shows the glass transition temperature, $T_g$ at 578 K, a sharp crystallization peak at 671 K and a liquidus temperature at 883 K. [B] The heat flow characteristic between $T_x$ and $T_{liq}$ change drastically because of a small variation in the Phosphorus content.

to the compositions. Any change in composition will be reflected in the DSC thermogram (see figure 3.5[B]). This can readily be noticed and any change in composition can be determined.

Figure 3.4 shows the heat flow characteristics of the $Al_{90}Ni_{10}$ alloy while heating and cooling as seen from DSC scans with a temperature ramp of 0.66 K $s^{-1}$. The endothermic peak at 909 K corresponds to the melting of the $Al_3Ni$ crystalline phase. At 1075 K $Al_{90}Ni_{10}$ becomes completely liquid (liquidus temperature, $T_{liq}$). On cooling, the peaks correspond to the recrystallization temperatures.

Figure 3.5[A] represents the DSC thermogram of $Pd_{43}Ni_{10}Cu_{27}P_{20}$ glass. A small endothermic kink at 578 K is the calorimetric glass transition temperature. A sharp exothermic peak at 671 K corresponding to the crystallization of the metallic glass, called the crystallization peak $T_x$. The intermediate small endothermic and exothermic peaks before the melting of the alloy is due to structural changes. The alloy is completely liquid at 862 K, which is the liquidus temperature $T_{liq}$. These temperatures are very sensitive to the composition. The reported characteristic temperatures of $Pd_{43}Ni_{10}Cu_{27}P_{20}$ taken from the sample which was characterized for composition beforehand by wavelength-dispersive spectrometer (WDS) [Sc00]. In the case of $Pd_{40}Ni_{40}P_{20}$ the intermediate peak is due to the transition which is correlated with a change of magnetic properties, above this temperature the sample is paramagnetic and below ferromagnetic [Wi94]. Table 3.1 gives the results of the DSC measurements on the alloys investigated.

| *Alloys* | $T_g$ (K) | $T_x$ (K) | $T_{liq}$ (K) |
|---|---|---|---|
| $Ni_{80}P_{20}$ | 612±0.5 | 643±0.5 | 1171±2 |
| $Pd_{40}Ni_{40}P_{20}$ | 577±0.5 | 669±0.5 | 972±0.6 |
| $Pd_{43}Ni_{10}Cu_{27}P_{20}$ | 570±0.5 | 671±0.5 | 863±0.5 |
| $Al_{90}Ni_{10}$ | — | — | 1073±1 |
| $Al_{80}Ni_{20}$ | — | — | 1263±2 |
| $Al_{77}Ni_{23}$ | — | — | 1343±2 |
| $Al_{70}Ni_{30}$ | — | — | 1528±2 |
| $Al_{80}Cu_{20}$ | — | — | 833±1 |
| $Al_{87}Ni_{10}Ce_3$ | — | — | 1073±1 |
| $Al_{77}Ni_{20}Ce_3$ | — | — | 1284±2 |
| $Al_{70}Ni_{27}Ce_3$ | — | — | 1528±2 |
| $Al_{84}Ni_{10}Ce_6$ | — | — | 1188±1 |
| $Al_{87}Ni_7Ce_6$ | — | — | 1028±1 |
| $Al_{77}Ni_{11}Ce_{12}$ | — | — | 1268±2 |

Table 3.1: Transition temperatures of alloys observed by differential scanning calorimetry.

## 3.6 Sample holder

The sample holder (Figure 3.6) we used for the scattering experiments is made of alumina ($Al_2O_3$). It has the geometry of a hollow cylinder. The height of the sample holder is 40 mm. The outer diameter is 22 mm and the inner cylinder diameter varies from 20.8 to 21.4 mm. So the sample thickness can be chosen either 1.25 mm or 0.6 mm. The $Al_2O_3$ sample holders are produced by Wesgo ceramic GmbH, Erlangen.

$Al_2O_3$ is used because

- Aluminum and Oxygen possess negligible neutron incoherent and absorption scattering cross sections
- It has a high melting temperature, $T_m = 2200$ K
- The alloys investigated were found to be not reacting with alumina (see figure 3.7)

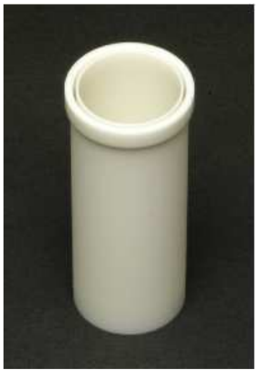

Figure 3.6: The sample holder used for neuron scattering experiments. It is made of alumina($Al_2O_3$) and has the shape of a hollow cylinder. The sample filling area is the region between the inner and outer cylinders.

The first mentioned properties make the sample holder fairly transparent to the cold neutrons used in the experiments and the later properties suitable for keeping the alloys at their liquid state for a long time. The hollow cylindrical geometry is chosen because, it makes the handling of the self absorption correction straight forward. The size of the sample holder matches with the neutron beam size at the sample position for the instruments FOCUS at PSI and IN6 at ILL, so that we can make use of the maximum available neutron flux. The prepared alloys were powdered (about 0.5 $mm^3$ size particles) and filled into the sample holder. For a complete filling, we repeated the process of filling of the powdered alloy and melting in a vacuum furnace 2 - 3 times. Approximately 8 to 12 grams of prepared alloys were used for each experiments.

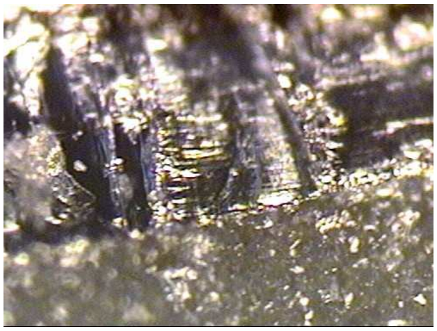

Figure 3.7: The interface between the $Al_2O_3$ sample holder and the $Al_{80}Ni_{20}$ sample after the experiment investigated by a microscope (magnification = 5X). A clean interface indicates that there is no reaction between the sample and $Al_2O_3$ at high temperatures.

# Chapter 4

# Inelastic neutron scattering

*Summary : The theory of neutron scattering, evaluation of self-diffusion coefficients from inelastic neutron scattering, experimental methods and the instruments used for the measurements are presented in this chapter.*

## 4.1 Introduction

The neutron time-of-flight technique has a long and distinguished history. In 1935, only three years after the discovery of neutrons, a pair of rotating discs were used to "prove by direct measurement that many of slow neutron are in thermal velocity range" [Du35]. With the advent of nuclear reactors (in 1942) more difficult measurements became possible, and a very different type of chopper was used by Enrico Fermi to determine the energy dependence of the absorption cross section of Boron [Fe47]. From the mid sixties the emphasis has been shifted to the study of more and more complicated materials. Several kinds of time-of-flight instruments have been developed in order to make possible many different type of experiments, mainly to study the excitations in solids and liquids [Be88, Wi81].

## 4.2 Neutron scattering - Theory

From the theoretical point of view the basic quantity measured from a neutron scattering experiment is the number of scattered neutrons with respect to its momentum $\hbar q$ and energy $\hbar\omega$ exchange with the sample. In terms of the incident and scattered wave vectors, $k_i$ and $k_f$, the wave vector transfer $q$ is given by $q = k_f - k_i$ and the magnitude of the momentum and energy transfer is related to:

$$q^2 = |k_i|^2 + |k_f|^2 - 2|k_i||k_f|\cos 2\theta \tag{4.1}$$

$$\hbar\omega = \hbar^2/2m_n(|k_f|^2 - |k_i|^2) \tag{4.2}$$

where $|k_i| = \sqrt{2m_nE_i/\hbar^2}$ and $|k_f| = \sqrt{2m_n(E_i + \hbar\omega)/\hbar^2}$. The scattering intensity is then described by a double differential scattering cross section $d^2\sigma/d\Omega dE$. $2\theta$ is the angle between $k_i$ and $k_f$, the scattering angle. This cross section is related to experimental quantities as follows: The number of counts at the detector $I$ is proportional to the time averaged neutron flux at the sample $\Phi_n$, the number of atoms in the beam $N$, the detector solid angle $\Delta\Omega$, the detector efficiency $f$, and finally the width of the energy channel $\Delta E$.

$$I = \Phi_n N \Delta\Omega f \Delta E \left(\frac{d^2\sigma}{d\Omega dE}\right) \tag{4.3}$$

Suppose the solid is made up of one kind of atoms, there will generally be still various isotopes present and each of these will be characterized by a distinct *scattering length*, $b_i$ which gives the (isotopic) scattering cross-section for neutrons from the single nucleus of that type, namely $4\pi b_i^2$. The presence of different isotopes distributed randomly in the sample means that the total scattering is made up of two parts, called the *coherent* and the *incoherent*. A quantity that is completely independent of the details of scattering experiments but containing the physics of the samples under investigation that is related to the double differential cross section and is given by:

$$\frac{d^2\sigma}{d\Omega dE'} = \frac{|\ k'\ |}{|\ k\ |} N \left(\frac{\sigma_{coh}}{4\pi} S_{coh}(q,\omega) + \frac{\sigma_{inc}}{4\pi} S_{inc}(q,\omega)\right) \tag{4.4}$$

where $k'$ and $k$ are the modulus of scattered and incoming beam, respectively. $N$ denotes the total number of atoms in the sample and $b_i$ is the scattering length. $\sigma_{coh} \propto \langle b_i^2 \rangle$ and $\sigma_{incoh} \propto \langle (b_i - \langle b_i \rangle)^2 \rangle$. This allows to select between the coherent and incoherent scattering processes, depending on the isotope at the samples.

The scattering function $S(q,\omega)$ or $S_{inc}(q,\omega)$ also called dynamic scattering law contains all the physics of the target. The dynamic scattering function represents the space and time Fourier transform of correlation functions,

$$S_{coh}(q,\omega) = \frac{1}{2\pi\hbar} \int G(r,t) e^{i(q.r - \omega t)} \mathrm{d}\mathbf{r}\mathrm{d}t \tag{4.5}$$

$$S_{inc}(q,\omega) = \frac{1}{2\pi\hbar} \int G_s(r,t) e^{i(q.r - \omega t)} \mathrm{d}\mathbf{r}\mathrm{d}t \tag{4.6}$$

where $G(r,t)$ and $G_s(r,t)$ are pair and self correlation functions. The physical interpretation of the function $G(r,t)$ d$\mathbf{r}$ is proportional to the probability of finding a particle $i$ in a region d$r$ around a point $\mathbf{r}$ at time $t$ given that there was a particle $j$ at the region at time $t = 0$; the division into self and distinct parts corresponds to the probabilities that $i$ and $j$ may be the same particle or different one. The intermediate scattering functions which are the space Fourier transform of the correlation functions are:

$$I(q,t) = \int G(r,t) e^{i(\mathbf{q}\cdot\mathbf{r})} \mathrm{d}\mathbf{r} \tag{4.7}$$

$$I_s(q,t) = \int G_s(r,t)e^{i(\mathbf{q}\cdot\mathbf{r})}\mathrm{d}\mathbf{r} \tag{4.8}$$

Fourier transformation of $I(q,t)$ with respect to time will then generate the dynamic scattering function.

$$S(q,\omega) = \frac{1}{2\pi\hbar}\int I(q,t)e^{-i\omega t}dt \tag{4.9}$$

$$S_{inc}(q,\omega) = \frac{1}{2\pi\hbar}\int I_s(q,t)e^{-i\omega t}dt \tag{4.10}$$

As stated above, the scattering function $S(q,\omega)$ is the space and time Fourier transform of a pair correlation function. With coherent scattering, collective phenomena such as Bragg reflections and phonons are observed. The incoherent scattering function $S_{inc}(q,\omega)$ being the space and Fourier transform of the self correlation function, conform information on diffusive motion.

### 4.2.1 Diffusive motion

In inelastic neutron scattering, the partial differential scattering cross section contains both elastic and inelastic contributions. In the liquids or glassy materials, at Bragg reflection condition elastic scattering without energy loss occurs. Dynamic wave like excitations, such as phonons and spin waves give rise to inelastic peaks among the Bragg diffraction peaks. In the case of diffusive motion, the movements are stochastic and relatively slow. They are observed as diffusive scattering around elastic Bragg peaks called, quasielastic scattering. Theoretically, the self-diffusion coefficient from quasielastic neutron scattering is obtained as follows.

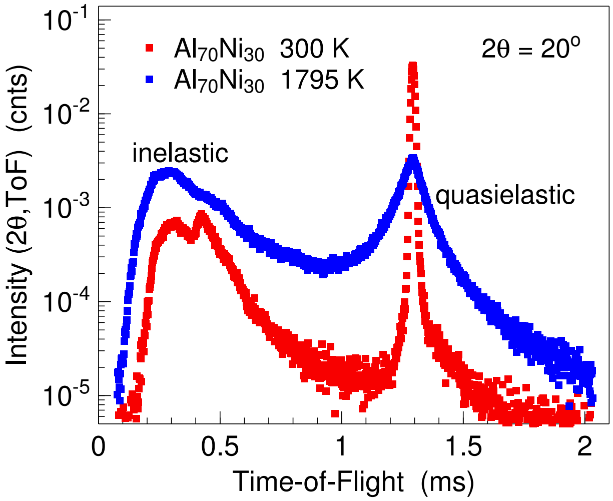

Figure 4.1: Inelastic neutron scattering spectra: a sharp elastic peak and broad peak at smaller time of flight shows that neutrons gained energy from phonons. The elastic peak is broadened ($Al_{70}Ni_{30}$ = 1795 K) due to quasielastic contributions from diffusive motions.

The basic equation governing the random diffusion is given by Fick's law:

$$\frac{\partial\rho}{\partial t} = D\nabla^2\rho(r,t) \tag{4.11}$$

where $D$ is the self-diffusion coefficient and $\rho$(r,t) is the particle density. $G_s(r,t)$ is the solution to the diffusion equation

$$\frac{\partial G_s}{\partial t} = D\nabla^2 G_s \tag{4.12}$$

spatial Fourier transform :

$$\frac{\partial I_s(q,t)}{\partial t} + D\,q^2\,I_s(q,t) = o \tag{4.13}$$

solution of 4.13

$$\Phi_s = I_s(q,t) = e^{-q^2 Dt} \tag{4.14}$$

with $I_s(q,0) = 1$ and Fourier transform yields the incoherent scattering function for diffusive motion:

$$S_{inc}(q,\omega) = \frac{1}{\pi\hbar}\frac{Dq^2}{(Dq^2)^2 + \omega^2} \tag{4.15}$$

Thus for diffusive motion of particles the incoherent quasielastic cross section has a Lorentzian shape with a FWHM of:

$$\Gamma_{inc} = 2\hbar Dq^2 \tag{4.16}$$

Then the self-diffusivity is

$$D = \frac{\Gamma_{inc}}{2\hbar q^2} \tag{4.17}$$

## 4.3 Time-of-flight spectroscopy

The inelastic neutron scattering experiment at a steady source is performed in the following way. (i) Incident neutron energy $E_i$ is selected from the white beam in a small solid angle in the direction of $k_i$. (ii) The final energy of the scatted neutron $E_f$ is analyzed to determine the energy change $\hbar\omega = E_i$ - $E_f$. (iii) The scattering angle with respect to the incident beam is measured to determine the momentum transfer $q = k_i - k_f$.

In practice, these basic conditions are achieved because of the physical properties of the neutron. The wavelength of the neutron, $\lambda$, is related to its velocity, $v$, by $\lambda = h/mv$ with the neutron mass $m$ = 1.675 x $10^{-24}$g. Its energy, $E$, is given by:

$$E = \frac{1}{2}mv^2 \tag{4.18}$$

The neutron velocity varies from 500 to 14,000 meters per second, therefore the neutron flight time is easily determined by sufficient length scale. Neutrons obey

Bragg's law, when diffracted by a single crystal. Bragg's law gives the relationship between wavelength, $\lambda = h/mv$, and the diffraction angle $\theta$.

$$\lambda = 2d_{hkl}sin\theta \tag{4.19}$$

condition (i) is achieved by using a mechanical velocity selector like rotating phase chopper. Condition (ii) is obtained by connecting the neutron velocity to its energy by measuring the time of flight $\tau = L/v$ and condition (iii) is fulfilled by counting the scattered neutron with a detector at accurate scattering angles.

The basic quantity measured in a time-of-flight experiment is a set of intensities $I(\theta_i, t_i)$ at $N$ detectors located at a scattering angle $\theta_i$, in $n_i$ channels centered at time $t_j(j = 1, 2, ..)$ relative to an appropriate starting time. The information that may be obtained from a neutron scattering experiment can be expressed in terms of the scattering function $S(q, \omega)$, that contains all the information accessible by the scattering experiment.

## 4.4 Experiments at IN6 and FOCUS

There are several types of neutron spectrometers that are designed to measure excitations in materials. Each of these spectrometers have an energy range $E$ and a related wave-vector range $Q$ over which it can measure excitations, with an associated energy and wave-vector resolution. The choice of the spectrometer is determined by how these capabilities match the excitations of interest. Figure 4.2 gives an idea about accessible space and time range of each method and the related scientific problems.

As one can see from figure 4.2, diffusional dynamics can be best studied by cold neutron chopper time-of-flight techniques. We performed most of our experiments at the IN6 time-of-flight spectrometer at the ILL. IN6 is a time focusing time of flight spectrometer with incident wave lengths ranging from 4.1 to 5.9Å and is designed for quasielastic and inelastic experiments. Figure 4.3 shows a schematic view of the IN6 spectrometer at the ILL. An intense beam is extracted from the H15 neutron guide by a vertically focusing monochromator array. It consists of three composite pyroelectric graphite monochromators that make of use the full height (20 cm) of the guide and that focus the beam down to the sample position. The second-order reflection from the graphite monochromator is removed by a beryllium filter cooled at liquid nitrogen temperature. The chopper system consists of two choppers, the pulse chopper and a suppressor chopper. Both have the so called "Fermi geometry", i.e, they have got a small slot length to ensure a good transmission and are rotating around a vertical rotating axis. By selecting the appropriate angular velocity of these two choppers, one can suppress the neutrons from $n+1$ and $n-1$ cycles. The

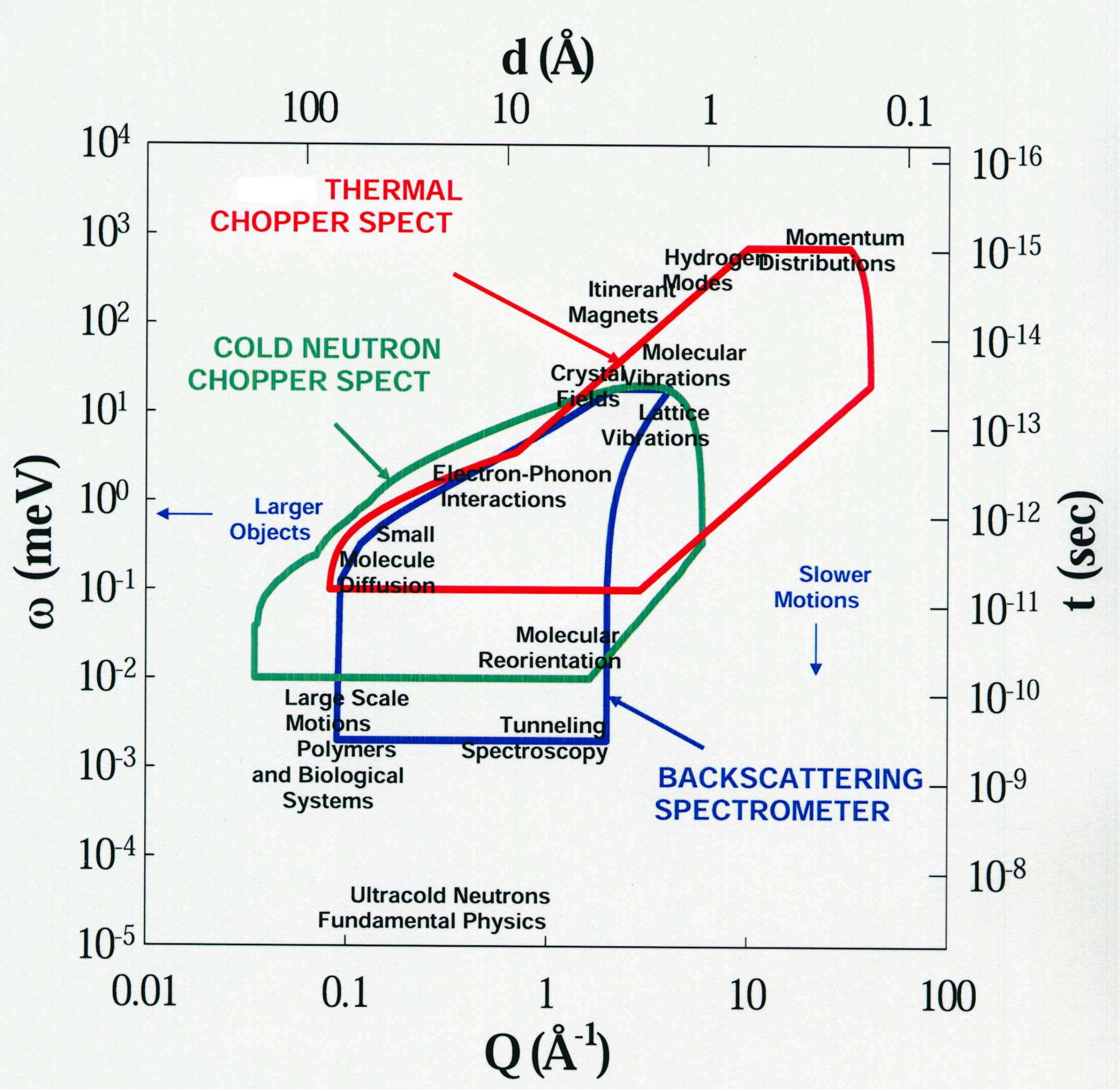

Figure 4.2: An over view of time and space covered by various time of flight neutron scattering techniques (source: NIST neutron scattering center).

relation between the two angular velocities of the chopper is called the ratio. The detector counts the neutrons arriving at a certain detection time interval $\Delta\tau$ in the time channel $n$, with an energy width $\Delta E$, and the absolute flight time is given by:

$$t = n\Delta\tau \tag{4.20}$$

The energy transfer in the sample is given by

$$\hbar\omega = E_i - \frac{1}{2}m_n\left(\frac{L}{L\sqrt{m_n/2Ei} + \Delta n\Delta\tau}\right)^2 \tag{4.21}$$

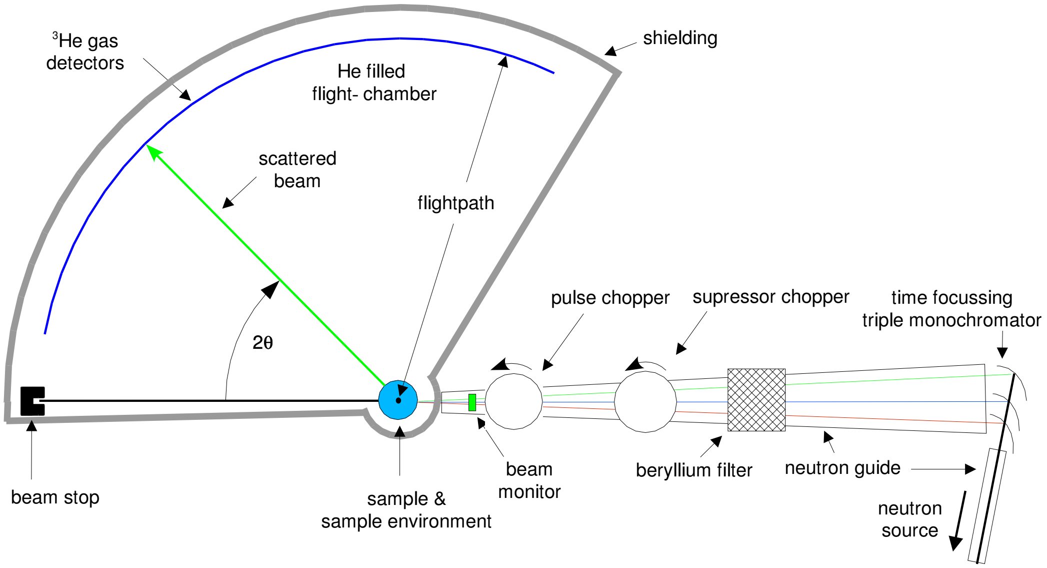
³He gas detectors
He filled flight- chamber
shielding
scattered beam
flightpath
2θ
pulse chopper
supressor chopper
time focussing triple monochromator
beam stop
sample & sample environment
beam monitor
beryllium filter
neutron guide
neutron source

Figure 4.3: Schematic of IN6 at ILL, Grenoble

with the incident neutron energy $E_i$, the neutron mass $m$ and the flight path $L$ from the sample to detector which is 2.43 m in the case of IN6 and 2.5 m in FOCUS. $\Delta n$ is the difference between the flight path number $n$ and the flight path number $n_{el}$ of the elastic channel.

### 4.4.1 Neutron wavelength

For elastic scattering, the neutron wavelength $\lambda$ and the $q$ space covered is given by

$$q = \frac{4\pi}{\lambda} sin\theta \tag{4.22}$$

According to this equation to cover a small $q$ range one should select higher $\lambda$. IN6 operates only at four wavelengths: 4.1, 4.6, 5.1, and 5.9Å. The available neutron flux varies considerably between the four possible wavelengths. To have an optimum $q$ value and neutron flux, we have chosen $\lambda = 5.1$ Å for our experiments. Also at 5.1Å no Bragg peaks from the sample environment, only one Bragg peak from sample container is observed and is the advantageous of this wavelength. The full $q - \omega$ domain assessable on IN6 for the wavelength 5.1 Å is shown in figure 4.4. The chopper phases are mostly chosen so that all elastically scattered neutrons reach the detector at the same time(elastic focusing). This corresponds to a chopper phase of one.

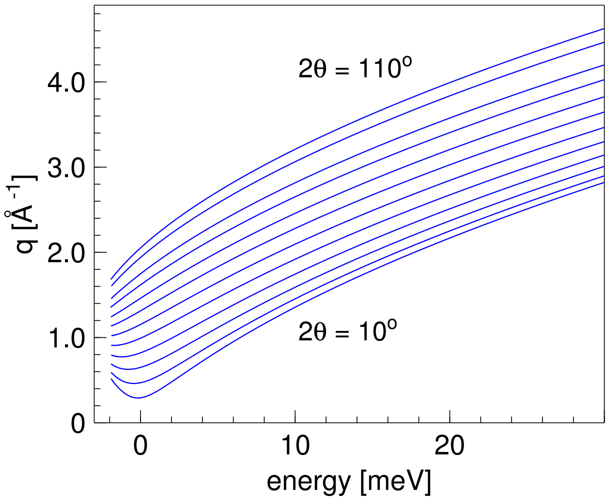

Figure 4.4: The $q$-$\omega$ domain of the ILL time-of-flight spectrometer IN6 at a wavelength 5.1 Å.

### 4.4.2 Sample environment

In our experiments a high temperature resistance furnace made of Nb was used, which is the highest possible temperature furnace available at ILL. In fact, this furnace was calibrated *in situ* with the melting temperature of the Ni and $Ni_{80}P_{20}$ samples. The temperature in this furnace is stable within ± 0.5 degrees at high temperatures. At FOCUS, the high temperature limit is 1400 K, this made us to limit the measurement of $Pd_{40}Ni_{40}P_{20}$ below this temperature. The sample box at IN6 is equipped with an oscillating collimator which prevents parasitic reflections (from the furnace walls for example) reaching the detectors. The furnace and collimator keeping area is evacuated to reduce background in IN6. At FOCUS collimator is kept open, this is one of the reasons why the spectra from FOCUS show high background.

Unfortunately the experiments are currently restricted to a temperature below 1800 K. Most of the alloys melt at higher temperatures. To measure a temperature dependence of self-diffusion coefficients and to get an activation energy in a reasonable precision, one needs to measure samples even at elevated temperatures. For choosing the material for the sample container, the ratio of neutron scattering from the sample container and from the sample itself should be as small as possible and self-absorption and multiple scattering have to be minimized. For these reasons, a hollow $Al_2O_3$ cylinder with sample thickness about 1mm was used.

### 4.4.3 The samples

The samples investigated are the alloys of elements: Al, Ni, Pd, Cu, P and Ce. The neutron coherent and incoherent scattering cross section and absorption cross sections of the elements are given in the table 4.1.

As seen from the table 4.1, the signals in our experiments are dominated by

| *Element* | $\sigma_{coh}$ (barns) | $\sigma_{inc}$ (barn) | $\sigma_{abs}$ (barn) |
|---|---|---|---|
| Al | 1.495±0.004 | 0.0082±0.0006 | 0.231±0.003 |
| Ni | 13.3±0.3 | 5.2±0.4 | 4.49±0.16 |
| Pd | 4.39±0.09 | 0.093±0.09 | 6.9±0.4 |
| Cu | 7.485±0.008 | 0.55±0.03 | 3.78±0.02 |
| Ce | 2.94±0.02 | 0.00±0.01 | 0.63±0.04 |
| P | 3.307±0.013 | 0.005±0.001 | 0.172±0.006 |

Table 4.1: Neutron coherent $\sigma_{coh}$, incoherent scattering cross sections $\sigma_{inc}$ and absorption cross sections $\sigma_{abs}$ of elements [Be88].

incoherent scattering from Ni. For pure Ni sample and samples with high Ni content ($Ni_3Al$, $Ni_{80}P_{20}$) we used a sample thickness of 0.6 mm for the measurements. This is to reduce the multiple scattering. For all the other alloys a sample thickness of 1.25 mm was found to be a good compromise for multiple scattering and scattered intensities. For the chosen wavelength and sample geometry all the samples scattered less than 5% of the incoming beam. Therefore, multiple scattering which would alter the data especially towards low $q$ [Wu00], only has negligible effect. The ILL IN6 experiments, with one to four hours scattering at each temperature give good statistics of the data whereas it requires more than 10 hours to obtain sufficient statistical data quality at FOCUS, PSI.[1]

---

[1] details of experiment can be found in appendix B

# Chapter 5

# Data reduction

*Summary : This chapter presents the details of the neutron time-of-flight data analysis to obtain the intermediate structure factor, density correlation functions and accurate self-diffusion coefficients.*

## 5.1 Raw data reduction

The primary step in the analysis of inelastic or quasielastic neutron scattering data is the reduction of the recorded neutron count rate as a function of time-of-flight and scattering angle to the scattering law $S(q, \omega)$. This is done by IDA (Ingenious Data Analysis) a software originally developed by Dr. Jachim Wuttke and maintained in our group. IDA is written in Fortran and data from neutron time-of-flight instruments, back scattering, spin-echo and chopper spectrometers can be analyzed.

Time-of-flight raw data files contain the wavelength, the number of channels, the channel width in picoseconds, chopper speed and the detector angles. The first step in reading in the raw data is to assign the spectral values and the channels for the flight time. To determine the elastic peak from the time-of-flight spectrum, the room temperature spectrum is selected and plotted as intensity versus time-of-flight, as shown in figure 5.1. The spectra shown are that of $Al_2O_3$ empty cell and $Al_{70}Ni_{30}$ which are standardized to the monitor counts and measured at a wavelength of 5.1 $Å^{-1}$. The time-of-flight varies from 0.1 to 2.0 ms $m^{-1}$. The shown spectrum is summed up in all angles. At 1.3 ms $m^{-1}$ a high intensity peak is observed that represents the elastic peak. Around 0.3 ms $m^{-1}$ the broad spectrum is due to scattering on phonons. The neutrons gained energy while scattering on the vibrating atoms.

In a multi-detector spectrometer, the detectors are fixed at angle $\theta_k$. $2\theta$ is defined as the angle between incoming and scattered beam. Let $\Delta t_j$ be the time width of channel $j$ centered at energy $\omega_j$ with a width $\Delta tof$. The incoming neutron flux

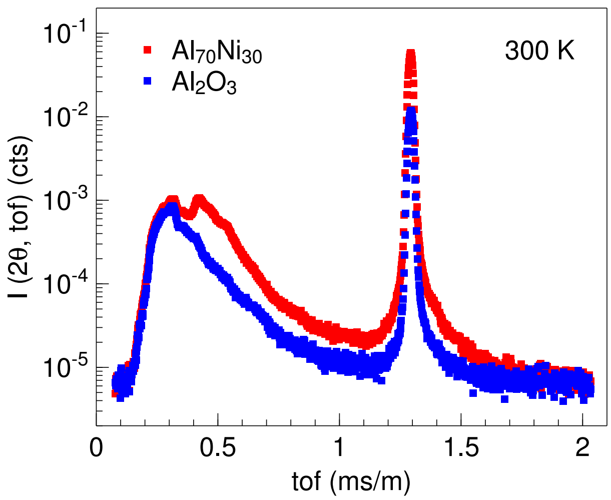

Figure 5.1: Shows the time of flight spectrum of $Al_{70}Ni_{30}$ and that of Alumina sample container. The sharp peak at 1.3 ms m$^{-1}$ is the elastic peak. The wavelength $\lambda = 5.1$ Å.

$\Phi_n(E_i, t_j)$ is measured by the monitor. The number of counts at the monitor will be

$$N_{m,j} = p_m A_m \Phi_n(E_i, t_j) \Delta t_j \tag{5.1}$$

where $p_m$ is the monitor efficiency at energy $E_i$, $A_m$ is the monitor area. During the same interval $\Delta t_j$, the number of scattered neutrons counted in the detector $k$ is $N^{S+C}_{m,j}$. Then the intensity of scattered beam due to sample and container is given by

$$I_{S+C}(2\theta_k, tof) = \frac{N^{S+C}_{m,j}}{p_k A^s_i \Phi_n(E_i, t_j) \Delta\Omega_k \Delta tof} \tag{5.2}$$

where $p_k$ is the detector efficiency and $A^S_i$ is the sample area illuminated by the beam.

The count rate at the detector should be normalized because the number of neutrons from the source can vary in time. For this purpose a transparent neutron counter (monitor) is placed in the neutron flight path. The neutron counts at the detector is then normalized with monitor counts by

$$\bar{N}^{S+C}_{k,j} = \frac{N^{S+C}_{k,j}}{N_{m,j}} = \frac{p_k \Delta\Omega_k}{p_m A_m} A^s_i I_{S+C}(2\theta, tof) \Delta tof \tag{5.3}$$

where $\bar{N}^{S+C}_{k,j}$ is the number of scattered neutrons from the sample and the container and $N_{m,j}$ is the monitor counts, $p_m$ is the monitor efficiency, $A_m$ is the monitor area.

In IN6 at ILL there are 337 $^3$He filled detectors to collect the scattered neutrons. These detectors might possess different counting efficiencies for neutron because the $^3$He pressure in the detector may vary. The detector efficiency must be corrected for a fair data analysis. The detector efficiency can be corrected by normalizing the inelastic data with a dominant incoherent scatterer. For this purpose Vanadium, which has a negligible coherent and a high incoherent scattering cross sections ($\sigma_c$

= 0.02 barn, $\sigma_i$ = 5.2 barn), in identical scattering geometry as for the sample was chosen. The scattering from the Vanadium is given by

$$I_V^{tot}(2\theta, tof) = n_V z_V \frac{\sigma_i^V}{4\pi} e^{-2W(q)} \tag{5.4}$$

where $n_V$ is the number density of vanadium and $z_V$ is the path length of the transmitted beam through the sample. The sample or container transmissions can be calculated as $T_S$ = exp(-$n_S z_S \sigma_{tot}$). For hollow cylindrical samples, the average path length $z_S$, in good approximation for small $\sigma$, is $\pi d$, where $d$ is the wall thickness of the sample. If the number of counts due to Vanadium is $N_{k,tot}^V$, the scattered intensity of sample and container is obtained by

$$\bar{I}_{S+C}(2\theta, tof) = \frac{\bar{N}_{k,j}^{S+C}}{N_{k,tot}^V} \frac{A_i^V}{A_i^S} \frac{I_V^{tot}(2\theta, tof)}{\Delta tof} \tag{5.5}$$

The above steps are also performed to obtain absolute scattering intensity from the container, $\bar{I}_C(2\theta, tof)$. The double differential cross section is related to the counts rate as

$$\frac{\mathrm{d}^2\sigma}{\mathrm{d}\Omega\mathrm{d}\omega} = \frac{\mathrm{d}^2\sigma}{\mathrm{d}\Omega\mathrm{d}tof} \cdot \left|\frac{\mathrm{dtof}}{\mathrm{d}\omega}\right| \tag{5.6}$$

The relation between energy $\omega$ and flight time, $tof$

$$\left|\frac{\mathrm{dtof}}{\mathrm{d}\omega}\right| = \frac{\mathrm{tof}^3}{m_n} \tag{5.7}$$

where $m_n$ is the mass of the neutron. The experimentally determined scattered intensity $\bar{I}(2\theta, tof)$ is related to the double differential scattering cross section as,

$$\frac{\mathrm{d}^2\sigma}{\mathrm{d}\Omega\mathrm{d}tof} = A\,\bar{I}(2\theta, \mathrm{tof}) \tag{5.8}$$

where $A$ is a constant related to the absorption of neutrons by sample and container, and

$$\frac{\mathrm{d}^2\sigma}{\mathrm{d}\Omega\mathrm{d}\omega} = \frac{|k_f|}{|k_i|} \cdot \frac{\sigma_{inc}}{4\pi} \cdot S(2\theta, \omega) \tag{5.9}$$

From equation 5.7, 5.8 and 5.9 it follows

$$S(2\theta, \omega) = \frac{|k_i|}{|k_f|} \cdot \frac{4\pi}{\sigma_{inc}} \cdot \frac{tof^3}{m_n} \cdot A\,\bar{I}(2\theta, tof) \tag{5.10}$$

The absolute scattered intensity from the container $\bar{I}_S(2\theta, tof)$ and from the sample plus container $\bar{I}_{S+C}(2\theta, tof)$ are then transformed to $S_C(2\theta, \omega)$ and $S_{S+C}(2\theta, \omega)$, respectively.

To see any Bragg reflections from the sample or from the container, the function $S(2\theta, \omega)$ was integrated over the elastic line. The resultant spectra are shown in the figure 5.2. For the chosen wavelength, 5.1Å the $Al_2O_3$ sample container shows a Bragg's reflection at an angle $2\theta = 95°$ (fig. 5.2). The spectra contain Bragg reflections were deleted from further data analysis.

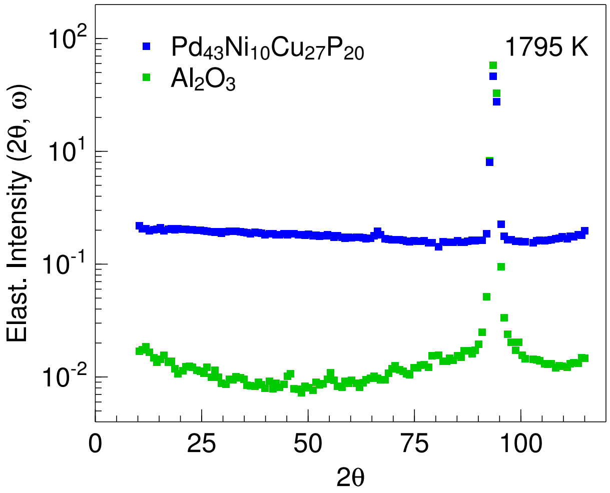

Figure 5.2: A Bragg peak from the sample container at $2\theta = 95°$. The blue spectrum is the sample plus container and the green is that of the sample container only.

## 5.2 Self-absorption correction

A simple subtraction of signals due to scattering from the container and from the sample (sample plus container) is not feasible since such a treatment would not take into account shielding due to absorption and scattering. This leads to shielding of the container by the sample and shielding of the sample on the container. Paalman and Prings were the first to suggest a proper self-absorption correction procedure [Pa62]. The value for $S(2\theta, \omega)$ corrected for self absorption from the sample $S$ in a container $C$ is given by

$$S_S(2\theta, \omega) = \frac{1}{A_{S,SC}(2\theta, \omega)} S_{S+C}(2\theta, \omega) - \frac{A_{C,SC}(2\theta, \omega)}{A_{S,SC}(2\theta, \omega) A_{C,C}(2\theta, \omega)} S_C(2\theta, \omega) \quad (5.11)$$

where $S_{S+C}$ is scattering from the sample and the container and $S_C$ that from the container only,

| | |
|---|---|
| $A_{C,C}(\theta, \omega)$ | is the correction factor for scattering and self absorption in the container. |
| $A_{C,SC}(\theta, \omega)$ | is the correction factor for scattering from the container and absorption in both sample and container. |
| $A_{S,SC}(\theta, \omega)$ | is the correction factor for scattering from the sample and absorption in both sample and container |

The fraction $A_{C,SC}(\theta, \omega)/A_{S,SC}(\theta, \omega)$ can be grouped to a coefficient called $A_{rel}$. If $A_{S,SC}(\theta, \omega)$ is defined as $A_1$ and $A_{rel}/A_{C,C}(\theta, \omega)$ as $A_2$, the corrected scattering function is then

$$S_S(2\theta, \omega) = A_1(2\theta, \omega) S_{S+C}(2\theta, \omega) - A_2(2\theta, \omega) S_C(2\theta, \omega) \quad (5.12)$$

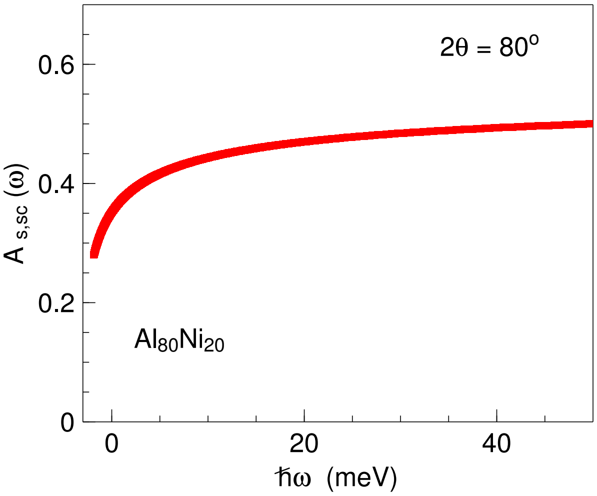

Figure 5.3: $A_{S,SC}(\omega)$ for $\mathrm{Al}_{90}\mathrm{Ni}_{10}$ at a scattering angle $2\theta = 80^0$ versus energy transfer $\hbar\omega$.

The sample thickness is chosen in accordance that the total scattering from the sample is less than 5% of incoming flux, then the mutiple scattering from the sample is negligible. The $S_S(2\theta, \omega)$ is then interpolated to constant $q$ to obtain $S_S(q, \omega)$.

In the limit of small energy and small momentum transfer the scattering function behaves classically *i.e.* for long time $t$ and large value of $r$. Conversely, for short times (large energy transfer) and small distance (large momentum transfer), quantum effects are not negligible. In general, it is not possible to carry out quantum mechanical calculations from the atomic properties of the scattering systems. Instead, the classically evaluated scattering function is derived from a physical model. In many cases, a very good approximation of the actual scattering function $S(q, \omega)$ is obtained by

$$S(q, \omega) = \exp\left(-\frac{\hbar\omega}{2k_BT}\right) S_S(q, \omega) \tag{5.13}$$

according to the detailed balance principle. The factor $\exp(-\hbar\omega/2k_BT)$ is then multiplied with $S_S(q, \omega)$ to obtain the scattering law $S(q, \omega)$. The scattering law for PdNiCuP is shown in the figure 5.4.

## 5.3 Quasielastic structure factor

Due to the restricted dynamic range permitted by the chosen wavelength and scattering angle, a complete static structure cannot be obtained neither from IN6 nor FOCUS. However, it is possible to obtain a quasielastic structure factor at intermediate $q$ values by integrating the scattering law over the elastic line:

$$S_{elast.}(q) = \int_{elast.line} S(q, \omega) d\omega. \tag{5.14}$$

The elastic structure factor is

$$S(q, \omega = 0) = S(q) f_q \tag{5.15}$$

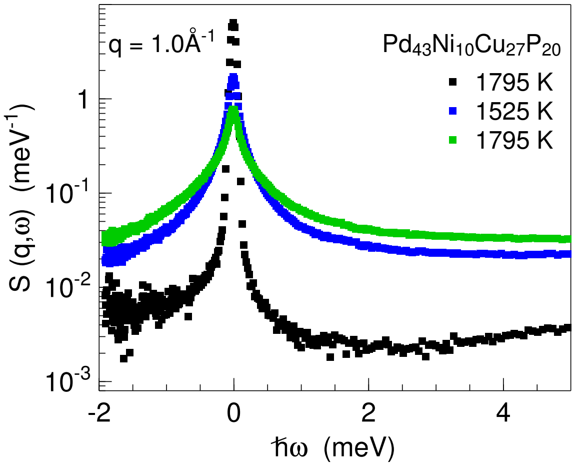

Figure 5.4: $S(q, \omega)$ for $Pd_{43}Ni_{10}Cu_{27}P_{20}$. The room temperature indicate the instrumental energy resolution. At high temperature the spectra are broadened due to quasielastic contributions from the diffusive motion of atoms

where $f_q$ is the Debye-Waller-Factor and $S(q)$ is equivalent to static structure factor. Figure 5.5 shows the the qusielastic structure factors obtained by integrating over the elastic line and subtracting the incoherent contribution from Ni. To subtract the incoherent contribution from Ni, the measured intensity is subtracted by a constant. The value of the constant is proportional to the mass of the Ni exposed to neutron beam. The spectrum indicates coherent scattering from CSRO. For $Al_{90}Ni_{10}$ the quasielastic structure factor has no change in intensity with $q$. The other Al-Ni alloy melts show an increasing intensity with increasing $q$. This variation in intensity indicates the presence of a prepeak in these systems.

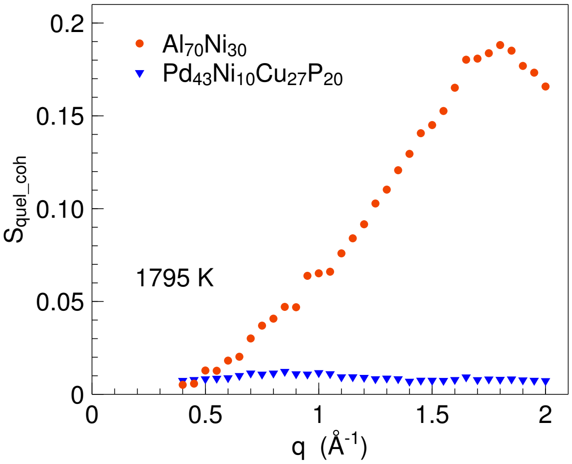

Figure 5.5: Quasielastic structure factors of $Al_{70}Ni_{30}$ and $Pd_{43}Ni_{10}Cu_{27}P_{20}$ melts at 1795 K.

## 5.4 Self-diffusion coefficient

There are two possible ways to calculate the self-diffusion coefficients from inelastic neutron scattering. The first possibility is to calculate from full width at half maximum (FWHM), $\Gamma_{inc}$ of the dynamic structure factor $S_s(q, \omega)$, by the equation

4.19. The second possibility is to obtain mean relaxation time $\langle\tau_q\rangle$ from the density correlation function $\Phi(q,t)$. Then from the plot of $q^2$ versus $1/\langle\tau_q\rangle$, the slope of the line gives the self-diffusion constant (lim $q \rightarrow 0$, $D = 1/\langle\tau_q\rangle q^2$). The first method is not adopted because of the finite energy resolution of the spectrometers and the relaxation process is not always a simple exponential function.

The density correlation function is obtained by Fourier transform of $S(q,\omega)$, divided with instrument energy resolution function and normalization to 1.

$$\Phi(q,t) = S_{exp}(q,t)/R(q,t) \tag{5.16}$$

where $R(q,t)$ is the Fourier transform of the instrumental energy resolution function. Ideally the sample should be at 0 K in order to obtain an accurate instrumental resolution function. Since measurements were done at 300 K, the data points below 1 ps were deleted and then interpolated to zero to approximate the real resolution function. Below 0.8 ps the data might be dominated by phonon and fast relaxation processes. The normalized resolution function $R(q,t)$ of IN6 at $q = 1.0$ Å$^{-1}$ is shown in the figure 5.6, at the wavelength $\lambda = 5.1$ Å. The instrumental energy resolution function is truncate at 50 ps (0.5 of $\Phi(q,t)$), corresponding to the limit of energy resolution of the instrument. $S(q,t)$ is then divided by $R(q,t)$ to obtain $\Phi(q,t)$.

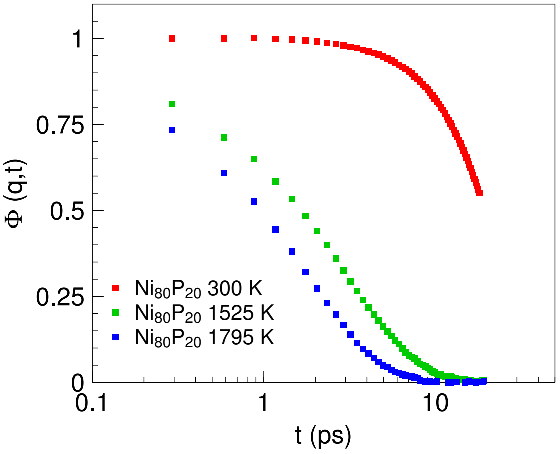

Figure 5.6: The figure shows the intermediate scattering function. The red curve is the instrumental energy resolution function measured at 300 K.

The intermediate scattering function $\Phi(q,t)$ decays to zero in most of the alloy melts around 20 ps in the low $q$ range. Due to this reason the data in the range of 0 to 20 ps were chosen for the analysis. To derive the $q$ dependence of the mean relaxation time from $\Phi(q,t)$, spectra are fitted with a stretched exponential function (Eq. 2.53). The variables in the fitting process are, '$a$', that correspond to Debye-Waller-Factor, the stretching exponent $\beta$ and the mean relaxation time $\langle\tau_q\rangle$. In the first fitting process the stretching exponent $\beta$ was treated as a free parameter and looked for a mean value. The further analysis was carried out with fixing this mean value for $\beta$. The data were fitted in a range from 0.80 ps to 20 ps. Below 0.8 ps the data might be dominated by phonon and fast relaxation processes. The

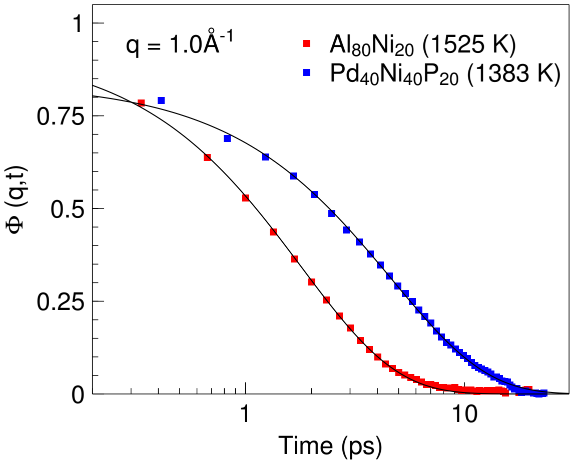

Figure 5.7: The figure shows the density correlation function $\Phi(q,t)$ of $Pd_{40}Ni_{40}P_{20}$ and $Al_{80}Ni_{20}$ at different temperatures fitted with the exponential function.

figure 5.7 shows the $\Phi(q,t)$ fitted with the exponential function. The $q^2$ dependence on mean relaxation time obtained from the analysis is plotted in figure 5.8 for $Pd_{40}Ni_{40}P_{20}$ melt. The slope of the line gives the self-diffusion coefficient $D$. From the hydrodynamic theory the validity of $q^2$ dependence should be applicable for small $q$ values only.

$$\lim_{q\to 0} \frac{1}{\langle\tau_q\rangle q^2} = D \tag{5.17}$$

For deriving the $D$ values, the data were fitted in the range 0.4 to 1 Å$^{-1}$. In dense liquids the $q^2$ dependence on mean relaxation time $\tau_q$ is found to be valid even at 1.8Å$^{-1}$ (figure 5.8).

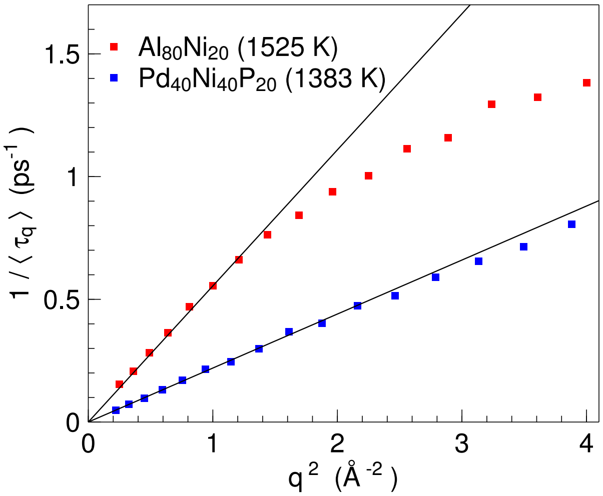

Figure 5.8: The figure shows the inverse of mean relaxation time $\langle\tau_q\rangle$ plotted against $q^2$. The data points are fitted with straight line and the slope of the line gives the self-diffusion coefficient $D$.

# Chapter 6

# Dynamics in dense metallic liquids

*Summary: The results of the investigation of the microscopic dynamics in dense metallic liquids are presented in this chapter.*

## 6.1 Introduction

An inelastic neutron scattering study on hard-sphere like $Pd_{43}Ni_{10}Cu_{27}P_{20}$ melts shows that the microscopic dynamics is well accordance with the mode-coupling theory [Me02]. From the MCT $\tau$ scaling law analysis the $T_c$ is found to be 700±30 K and is well above the calorimetric glass transition temperature, $T_g = 570$ K. Above $T_c$, the temperature dependence of the diffusion constant can be well described by the $\tau$ scaling law of MCT. Below $T_c$ it shows an Arrhenius type temperature dependence (see fig. 6.9). The diffusivity above the liquidus temperature is similar to that one found in simple metallic liquids [Me02]. In simple liquid alloys the microscopic mass transport is strongly dependent on composition and hence the thermodynamic properties [Sh85]. In dense metallic liquids the composition dependence of self-diffusion has not yet been studied. To understand the influence of composition or mixing effects on microscopic mass transport in dense metallic liquids, we studied Ni self-diffusion in liquid Ni, $Ni_{80}P_{20}$, $Pd_{40}Ni_{40}P_{20}$ and $Pd_{43}Ni_{10}Cu_{27}P_{20}$. As compared to simple metallic liquids, pure Ni and these glass forming alloy melts show a dense packing of atoms and packing fraction is as high as 0.5 at their respective melting temperature.

## 6.2 Thermophysical properties

### 6.2.1 Density

The density of liquid Ni has been measured by several authors with different techniques like the levitated drop, maximum bubble pressure and the direct Archimedean technique. The measured density shows a variation of 8.03 - 7.77 g cm$^{-3}$ at the melting point. Most reliable and recent measurements by Y. Sato *et. al.* [Sa00] and J. Brillo *et. al.* [Ju94] show a value of 7.82 ± 0.04 g cm$^3$ just above the melting temperature (1745 K). The packing density calculated using the equation 2.5 (hard sphere radius is taken as the covalent radius of Ni, 1.15 Å) indicates a high value and it is 0.51 at 1745 K. The density of $Ni_{80}P_{20}$ was measured by Y. Nishi and A. Yoshihiro [Ni85] using sessile drop technique in the temperature range from 1190 K to 1400 K. The packing fraction calculated from the density data at 1200 K indicates $Ni_{80}P_{20}$ is also a dense packed liquid, $\varphi = 0.50$. The specific volume of $Pd_{40}Ni_{40}P_{20}$ was measured by Chow *et. al.* [Ch93] in the temperature range 1000 K - 1196 K. The density obtained from this measurement shows a linear variation and it is best fitted with:

$$\rho(T) = 9.70 \pm 0.013 - (7.43 \pm 0.12) \times 10^{-4} T \text{ (g cm}^{-3}\text{)} \tag{6.1}$$

the density calculated from the above relation shows 8.96 g cm$^{-3}$ at 1000 K and gives a thermal expansivity of only 1.7%. In liquid $Pd_{43}Ni_{10}Cu_{27}P_{20}$ the thermal expansion and specific volume measured by Lu *et. al.* [Lu02] using the volume dilatometric method. The specific volume found to be varied linear with $T$ and the temperature dependence can be best fitted in the range 873 K - 1223 K by:

$$V_{liq}(T) = 7.8943 + 7.026 \times 10^{-4}(T - 293) \text{ (cm}^3\text{/mol)} \tag{6.2}$$

giving a constant coefficient of thermal expansion of 90 ± 3 × 10$^{-6}$ K$^{-1}$. The density obtained from his measurements is found to be 9.03 g cm$^{-3}$ at 900 K.

The packing fraction is calculated assuming these liquids are hard-sphere like systems, and using the equation 2.5 with an effective hard-sphere radius [Pa88]. The number density is obtained from the formula

$$n_0 = \frac{\rho \times 6.022 \times 10^{23}}{M} \text{ (atoms/cm}^3\text{)} \tag{6.3}$$

where $n_0$ is the number density in unit volume, $\rho$ is the density and $M$ is the average atomic mass. The calculated packing fraction for pure Ni and the alloys near to their liquidus temperatures are tabulated in table 6.1.

| *Sample* | *Density* (g $cm^{-3}$) | *Packing fraction* | $T_{liq}$ (K) |
|---|---|---|---|
| Pure Ni | 7.82 ± 0.04 | 0.51 (1745 K) | 1726 |
| $Ni_{80}P_{20}$ | 7.92 ± 0.05 | 0.50 (1200 K) | 1173 |
| $Pd_{40}Ni_{40}P_{20}$ | 8.96 ± 0.03 | 0.51 (1000 K) | 974 |
| $Pd_{43}Ni_{10}Cu_{27}P_{20}$ | 9.03 ± 0.03 | 0.51 ( 900 K) | 859 |

Table 6.1: The packing fraction of the alloy liquids just above the liquidus temperatures calculated from the density data by equation 2.5.

### 6.2.2 Viscosity

In liquid Ni the reported viscosity measurements by Y. Sato *et. al.* [Sa02] in the temperature range 1740 K - 1880 K is found to be obeyed Arrhenius type behavior and its value at 1795 K is 1.89±0.28 mPa s. The viscosity measurements on liquid $Ni_{80}P_{20}$ [Ni85] reported the value of 8.55±0.52 mPa s at 1390 K. Several authors reported viscosity measurements on $Pd_{40}Ni_{40}P_{20}$ from its undercooled state to well above its liquidus temperatures [Gr04, Ts91, Wi98]. Recently Griesche *et. al.* reported viscosity measurements in the temperature range 880 K to 1137 K and the values vary from 68.9±22.7 to 11.1±2.9 mPa s. By replacing 20% Ni by Cu in $Pd_{40}Ni_{40}P_{20}$ the viscosity is found to be decreased, ($Pd_{43}Ni_{10}Cu_{27}P_{20}$) [Gr04] and its value ranges from 48.0±14.0 to 5.9±1.9 mPa s in the temperature range 897 K to 1208 K. Unlike pure Ni these glass forming alloys show large increase in viscosity on cooling towards their melting temperatures. The reported viscosity values in these liquids are tabulated in table 6.2.

| *Alloy* | *Viscosity* (mPa s) | *T* (K) |
|---|---|---|
| Pure Ni | 1.89±0.28 | 1795 |
| $Ni_{80}P_{20}$ | 8.55±0.52 | 1390 |
| $Pd_{40}Ni_{40}P_{20}$ | 68.9±22.7 - 11.1±2.9 | 880 - 1137 |
| $Pd_{43}Ni_{10}Cu_{27}P_{20}$ | 48.0±14.0 - 5.9±1.9 | 897 - 1208 |

Table 6.2: Viscosity of the liquid alloys at some temperature of interest.

## 6.3 Thermodynamic properties

As mentioned earlier the glass transition, the crystallization, and liquidus temperatures of the metallic glass are measured using differential scanning calorimetry at a heating rate of 40 K $s^{-1}$. By adding 20 atomic percent of Phosphorus in pure

Nickel, the liquidus temperature is reduced from 1726 K to 1171 K in $Ni_{80}P_{20}$. Further adding Palladium in $Ni_{80}P_{20}$ the liquidus temperature is again decreased. A systematic change in glass transition temperature is also found while increasing the number of components. Enthalpy change in melting of these systems is found to be decreasing continuously with increasing composition [Lu99]. $Pd_{43}Ni_{10}Cu_{27}P_{20}$ alloy shows lower melting enthalpy as compared to $Pd_{40}Ni_{40}P_{20}$ [Fa04]. This decrease in enthalpy of melting can be attributed to a large negative heat of mixing of the components. The critical cooling rate for the glass formation in $Pd_{43}Ni_{10}Cu_{27}P_{20}$ is only 0.01 K $s^{-1}$, where as for $Ni_{80}P_{20}$ the critical cooling rate is more than $10^6$ K $s^{-1}$. The excess entropy at a given temperature (800 K) shows 8.4 J/mol K for $Pd_{40}Ni_{40}P_{20}$ and 9.8 J/mol K for for $Pd_{43}Ni_{10}Cu_{27}P_{20}$ and the difference increases with increasing temperature [Lu99]. Table 6.3 shows a list of thermodynamic properties of the alloys and pure Ni.

| *Alloy* | $T_g$ (K) | $T_x$ (K) | $T_{liq}$ (K) | $\Delta H_f$ (kJ/mol) |
|---|---|---|---|---|
| Pure Ni | – | – | 1726±1 | 17.2±0.51 |
| $Ni_{80}P_{20}$ | 612±0.5 | 643±0.5 | 1171±1 | — |
| $Pd_{40}Ni_{40}P_{20}$ | 577±0.5 | 669±0.5 | 974±0.5 | 10.42±0.05 |
| $Pd_{43}Ni_{10}Cu_{27}P_{20}$ | 570±0.5 | 671±0.5 | 859±0.5 | 7.01±0.04 |

Table 6.3: Thermodynamic properties of liquid Ni and the alloys obtained from DSC measurements and reported in [Lu99] .

## 6.4 Microscopic dynamics

### 6.4.1 Scattering law

As stated in section 5.1, the scattering law $S(q, \omega)$ was obtained by normalization to a Vanadium standard, correction to the self absorption, container scattering, and interpolation to a constant wave number $q$. The scattering law is shown in figure 6.1 for liquid $Ni_{80}P_{20}$ at $q = 1.0$ Å$^{-1}$. Regarding the scattering cross section of the individual elements, the alloys are predominately ($> 80\%$) coherent scatterer. However, at the first structure factor maximum at $q_0 \simeq 2.9$ Å$^{-1}$, the spectra measured at 0.4-2.0 Å$^{-1}$ are dominated by incoherent scattering. Signals from the samples, $Ni_{80}P_{20}$ and $Pd_{40}Ni_{40}P_{20}$ are dominated by incoherent scattering from Ni. Since Cu also scatters incoherently, the signals from $Pd_{43}Ni_{10}Cu_{27}P_{20}$ are dominated by Ni(73%) and Cu(20%). The alloys were measured at room temperature to obtain the instrumental energy resolution function. As seen in the figure 6.1, $S(q, \omega)$ displays a quasielastic line with an increasing width on increasing temperature. The quasielastic signals become a constant above 5 meV. The quasielastic signal is fairly separated from the vibrations.

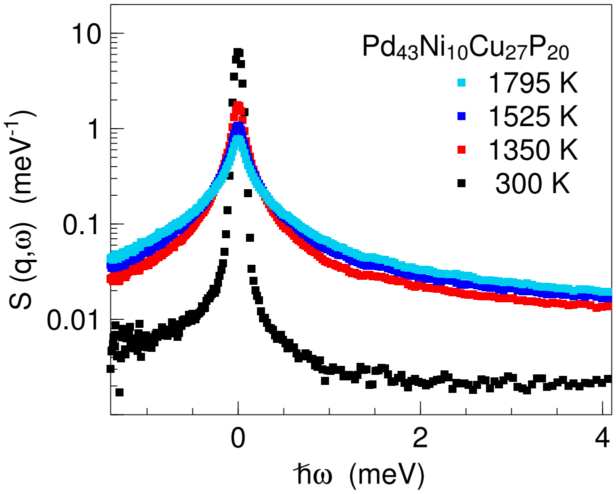

Figure 6.1: Scattering law $S(q, \omega)$ of liquid $Pd_{43}Ni_{10}Cu_{27}P_{20}$ obtained from IN6 neutron time of flight spectrometer. The data at 300 K represent the instrumental energy resolution. Measurement at higher temperatures show a broad quasielastic signal.

## 6.4.2 Phonons

The phonon contributions to dynamic processes in liquids are not well understood. It is reported that in mono atomic alkali melts the low lying collective phonon modes mediate the mass transport [Wa82, Mo87, Ba94]. The hard-sphere like colloidal suspensions that do not exhibit vibrations, the microscopic dynamics in these liquids are in good agreement with MCT predictions [Me93, Wi01]. In many molecular liquids the phonon density of state shows a first maximum between 4 and 8 meV and the broad quasielastic signal overlap with phonon contributions [Wu95, To01].

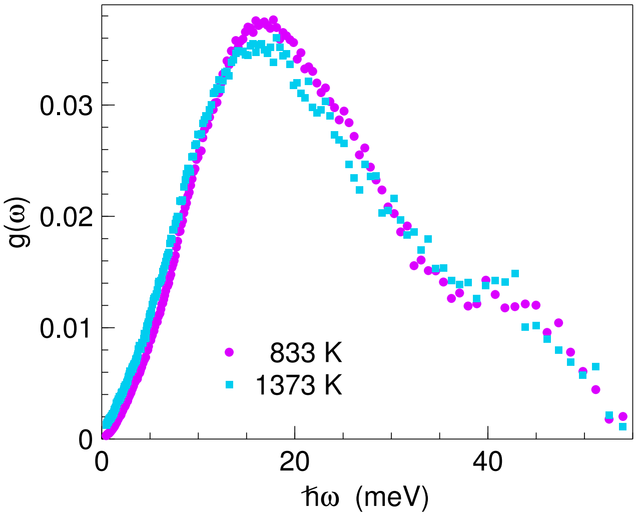

Figure 6.2: Vibrational density of states $g(\omega)$ representing mainly Ni and Cu vibrations in liquid $Pd_{43}Ni_{10}Cu_{27}P_{20}$. The maximum of $g(\omega)$ around 17 meV corresponds to 0.04 ps. The vibrations are fairly separated from relaxational dynamics above 1 ps and also exhibits a weak temperature dependence [Me02].

Figure 6.2 obtained from [Me02] displays the vibrational density of states $g(\omega)$ from the incoherent contribution from the Ni and Cu. $g(\omega)$ shows a weak temperature dependence, indicating that the vibrational degree of freedom have only few anharmonic contributions. This is also reflected in the low thermal expansivity of the melt. In our alloy melts and pure Ni, the maximum in $g(\omega)$ is around 17 meV and the vibrations are fairly separated from the quasielastic signal that extends up to several meV. This allows a detailed investigation of structural relaxation and self diffusion in these liquids.

### 6.4.3 Structural relaxation

Figure 6.3 shows the self correlation function $S(q,t)$ of liquid Ni obtained by Fourier transformation of the scattering law $S(q,\omega)$ and deconvolution with the instrumental resolution function. The structural relaxation of the incoherent Ni is observed above 1 ps, the phonon's and the fast relaxation process are observed below 1 ps. Data in $S(q,t)$ are fitted with an exponential function $S(q,t) = f_q \exp(-t/\tau_q)$. As the temperatures are high and relaxation is fast, it is difficult to observe stretching in $S(q,t)$. The final decay of correlations can be approximated to an exponential one.

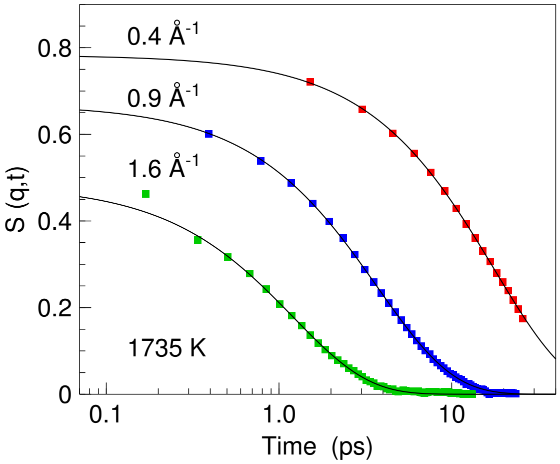

Figure 6.3: Self correlation function $S(q,t)$ of liquid Ni at different $q$ values as obtained by Fourier transform of $S(q,\omega)$ and deconvolution with instrumental energy resolution. Structural relaxation causes the finial decay of $S(q,t)$. The data are fitted with an exponential function

The normalized density correlation function $\Phi(q,t)$ of $Pd_{40}Ni_{40}P_{20}$ is shown in the figure 6.4. Between 0 and $\simeq$ 1 ps phonons and the fast relaxation process lead to a decrease in $\Phi(q,t)$ from 1 towards a plateau. Figure 6.4 display the long time decay of $\Phi(q,t)$ at $q = 0.97$ Å$^{-1}$ from this plateau towards zero in a semilogarithmic representation. The data in this figure are fitted with a stretched exponential function (Eq. 2.53). In the dense glass forming liquids the structural relaxation $\Phi(q,t)$ usually described by an stretched exponential function Eq.2.53 as a result of nonlinear coupling of the density fluctuations caused by feedback effect [Go92]. Fits with a stretched exponential function to the high-temperature data revealed a stretching exponent that approaches unity with increasing temperature.

A similar scenario is found in the case of the four component melts. A systematic change in $\beta$ with a change in alloy composition could not be detected.

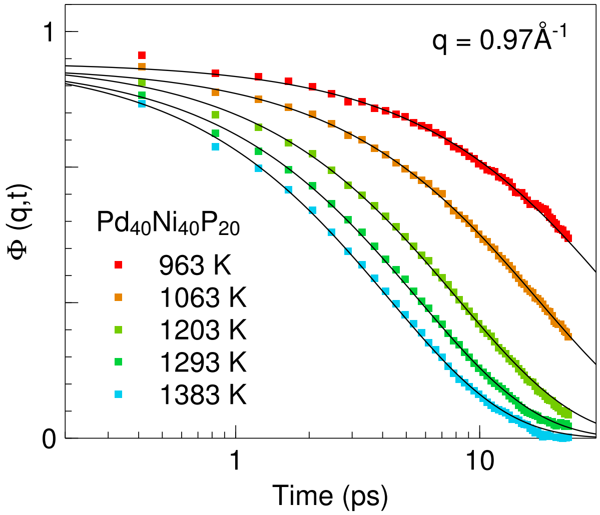

Figure 6.4: Normalized density correlation function $\Phi(q,t)$ of liquid $Pd_{40}Ni_{40}P_{20}$ at $0.97Å^{-1}$. The data points are fitted with stretched exponential function. [Eq. (2.53)].

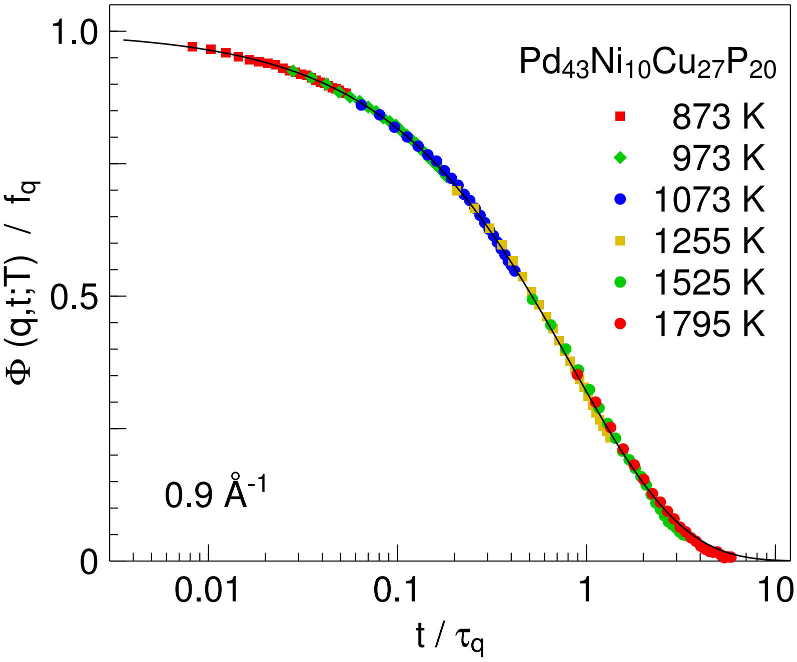

Figure 6.5: The rescaled density correlation function in the $\alpha$ relaxation regime (for $t > 1$ ps). All the data in the structural relaxation fall into a single master curve: a time temperature superposition of structural relaxation holds. The lines are fitted with a stretched exponential function [Eq 2.53] with $\beta = 0.75 \pm 0.02$.

Figure 6.5 shows the rescaled density correlation function for $Pd_{43}Ni_{10}Cu_{27}P_{20}$. The rescaling of $\Phi(q,t)$ has been done with $f_q$ the Debye-Waller-factor and that of time with $\langle\tau_q\rangle$ the mean relaxation time. Figure 6.5 demonstrates that the time-temperature superposition holds from liquid temperatures up to as high as 1795 K. The mode-coupling theory of the liquid-to-glass transition gives a consistent description of the dynamics that governs the mass transport with increasing relaxation time. With increasing relaxation time a plateau evolves in $\Phi(q,t)$. The decay from this plateau to zero exhibits stretching. The rescaled $\Phi(q,t)$ of $Pd_{43}Ni_{10}Cu_{27}P_{20}$ show a stretching with $\beta$=0.75±0.02.

### 6.4.4 Self-diffusion

Figure 6.6 shows the mean relaxation time as a function of $q$. The straight line is a power law fit $\langle\tau_q\rangle \propto q^{-n}$ with $n = 2.0$. Of course the range 0.2 to 1.4 $\text{Å}^{-1}$ is not sufficient to establish a scaling behavior in $q$. Our data is in good agreement with the relation $n = 2/\beta$ observed in a number of metallic liquids and polymers [Zo95, Co92, Co94].

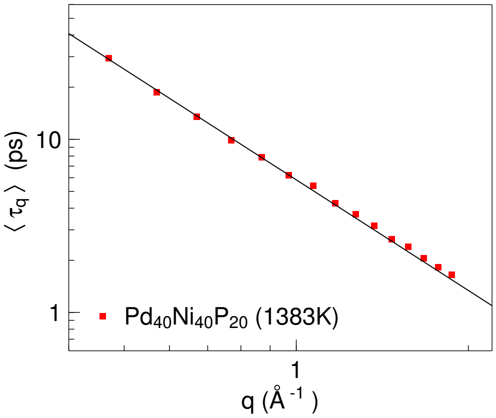

Figure 6.6: The mean relaxation time $\langle\tau_q\rangle$ is plotted against $q$. The straight line is a power law fit $\langle\tau_q\rangle \propto q^{-n}$, with $n = 2$.

The theory of molecular hydrodynamics shows that, as $q \longrightarrow 0$ the mean relaxation time is indirectly proportional to the square of the momentum transfer $q$. In the liquids Ni, $Ni_{80}P_{20}$, $Pd_{40}Ni_{40}P_{20}$ and $Pd_{43}Ni_{10}Cu_{27}P_{20}$ this dependence holds up to 1.8 $\text{Å}^{-1}$, while the first structure factor maximum is at $q_0 \simeq 2.9$ $\text{Å}^{-1}$. Figure 6.7 shows the $1/q^2$ dependence of the mean relaxation time in these liquid alloys. In liquid alkali metals, it was reported that a systematic deviation from the $q^2$ dependence of the quasielastic line width already occurs at a $q$ value that corresponds to 1/10 of their structure factor maximum. An explanation to this behavior is the low lying phonon mode that mediate atomic transport[Mo87]. A MCT calculation for hard-sphere liquids shows, in the hydrodynamic limit, that the mean relaxation time $\langle\tau_q\rangle$ is indirectly proportional to the square of the momentum transfer [Bo80]. In contrast, the mean relaxation time for the self motion in the MCT hard-sphere system varies rather well proportionally to $1/q^2$ for $q$ values extending even above the first structure factor maximum [Fu99].

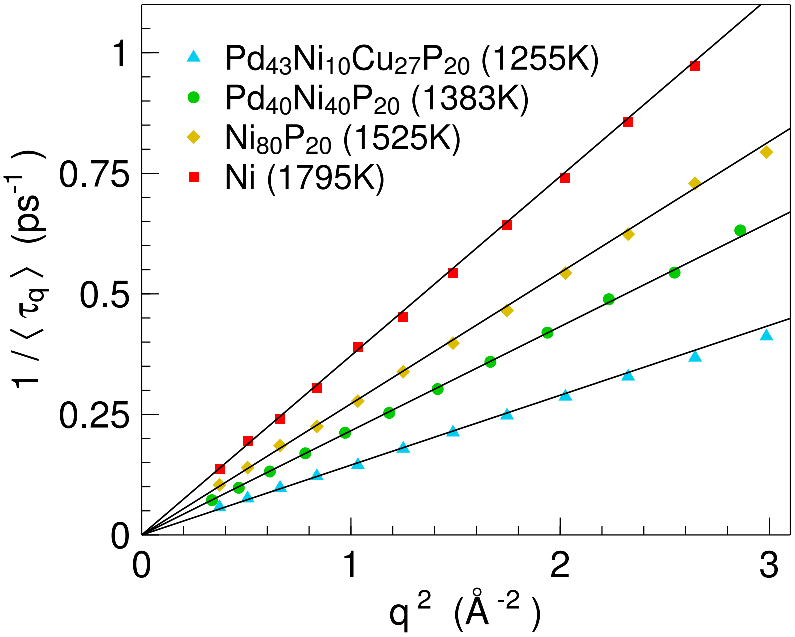

Figure 6.7: The inverse of mean relaxation time $\langle\tau\rangle$ is plotted against $q^2$. The straight line is a power law fit $1/\langle\tau_q\rangle \propto q^2$ and the slope of the line gives the self-diffusion constant $D(T)$.

It appears that the validity of $1/\langle\tau_q\rangle \propto q^2$ also for intermediate $q$ values is a specific signature of the collective atomic transport mechanism in dense liquids. We find that the mixing of hard-spheres with different radii has no effect in this behavior. Quasi-elastic neutron scattering data are not affected by convection effects, since dynamics are probed on significantly shorter time scales as the ones related to convective transport. Therefore, diffusion coefficients can be derived on an absolute scale. Since for the investigated samples the signal is dominated by the incoherent scattering from Ni, the data analysis gives the self-diffusion coefficient of Ni atoms.

The $1/q^2$ dependence of mean relaxation time, also demonstrates that the structural relaxation leads to a long range atomic transport mechanism with a diffusivity [Bo80].

$$D = \left[\langle\tau_q\rangle q^2\right]^{-1} \tag{6.4}$$

Figure 6.8 displays self-diffusion coefficients in pure Ni, $Ni_{80}P_{20}$, $Pd_{40}Ni_{40}P_{20}$, and $Pd_{43}Ni_{10}Cu_{27}P_{20}$ as a function of $1/T$ . For a comparison, data of $Pd_{40}Ni_{10}Cu_{30}P_{20}$ and of $Pd_{43}Ni_{10}Cu_{27}P_{20}$ measured at lower temperatures are shown as well. The values in the case of $Pd_{43}Ni_{10}Cu_{27}P_{20}$ range from $3\pm1\times10^{-11}$m$^2$s$^{-1}$ at 833 K to $4.74\pm0.18\times10^{-9}$m$^2$s$^{-1}$ at 1795 K. At the liquidus temperatures the diffusion slower by 2 orders of magnitude in most simple metallic liquids and alloys. Diffusivities obtained from the recent $^{57}$Co and $^{30}$P tracer diffusion measurements in liquid

$Pd_{43}Ni_{10}Cu_{27}P_{20}$ are in excellent agreement with the diffusivities obtained from the present inelastic neutron scattering. Unlike in Zr based glass forming melts, where the diffusivities of various tracers exhibit a size dependence (smaller atoms diffuse faster with smaller activation enthalpy) the similar diffusivities in $Pd_{43}Ni_{10}Cu_{27}P_{20}$ indicate a collective self motion of elementary atoms or ions.

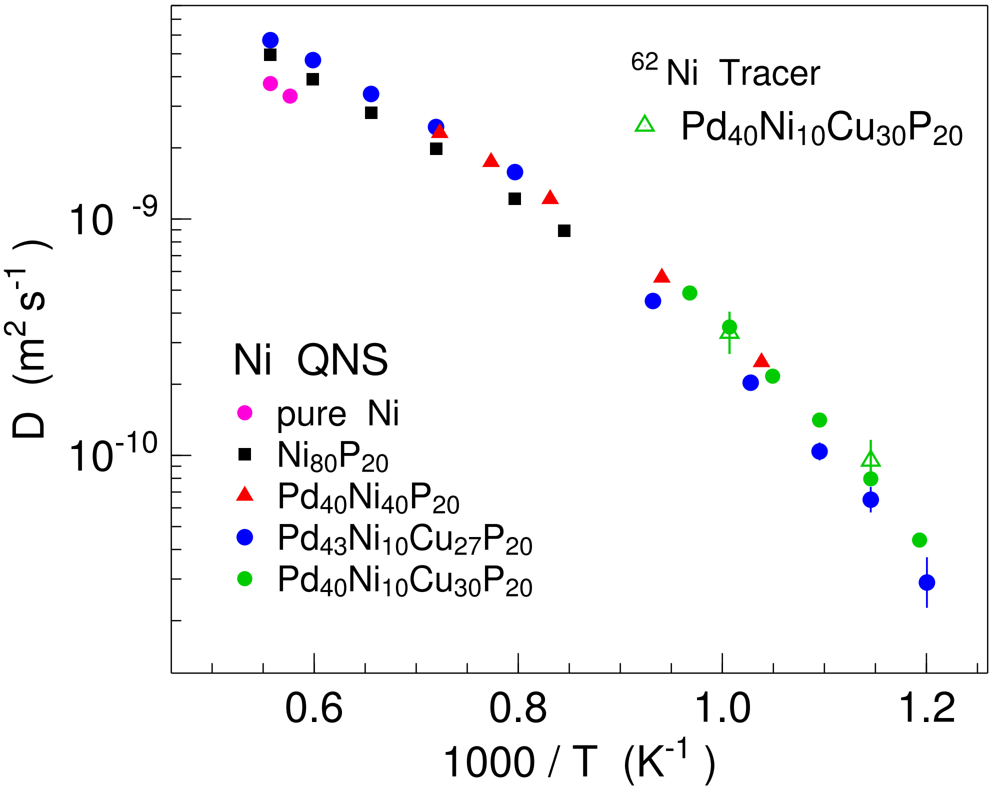

Figure 6.8: Ni self-diffusivity in the liquids Ni, $Ni_{80}P_{20}$, $Pd_{40}Ni_{40}P_{20}$ and $Pd_{43}Ni_{10}Cu_{27}P_{20}$ in a semilogarithmic plot, over 1000 degrees. Irrespective of the liquid composition and thermodynamic properties, the Ni self-diffusivites are similar within 20% .

In simple liquids, the shear viscosity $\eta$ and the self-diffusivity $D$ generally obey the Stokes-Einstein relation [Ba94, Ty84, Kr87] eq. 2.17. where $a$ is the hydrodynamic radius of the diffusing species. This equation even holds in most of the molecular liquids [Ch97]. If we take $a$ is equal to 1.15 Å for Ni, it's covalent radius [Pa88], it was reported that the relation 2.17 is valid for the four component melts but the three component melts show 20% lower values [Gr04]. The failure of Stokes-Einstein relation is also reported in the same system from a Au tracer diffusion measurement [Du93]. The Stokes-Einstein relation does not obey in $Ni_{80}P_{20}$ and the calculated diffusivity from the viscosity data [Yo85] is 40% lower as compared to the experimentally observed one. Pure Ni shows a similar discrepancy, but with the calculated diffusivity showing 40% higher $D$ value than the experimently observed one. Table 6.4 compares the diffusivities obtained from neutron scattering and those calculated from the viscosity via Stokes-Einstein relation.

| *Alloy* | *From QNS* $D$ ($\times 10^{-9}$m$^2$s$^{-1}$) | *From Viscosity* $D$ ($\times 10^{-9}$m$^2$s$^{-1}$) | *Temperature* (K) |
|---|---|---|---|
| Ni | 3.80±0.06 | 6.03±0.11 | 1795 |
| $Ni_{80}P_{20}$ | 1.96±0.06 | 1.04±0.11 | 1390 |
| $Pd_{40}Ni_{40}P_{20}$ | 0.55±0.06 | 0.44±0.66 | 1063 |
| $Pd_{43}Ni_{10}Cu_{27}P_{20}$ | 1.41±0.06 | 1.48±0.56 | 1255 |

Table 6.4: Ni self-diffusivities obtained from the inelastic neutron scattering and those calculated from the viscosity data via Stokes-Einstein relation.

## 6.5 Atomic transport mechanism

Among the three alloys investigated the $Pd_{43}Ni_{10}Cu_{27}P_{20}$ melt has the highest glass forming ability. A cooling rate of only 0.01 K $s^{-1}$ is sufficient to avoid crystallization and the formation of glass. Therefore it is possible to measure self-diffusion constant from the liquid down to the calorimetric glass transition temperature. Figure 6.9 shows the diffusivities in liquid Ni, $Ni_{80}P_{20}$, $Pd_{40}Ni_{40}P_{20}$ and $Pd_{43}Ni_{10}Cu_{27}P_{20}$ from tracer diffusion measurements, calculated from the viscosity via the Stokes-Einstein relation (Eq. 2.17) and the inelastic neutron scattering.

At temperature around 1390 K, the Ni self-diffusivities ($D$) show values $1.96\pm0.06 \times 10^{-9}$m$^2$s$^{-1}$ in $Ni_{80}P_{20}$, $2.23\pm0.11\times 10^{-9}$m$^2$s$^{-1}$ in $Pd_{40}Ni_{40}P_{20}$ and $2.09\pm0.11 \times 10^{-9}$m$^2$s$^{-1}$ in $Pd_{43}Ni_{10}Cu_{27}P_{20}$ . This shows similar Ni self-diffusivities (within 10%) even though the composition and hence the thermodynamic properties are different in these systems ( e.g enthalpy changes in melting differ over 35% as compared in $Pd_{40}Ni_{40}P_{20}$ to $Pd_{43}Ni_{10}Cu_{27}P_{20}$). At temperatures around 1000 K, the data for $Pd_{40}Ni_{40}P_{20}$ and $Pd_{43}Ni_{10}Cu_{27}P_{20}$ overlap. The differences in the diffusion constants of these two alloys are not larger than the error bars. This value of diffusivity is similar to that found one in mono-atomic liquid metals at their respective melting temperatures. For example, close to the melting point $D = 4.2 \times 10^{-9}$m$^2$s$^{-1}$ in liquid sodium [Mo86] from INS, $D = 3.7 \times 10^{-9}$m$^2$s$^{-1}$ in Potassium [Sh74] from tracer diffusion measurements and $D = 2.0 \times 10^{-9}$m$^2$s$^{-1}$ in liquid Tin from tracer diffusion under microgravity conditions [Fr87].[1].

---

[1] Ni self-diffisivities in the liquids : Ni, $Ni_{80}P_{20}$ , $Pd_{40}Ni_{40}P_{20}$ and $Pd_{43}Ni_{10}Cu_{27}P_{20}$ are listed in appendix C

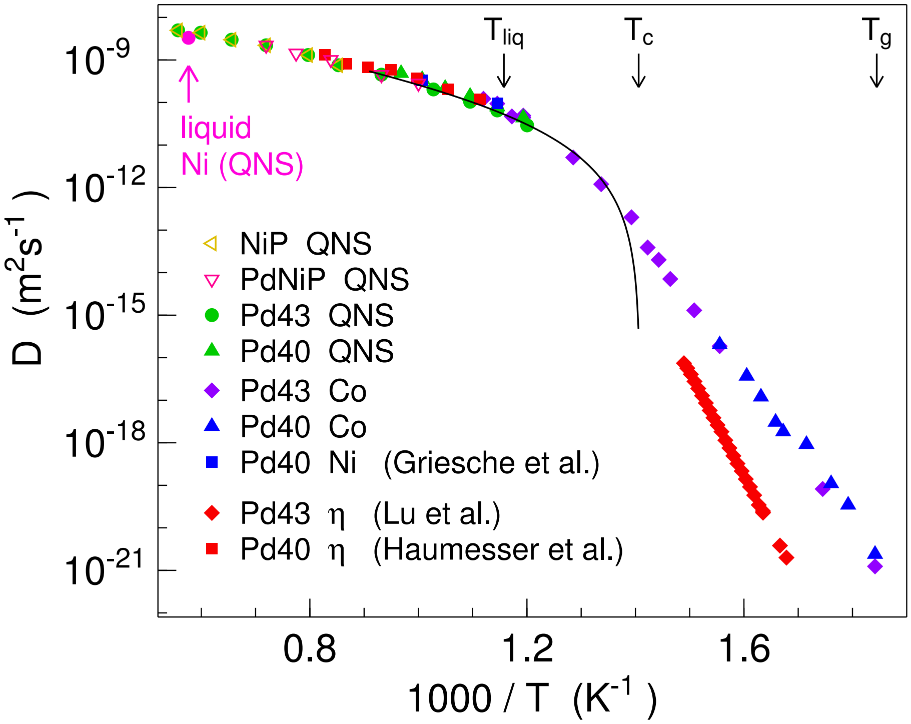

Figure 6.9: Atomic transport in Ni, NiP, PdNiP and PdNiCuP melts: At high temperatures diffusivities are similar to the diffusivities in liquid Sn and Na close to their melting temperature $T_m$ [Me02, Zo03].

Isotopic effect $E = (D_a/D_b - 1)/(\sqrt{m_b/m_a} - 1)$ (subscripts $a$ and $b$ represents two isotope of mass $m_a$ and $m_b$ with respective self-diffusivities $D_a$, $D_b$.) is a measure of degree of collectivity of the atomic transport. For diffusion via jump process in solid state lattice and via binary collision precess in simple liquid one finds the value of $E$ is close to unity [Me90]. In liquid Sn an isotopic effect of 0.4 has been reported, that increases with increasing temperature [Fr87]. Molecular dynamics simulation on Lennard-Jones liquids indicates that in order to have a change of $E$ from 0 to 0.3 one needs a change in density over 20% [Sc01]. Measurement of isotopic effect in $Pd_{43}Ni_{10}Cu_{27}P_{20}$ (Ref [Zo03]) yields $E \simeq 0$ at its liquidus temperature.

The atomic transport mechanism in these alloy melts remain collective at their liquidus temperatures even though the diffusivities are comparable to that in simple metallic liquid. The liquids exhibit low thermal expansion. The liquid $Pd_{43}Ni_{10}Cu_{27}P_{20}$ exhibits thermal expansion coefficient of $4\times10^{-5}$ $K^{-1}$ between 833 and 1373, and therefore the density and packing fraction changes only about 2%. In liquid $Pd_{40}Ni_{40}P_{20}$, the thermal expansivity is in the order of $7.8\times10^{-6}$ $K^{-1}$ and density changes only by 1.7% within 950 - 1200 K [Ch93]. Therefore, in these liquids to a good approximation, one can assume that the hard-sphere radius is temperature independent. The dense packing resulting a collective transport mechanism that extends well above their liquidus temperature, where the diffusivities are comparable to that in the simple metallic liquids.

In the simple metallic liquid, like liquid Na, the microscopic transport mechanism is strongly influenced by packing fraction. The density of liquid Na at 1773 K is 0.58 g $\mathrm{cm}^{-3}$, hence the packing fraction is only 0.23. In this regime the particle dynamics is controlled by binary collision and well accordance with simple hard-sphere theoretical predictions. At moderate density the Na self-diffusion couple to the transverse mode hence exhibit an increase in diffusion coefficient. In the high density liquid Na, *i.e.* at low temperature (371 K), just above the liquidus temperature, where the density is 0.98 g $\mathrm{cm}^{-3}$ and the packing fraction is 0.39. The dynamics is in accordance with MCT that the particle oscillate in a cage of next nearest neighbors and diffusive motion occurs through the coupling to a longitudinal mode which transport the particle together with its neighborhood from one place to other [Pi03].

The liquids we investigated show the density and the packing fraction is much higher as compared to the density of Na at its liquidus temperature. The investigation on self-diffusion in the liquids: Ni, $\mathrm{Ni}_{80}\mathrm{P}_{20}$, $\mathrm{Pd}_{40}\mathrm{Ni}_{40}\mathrm{P}_{20}$ and $\mathrm{Pd}_{43}\mathrm{Ni}_{10}\mathrm{Cu}_{27}\mathrm{P}_{20}$ exhibit similar microscopic transport process as in the case of dense liquid Na. The mixing of different atoms change drastically the thermodynamic properties and glass forming ability of the liquids but the self-diffusion at a given temperature is within error bars and similar to that one found in liquid Na at 371 K ($D_{Na} = 4.23\times10^{-9}\mathrm{m}^2\mathrm{s}^{-1}$). This indicates that at high densities or at high packing fractions the self-diffusion become highly collective. In the collective particle motion the influence of thermodynamics parameter like excess entropy is negligible but the mass transport is dominated by the packing fraction.

## 6.6 Entropy and self-diffusion

There is no general understanding how the thermodynamic properties correlate with self-diffusion in liquid metals and alloys. In simple liquid metals or in alkali melts the thermodynamic influence on self-diffusion is still an on going debate [Al04]. Some theories [Ro77] and molecular dynamic simulation studies which shows that the excess entropy or configuration entropy is correlated to self-diffusion in hard-sphere like liquids and predicted a universal scaling law [Dz96]. The excess entropy is defined through the radial distribution function(RDF) by

$$S_2 = -2\pi\rho\int_0^\infty g(r)\{\mathrm{In}[g(r)] - [g(r)-1]\}r^2dr \qquad (6.5)$$

The diffusion coefficient $D$ is expressed in dimensionless form $D^* = D\Gamma^{-1}\sigma^{-2}$, where $\sigma$ is the hard-sphere diameter and $\Gamma$ is the collision frequency according to the well-known Enskog theory of atomic transport [Ch39].

$$\Gamma = 4\,\sigma^2\, g(\sigma)\, \rho \sqrt{\frac{\pi k_B T}{m}} \tag{6.6}$$

Here $g(\sigma)$ is the radial distribution function evaluated at the hard sphere diameter [in practice $\sigma$ may be interpreted as the position of the first peak in the $g(r)$ ], $m$ is the mass of the diffusing species, $\rho$ is the number density, and $k_B\,T$ has the usual meaning of Boltzmann constant times temperature.

The original work of Dzugutov [Dz96] was based on simulation results, and has been further extended to the case of fluid mixtures by Hoyt *et. al.* [Hy00]. He provided a prescription for predicting only a single diffusivity parameter defined as a particular combination of the component diffusivities but did not prescribe any scaling law for the individual diffusivities of the components.

Our results strongly suggest dying out of the hard-sphere collisions governing microscopic transport but a collective atomic transport in dense liquids. But these theories [Dz96, Hy00] are mostly based on hard-sphere collision dynamics. In turn, the particle collisions are invariably related to thermodynamics state of the systems. Even though, a detailed comparison is not made, a large difference in thermodynamic properties, particularly the excess entropy [Lu02] in our system and a similar Ni self-diffusivities indicates that the validity of these theories in dense metallic liquids are doubtful. Thus our results confirm, the thermodynamic influence on self-diffusion becomes less important as the packing fraction increases. The packing fraction is the dominant factor governing the mass transport process in dense hard-sphere like liquids.

# Chapter 7

# Dynamics in liquids with CSRO

*Summary : The results of the investigation of the microscopic structure and dynamics in Al-Ni molten alloys are presented in this chapter.*

## 7.1 Chemical short range order (CSRO)

In general, metallic liquids consist of metallic ions embedded in a uniform free electron gas. With a short range repulsive force and an inner positive core the liquid metals are considered as a collection of hard-spheres. But inter-metallic compounds formed by transition metals (TM) and polyvalent main group elements such as Al or Si, hybridization leads to the formation of a deep pseudo-gap close to the Fermi level. It prevents the formation of TM-TM nearest neighbors and causes a chemical short-range order in the system [Ma86].

The CSRO causes anomalies in physical properties. For example, the enthalpy of mixing in the liquid phase are very often large and negative [Gr98, Su90, St93, Sa71], chemical activities [Va65, Jo80, Hi90], atomic volumes [Ay69], entropies [Ba83] and viscosities [Pe71] are characteristic of a highly non-ideal solution. It is not yet understood how CSRO influences the microscopic mass transport in these liquid alloys. To give an insight to this problem, we have investigated the interplay of the compositional dependence of the CSRO and the Ni self-diffusion in Al-Ni melts.

## 7.2 Al-Ni phase diagram

Figure 7.1 shows the Al-Ni phase diagram. The blue spheres depicted in it indicate the compositions and temperatures chosen for investigating the microscopic dynamics. On solidifying the Al-Ni alloy melts crystallizes. The formation crystal structure depends on the composition. Up to 50 atomic %, the alloy crystallizes as $Al_3Ni$ and it has an orthorhombic structure, is the prototype of the $D0_{20}$ type.

About 75 atomic percent of Al, the alloy crystallizes in $Ni_3Al$ structure. $Ni_3Al$ has a F.C.C structure of the $L1_2$ type. It will be interesting to study how the microscopic dynamics differ with different crystal structure formation. The phase diagram shows that the melting temperature of Al-Ni alloy increases rapidly with increasing Ni content on the Al rich side. At equal composition of Al and Ni, it has got the maximum melting temperature of 1911 K (1638 $^0$C). Further increase of the Ni content reduces the melting temperature only up to 1665 K.

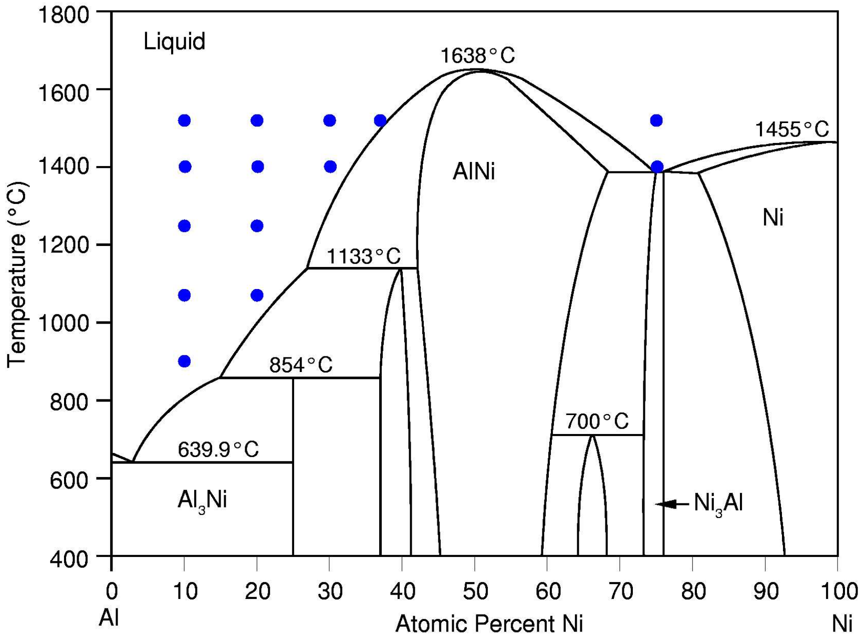

Figure 7.1: Al-Ni phase digram: The blue marks indicate the composition and temperature chosen for investigating the microscopic dynamics.

## 7.3 Density and viscosity of Al-Ni melts

Ayushina *et.al.* [Ay69] were the first to investigate the density of Al-Ni melts. They studied the density of Al-Ni as a function of composition and temperature. The measured density shows a linear increase with Ni concentration. From the phase digram it is clear that the Al-Ni melting temperature increases with Ni content up to 50 atomic percent and then decreases. However, this behavior is not reflected in the density data. The calculated molar volume from the measured density shows a non linear variation with composition. This indicates a nonlinear variation in the packing density with composition. The density and calculated molar volume are shown in the figure 7.2 at a temperature 1795 K. Because of CSRO present in the Al-Ni melts, it cannot be approximated to a hard-sphere like system, but the calculated molar volume indicates that the packing fraction in this system changes with compositions.

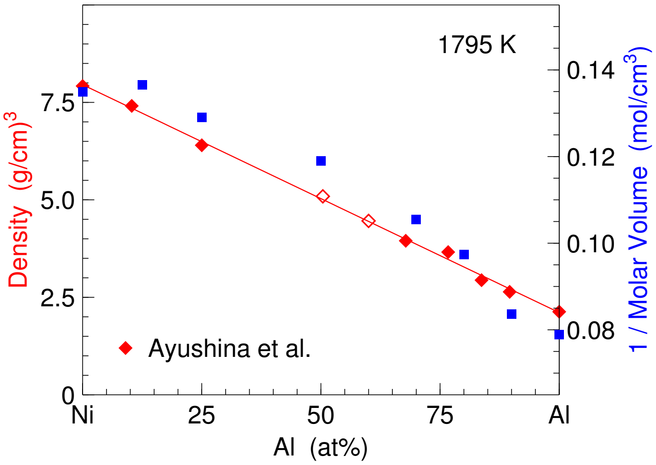

Figure 7.2: The red diamonds indicate the density [Ay69] and the blue squares, the molar volume calculated from the density data of Al-Ni melts at 1795 K, respectively. The open diamond represent the sample is in the crystalline state.

Figure 7.3 shows the viscosity of Al-Ni melts as a function of Ni concentration at 1990 K. The Al-Ni melts show the largest viscosity and the highest melting temperature at equal atomic percent. This sharp increase might be due to the strong CSRO present in the system. Such results were also seen in liquids Mg-Pb [Ge55a] and Mg-Sn [Ge55b] at particular stoichiometric compositions. These two liquids also possess CSRO and show the highest melting temperature and highest viscosity at compositions $Mg_2Pd$ and $Mg_2Sn$.

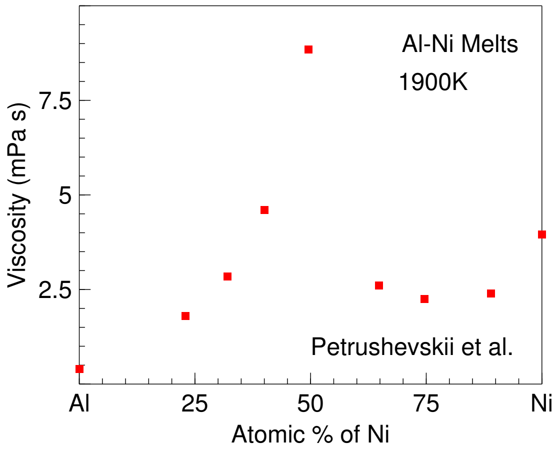

Figure 7.3: The viscosity of Al-Ni melts as function of Ni content as reported by Petrushevskii *et. al.* [Pe71].

## 7.4 Structure of Al-Ni melts

The structure of $Al_{80}Ni_{20}$ was experimentally investigated by Maret *et. al.* [Ma90], who used isotopic substitution and neutron diffraction experiments to measure each of the three independent partial structure factors at 1300 K. Figure 7.4 (a) shows the structure factors of $Al_{80}Ni_{20}$ observed by Maret *et. al.*.

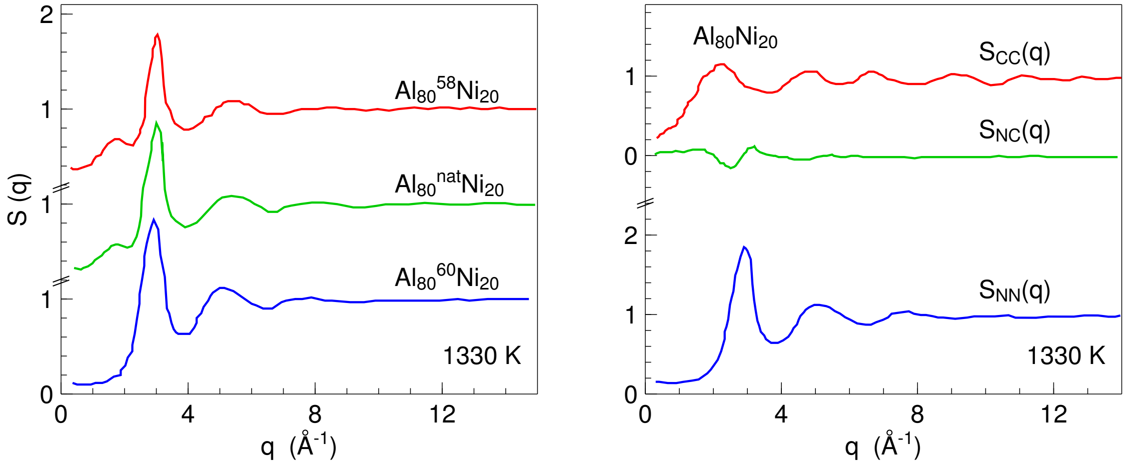

Figure 7.4: (a) The structure factors of $Al_{80}Ni_{20}$ observed by Maret *et. al.* in the neutron diffraction experiments. (b) The Bhatia-Thornton (BT) partial structure factors for liquid $Al_{80}Ni_{20}$ [Ma90].

The observed structure factor showed a peak at a $q$ value smaller than the first structure factor maximum. This peak represents the so called *prepeak*. The origin of the prepeak can be seen clearly from BT correlation function plotted in figure 7.4 (b). $S_{CC}$ shows a peak in the same position as the prepeak. The main peak at 3.0 Å$^{-1}$ corresponds to the next nearest neighbor distance. The prepeak indicates a chemical ordering beyond the first nearest neighbors. The obtained Ni-Ni and Ni-Al partial structure factors showed a significant prepeak and preminimum, respectively. The origin of this is attributed to a strong inter atomic interaction between Ni and Al, as discussed in detail by Saadeddine *et. al.* [Sa94], Phuong *et. al.* [Ph93] and Mark Asta *et. al.* [As99]. More specifically, the CSRO is affected by the strength of the Ni-Al interaction relative to the pure Ni-Ni and Al-Al interactions. Time of flight experiments on $Al_{80}Ni_{20}$ melts also show a peak (corresponding to the prepeak) in the quasielastic structure factor. To know the influence of composition on the formation of CSRO in Al-Ni melts, we have investigated CSRO as a function of Ni concentration and temperature.

## 7.5 Composition dependence of CSRO

To study the composition dependence of the CSRO, we have investigated the alloy melts $Al_{100-x}Ni_x$ at 1525 K and at 1795 K for compositions $x$ = 10, 20, 23, 30, 38 and 75. For the intermediate compositions, 39 to 74 atomic percent of Ni, we were not able to perform the experiments because the melting temperatures were too high for the ILL furnace.

The scattering law is then integrated over its elastic peak to obtain information on the structure factor at intermediate length scales [see section 5.3]. The structure factor maxima in these melts are at $q_0 \simeq 2.7$ - 3.0 $\text{Å}^{-1}$. The systems scatter incoherently, since the $q$ range for the experiment is well below $q_0$, the structure factor maximum. In principle no coherent scattering from the sample can be observed.

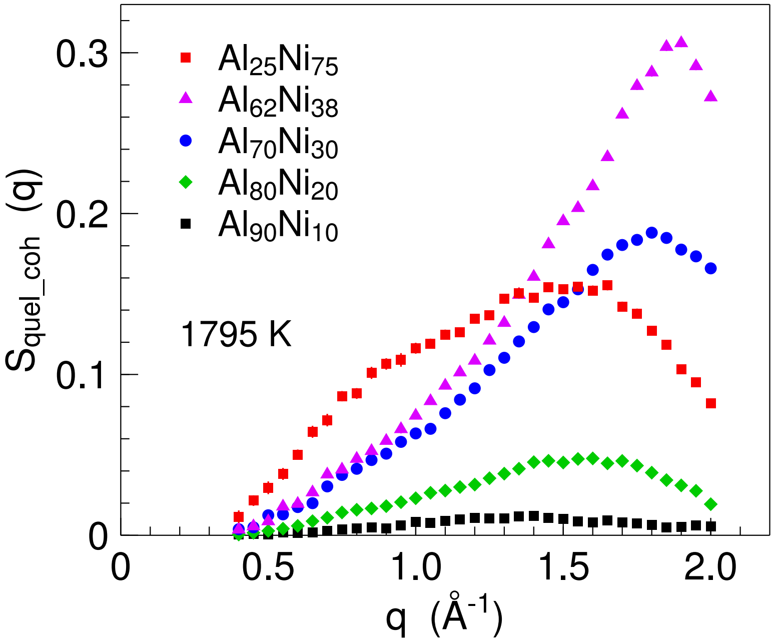

Figure 7.5: $S_{quel\_coh}$ quasielastic structure factor obtained from time of flight neutron scattering. The prepeak shows increasing intensity with increasing Ni content.

The figure 7.5 displays the quasielastic structure factor $S_{quel\_coh}$ for Al-Ni melts at 1795 K. For clarity, a constant that approximates the incoherent scattering from Ni has been subtracted. This quasielastic structure factor shows the prepeak and that originate from the coherent scattering due to CSRO.

For Al rich alloys the spectra exhibit prepeaks that show an increasing intensity with increasing Ni content at 1795 K. In the $Al_{80}Ni_{20}$ melt the prepeak shows a maximum at $\simeq 1.6\text{Å}^{-1}$, whereas in $Al_{68}Ni_{38}$ the maximum is shifted towards a higher $q$ value, $1.8\text{Å}^{-1}$. In the $Al_{90}Ni_{10}$ melt nearly no prepeak is visible at the same temperature. The quasielastic structure factors measured at 1525 K show similar prepeak positions as compared to the data at 1795 K, and the intensity in the maxima exhibit a $\simeq$ 20% increase which can be accounted for the increased Debye-Waller factor. On the Ni rich side ($Al_{25}Ni_{75}$) $S_{quel\_coh}$ also exhibits a broader prepeak. The maximum of the broader prepeak is located around 1.5$\text{Å}^{-1}$. The shift of the prepeak position indicates that the ordering beyond the nearest neighbours changes with composition.

The total structure factor of a binary alloy consists of three partial structure factors. In order to understand the complete structural information and CSRO that is present in the Al-Ni melts one has to consider the three partial structure factors. To obtain partial structure factors from neutron scattering experiment, one needs to use different isotopes. As the isotopes are expensive and limited neutron beam time we used the molecular dynamics simulation results obtained by S. K. Das and J. Horbach [Da04] to explain the structure of Al-Ni melts.

The molecular dynamic simulation was done using the potential of embedded-atom type derived by Mishin *et. al.* [Mi02]. The simulations were done at 1795 K and 1525 K for different Al-Ni compositions. The system consists of 1500 particles in each case. First they did standard Monte-Carlo simulation in the $NpT$ [Bi00] ensemble to fully equilibrate the system at zero pressure and to generate five independent configurations for the MD simulation in the micro-canonical ensemble. Newton's equations of motion were then integrated with the velocity Verlet algorithm using a time step of 1.0 fs. From the MD trajectories the structure factor and the diffusion constant were determined. The temperature and concentration dependence of the measured diffusion coefficients are well reproduced by the MD simulation. There is an overall 80% agreement with the experimental data. The simulation results are found to be appropriate to describe the dynamics in Al-Ni melts, since the inter atomic potential used for the simulation seems to be quite accurate [Mi02].

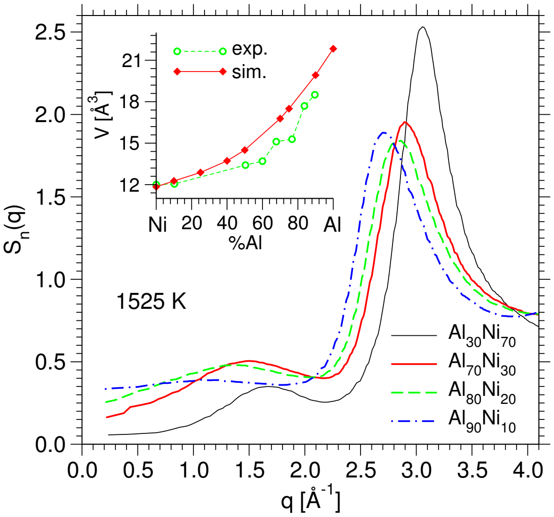

Figure 7.6: Structure factor $S_n(q)$ of Al-Ni melts as calculated from the partial structure factors of the simulation weighted with neutron scattering lengths. Inset: Atomic volume from the simulation compared to the experimental data as a function of composition [Da04].

To obtain the structure factor $S_n(q)$ of Al-Ni melts from the simulation, the partial structure factors were weighted with the neutron scattering lengths of Al and Ni. The structure factor is defined by:

$$S_n = 1/(N_{Al} b_{Al}^2 + N_{Ni} b_{Al}^2) \sum_{k,l}^{N} b_k b_l \langle e^{iq\cdot(r_k - r_l)} \rangle \tag{7.1}$$

were $r_k$ is the position of $k^{th}$ particle, $N$ denotes the number of atoms, and $b_{Al} = 0.3449 \times 10^{-12}$ cm and $b_{Ni} = 1.03 \times 10^{-12}$ cm are the neutron scattering lengths of Al and Ni, respectively. Figure 7.6 shows the structure factor obtained from the simulation. A prepeak is also observed in the simulation which is located at slightly smaller $q$ values as compared to the experimental results for the Al rich system. However, in the Al rich system, a similar behavior as in the experiment is found, i.e. with increasing Ni content the prepeak become narrower its amplitude increases, and its location shifts to a higher $q$ value.

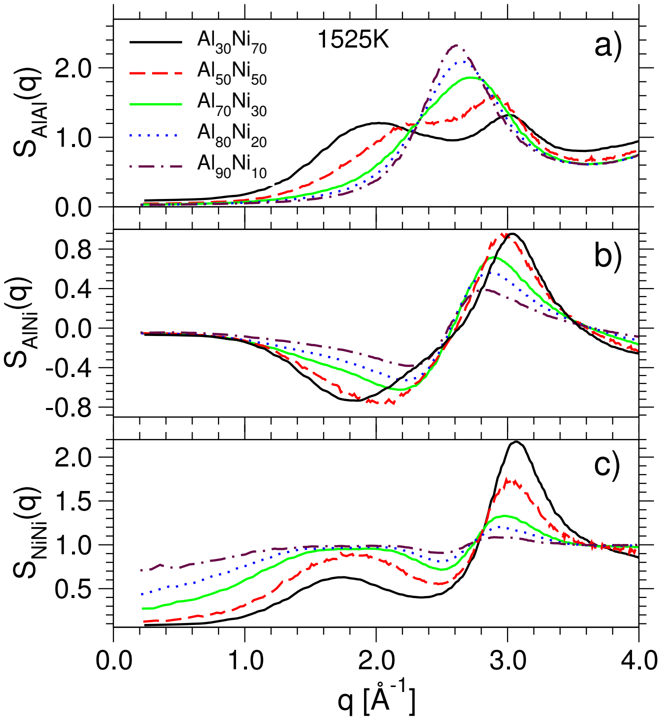

Figure 7.7: Partial structure factors (a) $S_{AlAl}(q)$, (b) $S_{AlNi}(q)$ (c)$S_{NiNi}(q)$ of Al-Ni melts obtained from the simulation at 1525 K [Da04].

The figure 7.7 shows the partial structure factors obtained from the simulation. The simulation results show that no prepeak emerges from the $S_{AlAl}(q)$ for Al rich compositions but the main peak moves to slightly higher $q$ with decreasing Al concentration. By further reduction of the Al concentration, a prepeak evolves that move to smaller $q$. As a result a double peak structure is observed in $S_{AlAl}(q)$ for $Al_{70}Ni_{30}$ with maxima at $q_1 = 1.8\text{Å}^{-1}$ and $q_2 = 3.0\text{Å}^{-1}$. In $S_{AlNi}(q)$, a prepeak with negative amplitude is visible at all Al concentration and, as in the Al-Al correlations, this peak moves to smaller $q$ with decreasing Al concentration. The negative amplitude of the prepeak in $S_{AlNi}(q)$ is due to the avoidance of the corresponding Al-Ni distance. Also in $S_{NiNi}(q)$ a prepeak is present at all Al concentrations. This prepeak broadens with increasing Al concentration while its location remains essentially the same. In $Al_{70}Ni_{30}$, the main peak is at the same location for all the three different partial structure factors, namely around $q_0 = 3.0\text{Å}^{-1}$.

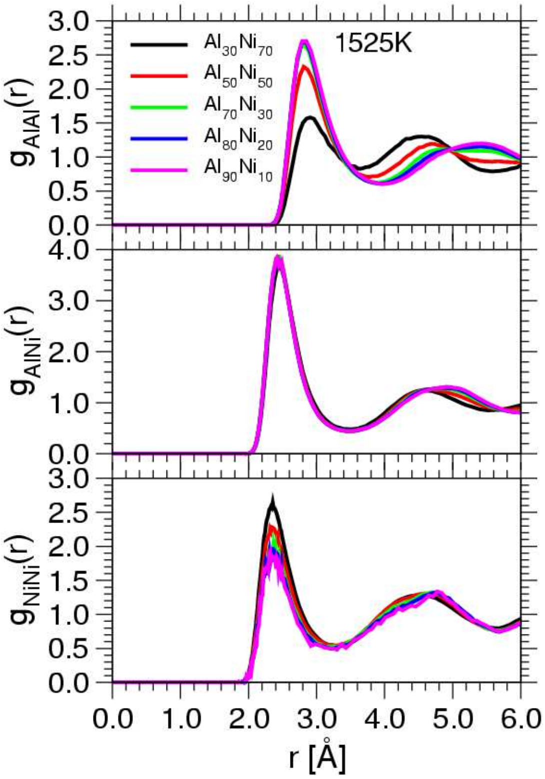

Figure 7.8: Pair correlation function $g_{\alpha\beta}(r)$ of Al-Ni melts as obtained from the simulation.

The structure factor obtained from the simulation of Das and Horbach [Da04] give the following: In Ni rich system, the distance between Al-Al atoms is similar to that of Ni-Ni atoms. On the other hand in Al rich system the distance between Al-Al atoms becomes larger without a significant change in the distance between Ni-Ni atoms. The location of this peak moves towards a higher $q$ in the Ni rich system due to the fact that with increasing Ni concentration the packing density of atoms increases. The atomic volume $V_a$ found in the simulation is comparable to the experiment [Ay69]. All this explain the nonlinear behavior of atomic packing upon change in the composition.

## 7.6 Microscopic dynamics

Similar to the case of the dense metallic liquids investigated in the first part, the phonon contributions are found to be well separated from the quasielastic signals in Al-Ni melts. This allows us to derive an accurate Ni self-diffusion coefficient from the experiment. The scatting law is obtained as described in section 5.2. The scattering law is then Fourier transformed and division of the instrumental resolution function to obtain the normalized density correlation function $\Phi(q,t)$. The $\Phi(q,t)$ decays to zero exponentially in all Al-Ni melts.

## 7.7 Atomic transport

The Ni self diffusivities are derived from the $q^2$ dependence of the mean relaxation time as described earlier. Figure 7.9 shows the $1/q^2$ dependence of mean relaxation time $\langle\tau_q\rangle$. Unlike in dense liquids, where the $1/q^2$ dependence of $\langle\tau_q\rangle$ holds at intermediate $q$ values but in Al-Ni melts it deviates at low $q$. In $Al_{90}Ni_{10}$ melt the $1/q^2$ dependence holds up to $0.6Å^{-1}$. The deviation from the $q^2$ dependence is found to be independent of compositions, but holds at larger $q$ values in $Ni_3Al$.

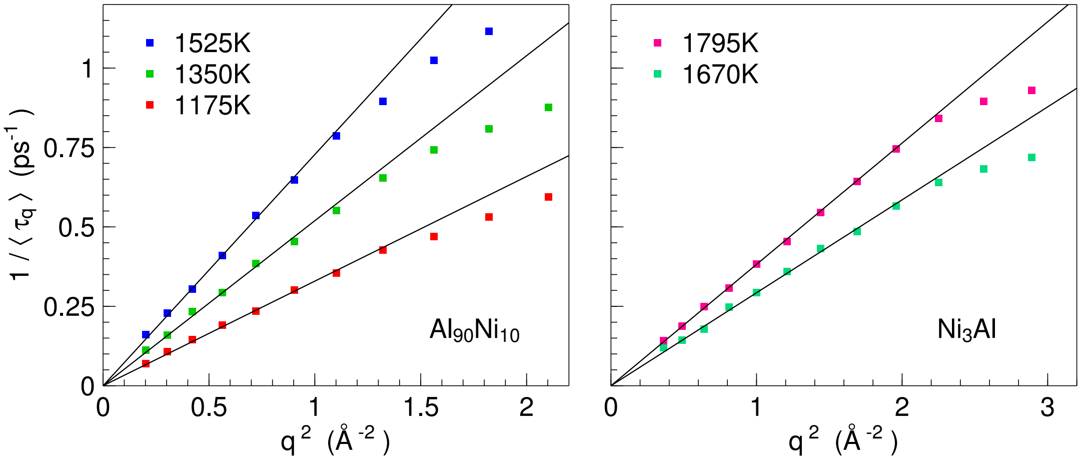

Figure 7.9: The $1/q^2$ dependence of mean relaxation time $\langle\tau_q\rangle$ in $Al_{90}Ni_{10}$ and in $Ni_3Al$ melts. As compared to dense liquids, the $q^2$ dependence deviates at smaller $q$ values. But in $Ni_3Al$ the deviation is comparatively at larger $q$ value.

Ni self-diffusion coefficient in the alloys Al-Ni were derived from the melting temperature up to 1795 K. The alloys investigated were $Al_{100-x}Ni_x$ with x=10, 20, 23, 30, 38 and 75. Figure 7.10 shows the measured Ni self-diffusion coefficient as a function of Al content at 1525 K and 1795 K. At 1795 K the values of $D$ range from $3.96\pm0.10\times10^{-9}m^2s^{-1}$ in $Al_{25}Ni_{75}$ to $10.11\pm0.10\times10^{-9}m^2s^{-1}$ in $Al_{90}Ni_{10}$. The Ni diffusion coefficient in $Al_{25}Ni_{75}$ is equal within the error bar to the value in pure liquid Ni with $D = 3.96 \pm 0.10 \times 10^{-9} \mathrm{m}^2\mathrm{s}^{-1}$. Substitution of 25% Al does not effect the diffusion coefficient significantly. In contrast, on the Al rich side the diffusion coefficient shows a pronounced increase with increasing Al content. The measured Ni self-diffusivities are tabulated in appendix D. The diffusivity calculated from the viscosity data does not obey Stokes-Einstein relation (see fig. 7.10).

The molecular simulation results show, at Al rich side, the values of Ni self-diffusion coefficient well agree with the experimental one. On the other hand in Ni rich side of the composition the value of Ni self-diffusion coefficient are higher by 30% (see figure 7.11). The reason for this behavior is yet not understood.

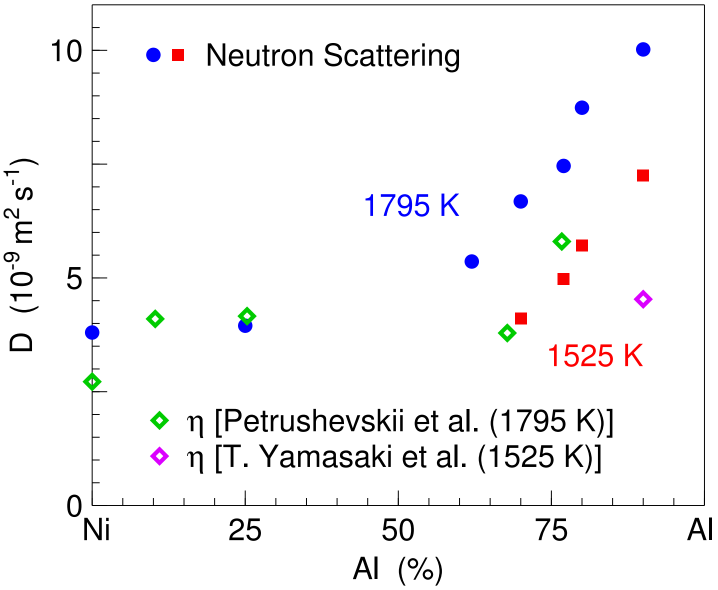

Figure 7.10: Ni self-diffusion in Al-Ni melts at 1795 K and 1525 K observed by neutron scattering and calculated from viscosity data [Pe71, Ya93].

The temperature and composition dependence of the measured diffusion constants are well reproduced by the MD simulation. There is an overall 80% agreement with experimental data (Figure 7.11).

The Ni self-diffusion constants in each of these melts were measured at four to five temperatures. Even though, the number of data points are not enough to calculate the activation enthalpy $E$ for the Ni self-diffusion accurately, it is found to be increased linearly with Ni concentration in Al rich side (Table 7.1). This again indicates that the packing fraction have no influence on the mass transport in these melts.

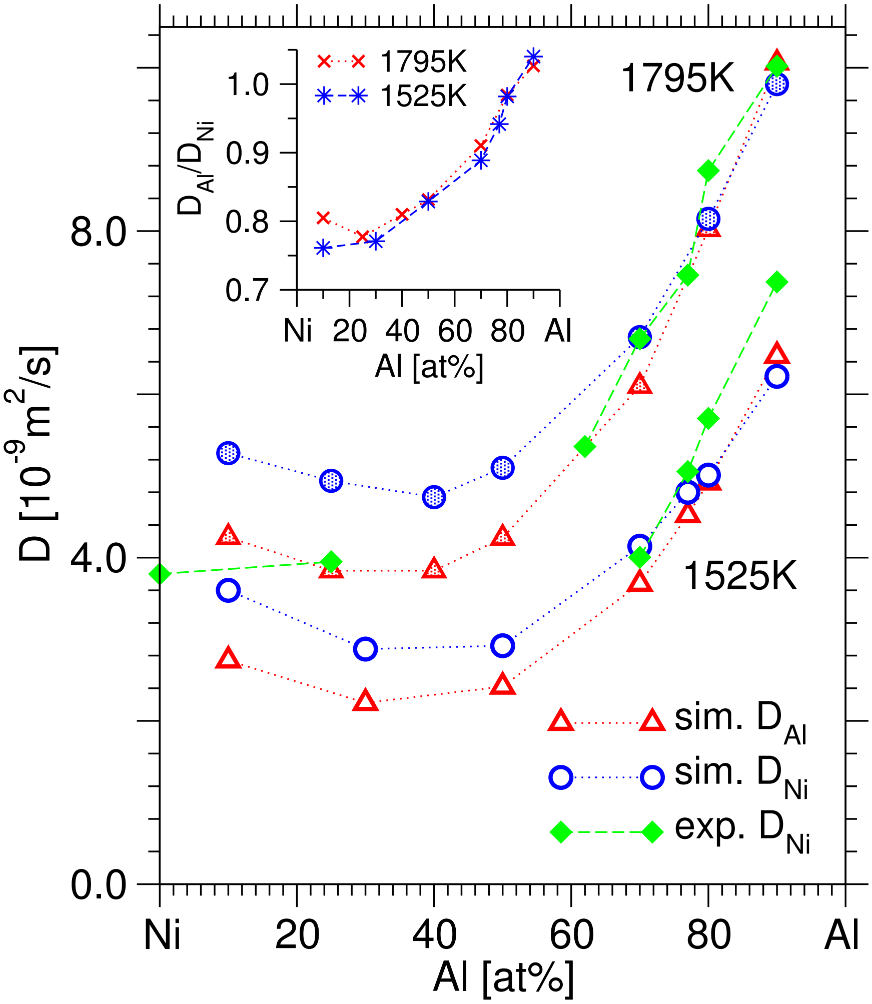

Figure 7.11: A comparison of Ni self-diffusion in Al-Ni melts at 1795 K and 1525 K observed by neutron scattering and MD simulation [Da04].

| *Alloy* | $T_{liq}$ (K) | *Temperature range* (K) | $E_{Ni}$ (kJ mol$^{-1}$) |
|---|---|---|---|
| $Al_{90}Ni_{10}$ | 1073 | 1175 - 1795 | 30.81±0.12 |
| $Al_{80}Ni_{20}$ | 1270 | 1350 - 1795 | 35.15±0.15 |
| $Al_{70}Ni_{30}$ | 1530 | 1550 - 1795 | 40.85±0.16 |

Table 7.1: Activation energy for Ni self-diffusion in Al-Ni melts

## 7.8 Al-Ni and Al-Cu melts

The intermediate structure and microscopic dynamics in $Al_{80}Cu_{20}$ has also been investigated by inelastic neutron scattering. The Ni and Cu atoms possess compa-

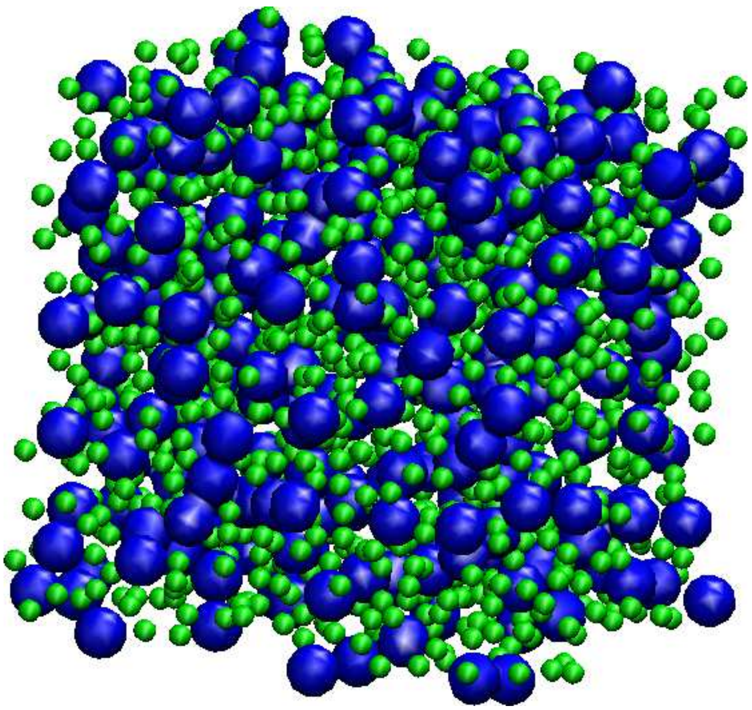

Figure 7.12: A snapshot of $Al_{80}Ni_{20}$ from the MD simulation at 1750 K. The blue spheres represent Ni atoms and green one the Al atoms. It is clear from the figure that the atoms are not distributed randomly because of the CSRO.

rable hard-sphere diameters (twice the covalent radius), $\sigma_{Ni} = 2.3$Å , $\sigma_{Cu} = 2.32$Å, respectively. The quasielastic structure factor of $Al_{80}Cu_{20}$ melts does not show a prepeak, indicating there is no chemical short range order in this melt. The diffusivities of Cu in $Al_{80}Cu_{20}$ melts show 40% faster as compared to Ni in $Al_{80}Ni_{20}$ melts. The activation energy obtained from the measured self-diffusion constants is found to be similar to that of activation energy for Ni self-diffusion in $Al_{80}Ni_{20}$ melts. Since the strength of the CSRO decreases with increasing temperature one would expect a different activation energy in melts that do not show CSRO. Similar activation energies indicate that the CSRO has no influence on the microscopic transport mechanism.

## 7.9 Al-Ni and Al-Ni-Ce melts

The dynamics in Al-Ni-Ce melts has also been studied as the part of the DFG program. Unlike Al-Ni melts, which crystallize while solidifying, the Al-Ni-Ce melts form multicomponent that are crystalline, nano crystalline and amorphous. To understand any changes in the dynamics that relate to the formation of multi-

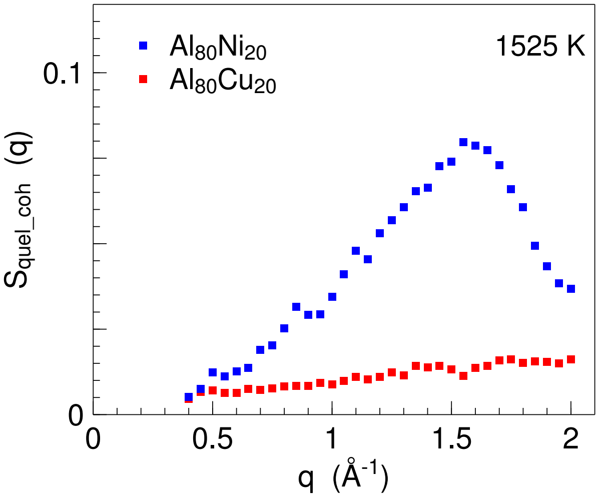

Figure 7.13: The quasielastic structure factor of $Al_{80}Ni_{20}$ and $Al_{80}Cu_{20}$ melts at 1525 K.

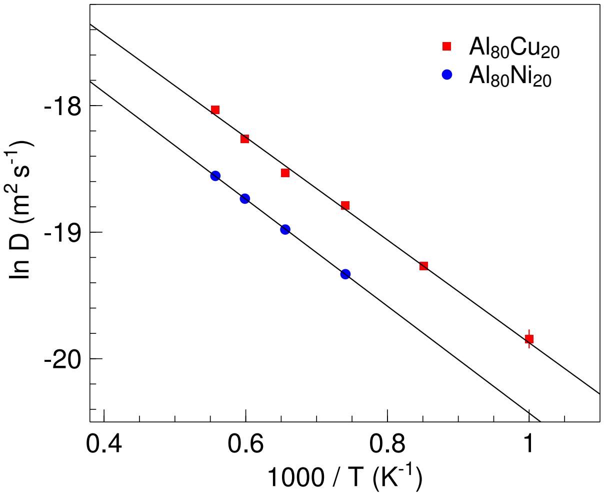

Figure 7.14: Activation energy for Ni self-diffusion in $Al_{80}Ni_{20}$ $E_{Ni} = 35.15\pm0.15$kJ mol$^{-1}$ and for Cu self-diffusion in $Al_{80}Cu_{20}$ melts $E_{Cu} = 33.28\pm0.12$kJ mol$^{-1}$.

phases, we investigated Ni self-diffusivity in Al-Ni-Ce melts. The measured Ni self diffusivities are shown in the figure 7.15. The Ni mobility decreases with the addition of Ce in Al-Ni melts. In $Al_{80}Ni_{20}$, by replacing Al with 3% Ce *i.e* $Al_{77}Ni_{20}Ce_3$, the melting temperature does not change whereas the measured Ni self-diffusivities show a noticeable slow down. For instance, $D_{Ni}$ at 1525 K in $Al_{80}Ni_{20}$ is $5.71\pm0.07\times10^{-9}$m$^2$s$^{-1}$, whereas in $Al_{77}Ni_{20}Ce_3$ it is reduced to $4.21\pm0.11\times10^{-9}$m$^2$s$^{-1}$. These melts also show a prepeak in its structure factor but its maximum is shifted towards larger $q$ value. The activation energy for Ni self-diffusion is also increases while replacing small amount of Al by Ce. For example, the activation energy for Ni self-diffusion in $Al_{84}Ni_{10}Ce_6$ is 42.20±0.15 kJ $mol^{-1}$ whereas in $Al_{90}Ni_{10}$ it is only 30.81±0.12 kJ $mol^{-1}$ (see table 7.2). The slowing down of self-diffusion and an increased activation energy might be the reason for the multiphase formation on solidifying. For the glass forming alloys discussed in the previous chapter the activation energy is still larger.

| *Alloy* | $T_{liq}$ (K) | *Temperature range* (K) | $E_{Ni}$(kJ $mol^{-1}$) |
|---|---|---|---|
| $Al_{87}Ni_{10}Ce_3$ | 1073±1 | 1000 - 1525 | 34.60±0.12 |
| $Al_{77}Ni_{20}Ce_3$ | 1284±2 | 1175 - 1525 | 33.86±0.16 |
| $Al_{70}Ni_{27}Ce_3$ | 1528±2 | 1525 - 1795 | 42.93±0.16 |
| $Al_{87}Ni_7Ce_6$ | 1028±1 | 1175 - 1525 | 38.18±0.16 |
| $Al_{84}Ni_{10}Ce_6$ | 1188±1 | 1200 - 1525 | 42.20±0.15 |

Table 7.2: Activation energy for Ni self-diffusion in Al-Ni-Ce melts

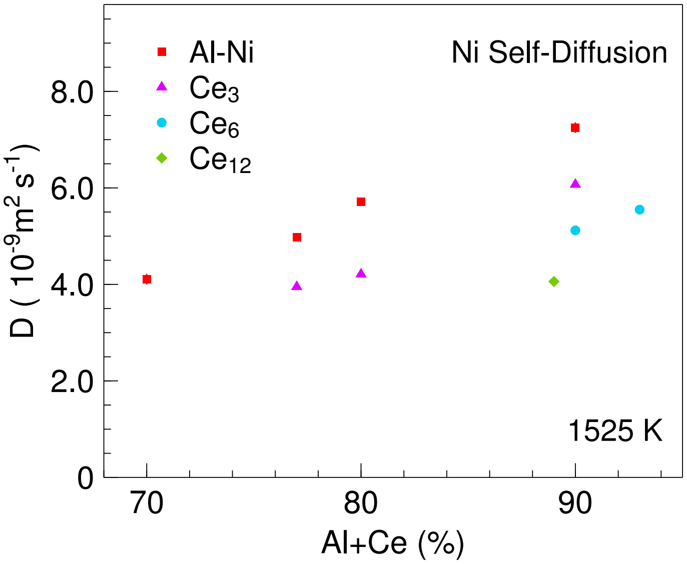

Figure 7.15: Ni self-diffusivities in Al-Ni melts (red squares) and in Al-Ni-Ce melts. Ni self-diffusiviy decreases with increasing Ce content.

# Chapter 8

# Conclusions

## 8.1 Microscopic dynamics in dense liquids

Pure Ni is completely liquid only at 1726 K (liquidus temperature). By adding 20 atomic percent phosphorus, its liquidus temperature decreases to 1171 K, a change of over 550 degree. This alloy becomes glass forming and the DSC measurement on melt spin $Ni_{80}P_{20}$ ribbon shows a glass transition temperature at 612 K. The $Pd_{40}Ni_{40}P_{20}$ alloy shows a better glass forming ability and its liquidus temperature is at 972 K much lower than that of $Ni_{80}P_{20}$. The melting enthalpy of $Pd_{40}Ni_{40}P_{20}$ found to be 10.42±0.04 kJ mol$^{-1}$ and it is quite low as compared to pure Ni (17.5±0.04 kJ mol$^{-1}$). The alloy $Pd_{43}Ni_{10}Cu_{27}P_{20}$ has the highest glass forming ability among the three alloys investigated. Only a cooling rate of 0.1 K s$^{-1}$ is needed to avoid crystallization. On the other hand, the alloy is completely liquid at 863 K, and the melting enthalpy is found to be only 7.01±0.04 kJ mol$^{-1}$. In these liquids, an increasing number of components continuously decreases the melting temperature and the critical cooling rate for glass formation. But the calculated packing fraction from the density data of these systems show a similar value and is about 0.50 at their respective melting points.

The microscopic dynamics in the melts: pure Ni, $Ni_{80}P_{20}$, $Pd_{40}Ni_{40}P_{20}$ and $Pd_{43}Ni_{10}Cu_{27}P_{20}$ has been investigated from melting temperature up to 1795 K, the highest feasible temperature presently available. To obtain the scattering law $S(q,\omega)$ from inelastic neutron scattering, the data were normalized to a vanadium standard, corrected for self absorption and container scattering. Further, $S(q,\omega)$ was symmetrized with respect to the energy transfer $\hbar\omega$ by means of the detailed balance factor. Fourier transformation of $S(q,\omega)$, division of the instrumental resolution function and normalization with the value at $t = 0$ gives the density correlation function $\Phi(q,t)$.

The density correlation functions are then fitted with a stretched exponential function (KWW) $\Phi(q,t) = f_q \exp[-(t/\tau_q)^{\beta}]$. The value of $\beta$ ($\beta < 1$) determines the degree of deviation or stretching from the exponential decay. We found that the $\beta$ value approaches unity at temperatures above the liquidus temperature, corresponding to an exponential decay. At high temperatures the finial decay of density correlation can only observed in the experimental window. The finial decay KWW function is in good approximation is an exponential function. So a systematic change in the value of $\beta$ with alloy composition could not be detected. The rescaled density correlation function for different temperatures fall into a master curve when plotted against rescaled time. This indicates that the time-temperature superposition of structural relaxation holds. In $Pd_{43}Ni_{10}Cu_{27}P_{20}$ melts it holds from 873 K up to a maximum temperature measured. The rescaled density correlation functions are best fitted with a stretched exponential function with a $\beta$ value 0.75.

The $q$ dependence of the mean relaxation time is used to evaluate the self-diffusion coefficients. The $q^2$ dependence of $1/\langle\tau_q\rangle$ holds not only at low $q$ but also at intermediate $q$ values. This is the signature of a collective atomic transport mechanism, which is found only in the dense packed hard-sphere like systems.

The Ni self-diffusivities were measured for all these systems starting from melting temperatures up to 1795 K. Irrespective of the alloy composition the measured diffusivities are found to be similar (within 20%) in all these systems at a given temperature. This indicates that the atomic transport is neither influenced by the changes in composition nor in the thermodynamic properties of the liquids. This finding confirms that the mobility of Ni atoms in the investigated dense hard-sphere like liquids is determined by the packing fraction and this property is similar in all these melts.

The diffusivity is related to the shear viscosity by the Stokes-Einstein relation, $D = 1/6\pi a\eta$, where $a$ is the hydrodynamic radius of the diffusing particle. A comparison of diffusivities obtained from neutron scattering and from shear viscosity shows that this relation holds in $Pd_{43}Ni_{10}Cu_{27}P_{20}$ melts, with $a = 1.15$Å, the tabulated Ni covalent radius [Pa88]. In pure Ni the most recent measurement shows the viscosity value of 1.89±0.06 mP s at 1795 K. The diffusivities calculated from the above value are 40% smaller as compared to that obtained by neutron scattering. The non validity of Stokes-Einstein relation is also found in $Ni_{80}P_{20}$, but in $Pd_{40}Ni_{40}P_{20}$ the disagreement is only 20%. Surprisingly, the Ni self-diffusivity derived from the hard-sphere calculation for liquid Ni by Protopapas *et. al.* agree quite well with our results from the neutron scattering. Convection is a major problem in tracer diffusion measurements, but in neutron scattering we explore the dynamics in the picoseconds range therefore this effect does not play any role. Our value of self-diffusion constants are more accurate compared to those obtained by any other techniques presently available.

## 8.2 Dynamics in melts with CSRO

Short-range order (SRO) refers to the existence of structural order occurring over a range of distance greater than the average nearest-neighbor distance. This gives rise to the so called pre-peak in the structure factor $S(q)$ at a $q$ value smaller than that of the main peak (structure factor maximum). The intermediate structure analysis of Al-Ni melts in section 6.1 reveal the existence of pronounced pre-peaks in Al-Ni melts. Also from the molecular dynamics simulation a clear prepeak in the structure factor is observed. This is a clear signature that the ordering beyond the next nearest neighbor distance is present in the studied system. Although the physical origin of the prepeak is a controversial issue, in this case the SRO can be attributed to the formation of structural units constituted of dissimilar atoms because of chemical affinity between them, namely chemical short range order.

In Al-Ni systems the pre-peak position is found to be strongly dependent on the composition. The maximum of the pre-peak position moves towards higher $q$ values, from 1.6 $Å^{-1}$ in $Al_{80}Ni_{20}$ to 1.8 $Å^{-1}$ in $Al_{62}Ni_{38}$. The intensity of the pre-peak increases with increasing Ni content at the Al-rich side of Al-Ni melts. On the Ni-rich side a broad prepeak is visible and its maximum is found to be located at a smaller $q$ value of around 1.5 $Å^{-1}$. The molecular dynamics simulation by Das and Horbach shows that, in Ni-rich system the distance between Al-Al atoms and Ni-Ni are similar. But on the Al-rich side the distance between repeated Ni-Ni units does not change, but the Al-Al distance becomes larger. This explains the non-linear behaviour of the atomic volume and hence the packing fraction with composition.

The Ni self-diffusion coefficients are derived from the $q^2$ dependence of the mean relaxation time for $q \to 0$. In the above mentioned dense metallic liquids this dependence is found to be valid at the intermediate $q$ values up to 1.8 $Å^{-1}$. In Al-Ni melts, although there is coherent contribution because of CRSO, it is found to be still valid up to 0.6 $Å^{-1}$. But in $Ni_3Al$, where the Ni self- diffusivity is similar to that of pure liquid Ni, the $q^2$ dependence holds comparable to that in the dense liquids. This shows that the increasing packing fraction leads to collective atomic transport that is similar to that at the Ni rich side of the Al-Ni melts. At the Al-rich side, the Ni self-diffusivity shows a linear increase with increasing Al content. On the Al rich side the atomic volume and the packing fraction decreases with increasing Al content. This indicates that the nonlinear behavior of the Ni self-diffusion constant with increasing Al content is due to the change in packing fraction.

Metallic melts with CSRO investigated by inelastic neutron scattering and molecular dynamics simulation shows that the CSRO causes a non-linear variation in atomic volume. Atomic transport is not affected by chemical short range ordering, but is strongly influenced by packing effects.

## 8.3 Future prospects

In the present experimental setup the samples were kept in a container in front of the neutron beam. The material for the sample container is a big constraint for the experiment. Many samples do react with the sample container at high temperature. For our studies we used an Alumina ($Al_2O_3$) container, which easily reacts with alloys like FeNi, ZrNiAl, that are also interesting systems to investigate. Another fact to consider is the temperature at which one can investigate liquid metals. Since the melting temperatures of many alloys are at very high temperature, to study the temperature dependence of self-diffusion, a high temperature furnace is needed for the experiments. The presently available high temperature furnace at the ILL can go only up to a maximum 1800 K. Another matter of concern is that the flux from the neutron source.

Electromagnetic levitation is a promising technique for the future. By this technique, it is possible to avoid the container and the temperature can be varied to a desired value. With this technique, an electrically conductive sample of 6-10 mm diameter is levitated and kept in an inhomogeneous electromagnetic RF field. Eddy currents are induced in the specimen which leads to melting. On the other hand, the interaction of eddy currents with the inhomogeneous magnetic field of the levitation coil leads to a force that gets compensated with the gravitational pull. The sample is then able to elevate in the solid or liquid state. The specimen is then free from container and the temperature can be set to any desired value by just increasing or decreasing the current through the coils. This container-less technique is most advantageous for studying undercooled metallic melts. Since the samples are not in contact with any surfaces, it is possible to undercool the liquids well below their melting temperature (e. g. liquid Ni was able to undercool up to 300 K [Sc02]). In most cases the sample container acts as a nucleation site for crystallization. The melts get easily crystallized when in contact with surfaces. This problem can be avoided in the levitation techniques. Figures 8.1 shows the experimental setup for

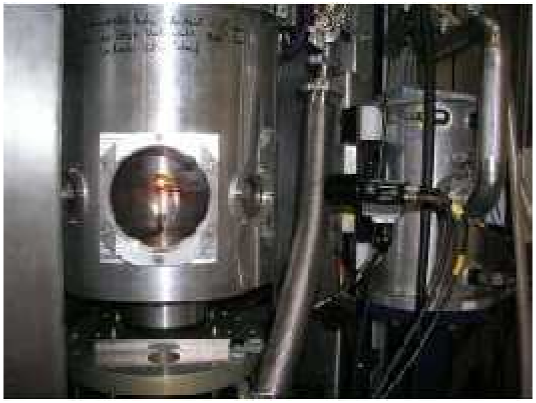

Figure 8.1: The experimental setup for the levitated neutron scattering techniques. A bright spot in the figure shows the levitated Ni droplet in a He filled chamber.

levitated neutron scattering.

We have already performed a neutron scattering experiment with this levitation technique at FOCUS, PSI Switzerland in collaboration with D. Holland-Moritz and D.M. Herlach (DLR Cologne). We studied Ni dynamics in its undercooled state. It was possible to undercool the sample up to 200 degree more than 20 hours. The result of the experiment is shown in figure 8.2. Due to high background and low flux with this experiment we could not study the structural relaxation. The development of a high flux neutron source like FRM II, with 4-5 times higher flux, and adapting a new induction coil in the levitation setup with a wider angle to cover more scatted neutrons expected to provide 10 times higher neutron counts per second as compared to the present study. The first measurement on TOF-TOF spectrometer at FRM II shows the background is comparable to IN6 and it is 10 time lower comparable to that of FOCUS. In future the levitation technique can be used to study more complex dynamics in liquid metals and alloys especially in their undercood state.

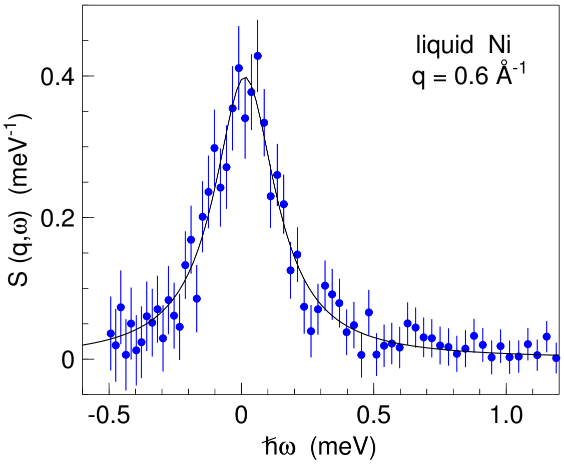

Figure 8.2: Results of neutron scattering on a levitated undercooled liquid Ni. The Ni self-diffusivity obtained from fitting the data points with a Lorentzian function and by the formula $D = \Gamma/2\hbar q^2$ was found to be 2±1 × $10^{-9}\mathrm{m}^2\mathrm{s}^{-1}$ at 1577 K.

# Appendix A

# Alphabetic list of quantities and abbreviation

| | | | |
|---|---|---|---|
| $a$ | hydrodynamic radius | $b_i$ | scattering length of nuclei |
| $D$ | self-diffusion constant | $\tilde{D}$ | chemical diffusion constant |
| $\alpha$ | X-ray absorption coefficient | $T_m$ | melting temperature |
| $\beta_s$, $\zeta$ | sliding friction coefficient | $T_x$ | crystallization temperature |
| $\beta_q$ | stretching exponent | $T_c$ | critical temperature |
| $\gamma$ | contact angle | $T_g$ | glass transition temperature |
| $\epsilon$ | scale parameter | $T_{liq}$ | liquidus temperature |
| $\eta$ | dynamic viscosity | $\sigma_{abs}$ | absorption cross section |
| $\lambda$ | wavelength | $\sigma_{coh}$ | coherent scattering cross section |
| $\varphi$ | packing fraction | $\sigma_{inc}$ | incoherent scattering cross section |
| $\eta$ | dynamic viscosity | $S_{quel\_coh}$ | quasielastic structure factor |
| $\rho$ | liquid or solid density | $k_B$ | Boltzmann constant |
| $\langle\tau_q\rangle$ | mean relaxation time | $R$ | Universal gas constant |
| $q$ | momentum transfer | $n_0$ | Number density |
| $\nu$ | Kinematic viscosity | $g(\omega)$ | phonon density of state |
| $\sigma_d$ | inter atomic distance | $g(r)$ | pair distribution function |
| $\sigma$ | hard-sphere diameter | $V_m$ | volume at melting |
| $K$ | temperature in Kelvin | $G(r,t)$ | pair correlation function |
| $x_\alpha$ | atomic fraction | $G_s(r,t)$ | self correlation function |
| $\psi_v(t)$ | velocity autocorrelation | $S(q,\omega)$ | dynamic structure factor |
| $v_f$ | free volume | $n_{el}$ | elastic channel number |
| $W$ | Debye-Waller-Factor | $2\theta$ | scattering angle |
| $k_i$ | incident wave vector | $k_f$ | scattered wave vector |
| $\Phi(q,t)$ | density correlation function | $m_n$ | The mass of neutron |

# Appendix B

# List of neutron scattering experiments

**FOCUS, August 2002**
$\lambda = 5.4$Å
elastic peak 304/946
energy resolution 133$\mu$eV
high temperature furnace
$Al_2O_3$ hollow cylinder
elastic focusing

| substance | temperature [K] | time [min] |
|---|---|---|
| $Pd_{40}Ni_{40}P_{20}$ | 300, 963, 1206<br>1296, 1383 | 500 - 600 |

**IN6, November 2002**

$\lambda = 5.1$Å
elastic peak 637/1024
channel width 4.75 $\mu$s
energy resolution 97$\mu$eV
$Al_2O_3$ hollow cylinder
elastic focusing

| substance | temperature [K] | time [min] |
|---|---|---|
| $Ni_{80}P_{20}$ | 300, 1183, 1255<br>1390, 1525, 1670, 1795 | 60 |
| Ni | 300, 1735, 1795 | 60 |
| $Al_{80}Ni_{20}$ | 300, 1011, 1350<br>1525, 1670, 1795 | 120 |
| $Ni_3Al$ | 300, 1670, 1795 | 120 |
| $Pd_{43}Ni_{10}Cu_{27}P_{20}$ | 300, 1255, 1390<br>1525, 1670, 1795 | 180 |

**IN6, April 2003**
$\lambda = 5.1$Å
elastic peak 637/1024
channel width 4.75 $\mu$s
energy resolution 97$\mu$eV
$Al_2O_3$ hollow cylinder
elastic focusing

| substance | temperature [K] | time [min] |
|---|---|---|
| $Al_{77}Ni_{20}Ce_3$ | 300, 1000, 1175<br>1350, 1525 | 120 |
| $Al_{87}Ni_{20}Ce_3$ | 300, 1000, 1175<br>1350, 1525 | 120 |

**IN6, October 2003**

$\lambda = 5.1$Å
elastic peak 637/1024
channel width 4.75 $\mu$s
energy resolution 97 $\mu$eV
high temperature furnace
$Al_2O_3$ hollow cylinder
elastic focusing

| substance | temperature [K] | time [min] |
|---|---|---|
| $Al_{90}Ni_{10}$ | 300, 1000, 1175,<br>1350, 1525, | 180 |
| $Al_{70}Ni_{30}$ | 300, 1175, 1350<br>1525, 1670, 1795 | 120 |
| $Al_{87}Ni_7Ce_6$ | 300, 1350<br>1525, 1750 | 180 |
| $Al_{84}Ni_{10}Ce_6$ | 300, 1000,b1175<br>1350, 1525 | 180 |
| $Al_{77}Ni_{23}$ | 300, 1350, 1525 | 120 |
| $Al_{80}Ni_{20}$ | 300, 870, 1000<br>1175, 1525, 1670<br>1795 | 120 |

**FOCUS, December 2003**

$\lambda = 4.8$Å
elastic peak 304/956
Levitation technique
elastic focusing

| substance | temperature [K] | time [min] |
|---|---|---|
| Ni(Undercooled) | 300, 1577 | 2400 |

**IN6, April 2004**

$\lambda = 5.1$Å
elastic peak 637/1024
channel width 4.75 $\mu$s
elastic focusing

| substance | temperature [K] | time [min] |
|---|---|---|
| $Al_{77}Ni_{11}Ce_{12}$ | 300, 1350, 1525 | 180 |
| $Al_{77}Ni_{20}La_3$ | 300, 1350, 1525 | 120 |

**IN6, June 2004**

$\lambda = 5.1$Å
elastic peak 637/1024
channel width 4.75 $\mu$s
high temperature furnace
$Al_2O_3$ hollow cylinder
elastic focusing

| substance | temperature [K] | time [min] |
|---|---|---|
| $Al_{62}Ni_{38}$ | 300, 1795 | 120 |
| $Al_{77}Ni_{23}$ | 300, 1670,1795 | 120 |
| $Al_{77}Ni_{20}Ce_3$ | 300, 1670,1795 | 120 |
| $Al_{90}Ni_{10}$ | 300, 1670, 1795 | 180 |
| $Pd_{43}Ni_{10}Cu_{27}P_{20}$<br>(Glassy state) | 300 | 180 |

# Appendix C

# Ni self-diffusion in dense metallic melts

| **Alloy** | **Temperature ( K )** | $D \times 10^{-9}\mathrm{m^2s^{-1}}$ |
|---|---|---|
| Ni | 1795 | 3.80±0.06 |
| | 1735 | 3.27±0.04 |
| $\mathrm{Ni_{80}P_{20}}$ | 1795 | 4.65±0.05 |
| | 1670 | 3.70±0.06 |
| | 1525 | 2.72±0.06 |
| | 1390 | 1.96±0.06 |
| | 1255 | 1.21±0.06 |
| | 1183 | 0.89±0.06 |
| $\mathrm{Pd_{40}Ni_{40}P_{20}}$ | 1383 | 2.23±0.11 |
| | 1293 | 1.73±0.08 |
| | 1203 | 1.22±0.07 |
| | 1063 | 0.55±0.03 |
| | 963 | 0.26±0.03 |
| $\mathrm{Pd_{43}Ni_{10}Cu_{27}P_{20}}$ | 1795 | 4.74±0.18 |
| | 1670 | 3.97±0.10 |
| | 1525 | 2.90±0.07 |
| | 1390 | 2.09±0.11 |
| | 1255 | 1.41±0.18 |

# Appendix D

# Ni self-diffusion in Al-Ni, Al-Cu and Al-Ni-Ce melts

| **Alloy** | **Temperature ( K )** | $D \times 10^{-9}\mathrm{m^2s^{-1}}$ |
|---|---|---|
| $Ni_3Al$ | 1795 | 3.95±0.10 |
| | 1670 | 3.05±0.17 |
| $Al_{90}Ni_{10}$ | 1795 | 10.05±0.11 |
| | 1670 | 8.66±0.04 |
| | 1525 | 7.25±0.11 |
| | 1350 | 5.13±0.04 |
| | 1175 | 3.40±0.07 |
| | 1000 | 2.60±0.03 |
| $Al_{80}Ni_{20}$ | 1795 | 8.74±0.09 |
| | 1670 | 7.30±0.08 |
| | 1525 | 5.71±0.07 |
| | 1350 | 4.02±0.06 |
| | 1011* | 2.35±0.18 |
| $Al_{70}Ni_{30}$ | 1795 | 6.68±0.04 |
| | 1670 | 5.39±0.11 |
| | 1525 | 4.11±0.11 |
| | 1350 | 3.29±0.16 |
| | 1175* | 2.75±0.27 |
| $Al_{77}Ni_{23}$ | 1795 | 7.46±0.07 |
| | 1525 | 4.98±0.07 |
| | 1350 | 2.98±0.09 |
| $Al_{62}Ni_{38}$ | 1795 | 5.36±0.07 |

| **Alloy** | **Temperature ( K )** | $\boldsymbol{D \times 10^{-9} m^2 s^{-1}}$ |
|---|---|---|
| $Al_{87}Ni_{10}Ce_3$ | 1525 | 6.07±0.06 |
| | 1350 | 4.24±0.06 |
| | 1175 | 2.70±0.09 |
| | 1000 | 1.93±0.11 |
| $Al_{77}Ni_{20}Ce_3$ | 1525 | 4.21±0.11 |
| | 1350 | 2.62±0.04 |
| | 1175 | 1.88±0.08 |
| | 1000* | 1.82±0.16 |
| $Al_{84}Ni_{10}Ce_6$ | 1525 | 5.12±0.08 |
| | 1350 | 3.35±0.04 |
| | 1175 | 1.90±0.03 |
| | 1000* | 1.88±0.18 |
| $Al_{87}Ni_7Ce_6$ | 1525 | 5.55±0.10 |
| | 1350 | 3.90±0.07 |
| | 1175 | 2.27±0.07 |
| | 1000* | 1.93±0.19 |
| $Al_{70}Ni_{27}Ce_3$ | 1795 | 6.55±0.10 |
| | 1670 | 5.48±0.07 |
| | 1525 | 3.95±0.07 |
| $Al_{77}Ni_{11}Ce_{12}$ | 1525 | 4.06±0.06 |
| | 1350 | 2.35±0.04 |
| $Al_{77}Ni_{20}La_3$ | 1525 | 4.65±0.07 |
| | 1350 | 3.11±0.05 |
| $Al_{80}Cu_{20}$ | 1795 | 14.71±0.09 |
| | 1670 | 11.73±0.12 |
| | 1525 | 8.94±0.13 |
| | 1350 | 6.91±0.07 |
| | 1175 | 4.29±0.09 |
| | 1000 | 2.41±0.18 |

* coexistence of crystalline and liquid phase

# Appendix E

# Acknowledgments

First and foremost, I wish to thank sincerely my adviser Prof. Dr. Andreas Meyer for accepting me as his Ph.D. student, for his competent direction, valuable insights and continuous support both within and beyond this dissertation work. His warm personality and excellent academic guidance has made this work possible.

I express my sincere gratitude towards our chair Prof. Dr. Winfried Petry for his encouragement, helps and advice.

My special thanks to Dr. M. M. Koza, Dr. H. Schober at Institute of Laue-Langevin and Dr. S. Janssen, Dr. F. Juranyi, Dr. A. Podlesnyak at Paul Scherrer Institute for their assistance and cooperation during the experiments.

My acknowledgments also goes to Priv.-Doz. Dr. Walter Schirmacher for being a critical reviewer of my dissertation and for his constructive suggestions. I am also thankful to my colleagues Mr. F. Kargl, Mr. T. Mehaddene and others for their helps and friendliness.

I am grateful to the *Deutscher Forschungsgemeinschaft* (DFG) for financial support for this work within the special priority program 1120 "*Phase transitions in multicomponent melts*" under contract number Me1958/2-1,2.

Finally, I would like to take this opportunity to thank my wife and parents back home for all the support throughout the years. It would have been impossible for me to finish this work here without their support and encouragement.

Garching
10.05.2005 Suresh Mavila Chathoth

# Appendix F

# Publications

1. *Atomic Diffusion in Liquid Ni, NiP, PdNiP and PdNiCuP Alloys.* S. Mavila Chathoth, A. Meyer, M.M. Koza, F. Juranyi Appl. Phys. Lett. 85, 4881 (2004).

2. *The Influence of Chemical Short Range Order on Atomic Diffusion in Al-Ni Melts.* S.K. Das, J. Horbach, M.M. Koza, S. Mavila Chathoth, A. Meyer, Appl. Phys. Lett. 86, 011918 (2005).

3. *Ni and Ce Self-diffusion in AlNiCe Melts*, S. Mavila Chathoth, A. Meyer, A. Griesche, M.-P. Macht and G. Frohberg and M.M. Koza, (in preparation).

# Bibliography

[Ad65] G. Adams and J. H. Gibbs, J. Chem. Phys. **43**, 139 (1965).

[Al74] B. J. Alder, W. E. Alley and J. H. Diamond, J. Phys. Chem. **61**, 1415 (1974).

[Al04] Alok Samanta, Sk. Musharaf Ali, and Swapan. K. Ghosh, Phys, Rev. Lett. **92**, 145901 (2004).

[An52] E. N. da C. Andrade and E. R. Dobbs, Proc. R. Soc. **A211**, 12 (1952).

[An95] C.A. Angell, Science. **267**. 1924 (1995).

[Ar66] N. W. Aschroft and J. Lekner, Phys. Rev. **145**, 83 (1966).

[Ar92] V. I. Arnold, *Catastrophe Theory, 3rd ed.*, Springer Verlag, Berlin (1992).

[As99] M. Asta, D. Morgan, J. J. Hoyt, B. Sadigh, J. D. Althoff, D. de Fontaine and S. M. Foiles, Phys. Rev. B **59**, 14271 (1999).

[Ay69] G. D. Ayushina, E. S. Levin and P.V. Geld, Russ. J. Phys. Chem. **43**, 2756 (1969).

[Ba83] F. Bashforth and J. C. Adams, *An attempt to test the theories of capillary action*, Cambridge University Press (1883).

[Ba94] U. Balucani and M. Zoppi, *Dynamics of the Liquid State*, Clarendon, Oxford (1994).

[Ba83] G. I. Batalin, E. A. Beloborodova and V. G. Kazimirov, *Thermodynamics and the Constitution of Liquid Al Based Alloys*. Metallurgy, Moscow (1983).

[Be84] U. Bengtzelius, W. Götze and A. Sjölander, J. Phys. C. **17**, 5915 (1984).

[Be88] M. Bée, *Quasielastic neutron Scattering: Principles and Applications in Solids State Chemistry, Biology and Material Science*, Adam Hilger, Bristol and Philadelphia (1988).

[Be72] R. T. Beyer and E. Ring, *Liquid metals: Chemistry and Physics*, edited by S. Z. Beer, Dekker, New york (1972).

[Bi60] R. B. Bird, W. E. Stewart and E. N. Lightfoot, *Transport phenomena. Ch. 1*, John and Wiley and Sons, New York (1960).

[Bi00] D. P. Landau and K. Binder, *A guide to Monte Carlo Simulation in Statistical Physics*, Cambridge University press, Cambridge (2000).

[Bo69] J. O. M. Bockris. L. J. White and J. D. Mackenzie, *Physiochemical measurements at high temperatures*, Butterworth, London (1969).

[Bo93] R. Böhmer, K. L. Ngai, C. A. Angell, and D. P. Plazek, J. Chem. Phys. **99**, 4201 (1993).

[Bo80] J. P. Boon, S. Yip, *Molecular Hydrodynamics*, McGraw-Hill, New York (1980).

[Bu97] E. Budke, P. Fielitz, M.-P. Macht, V. Naundorf, and G. Frohberg, Defect and Diffusion Forum **143-147**, 825 (1997).

[Ch93] K. C. Chow, S. Wong and H. W. Kui, J. Appl. Phys. **74**, 5410 (1993).

[Ch91] R. W. Cahn, in *Glasses and Amorphous Materials*, J. Zarzycki, Ed., vol. 9 of Materials Sciences and Technology, edited by R. W. Cahn, P. Haasen, and E. J. Kramer, pp. 493-548, VCH Press, Weinheim (1991).

[Ch39] S. Chapman and T. G. Cowing *The mathematical Theory of Non-Uniform Gases*, Cambridge University Press, Lndon (1939).

[Ch66] T. W. Chapman, J. Am. Inst. Chem. Eng. **12** 395 (1966).

[Ch97] I. Chang and H. Sillesiu, J. Phys. Chem. B **101**, 8794 (1997).

[Ch68] H. S. Chen and D. Turnbull, J. Chem. Phys. **48**, 12560 (1968).

[Ch78] H. S. Chen, J. non-Cryst. Solids **29**, 223 (1978).

[Cl60] W. Clement, R. H. Willems and P. Duwez, Nature **187**, 869 (1960).

[Co59] M. H. Cohen and D. Turnbull, J. Chem. Phys **31**, 1164 (1959).

[Co92] J. Colmenero, A. Alegra, A. Arbe and B. Frick, Phys. Rev. Lett. **69**, 478 (1992).

[Co94] J. Colmenero, A. Arbe, A. Alegra, and K. L. Ngai, J. Noncryst. Solids **172 174**, 126 (1994).

[Cr74] A. F. Crawley, Int. Met. Rev. **19**, 32 (1974).

[Da04] S. K. Das, J. Horbach, M. M. Koza, S. Mavila Chathoth and A. Meyer, Appl. Phys. Lett. **85**, 011918 (2005).

[Da76] H. A. Davies, Phys. Chem. Glass **17**, 159 (1976).

[Dr82] A. J. Drehman, A. L. Geer and D. Turnbull. Appl. Phys. Lett. **41**, 716 (1982).

[Du93] Peter A. Duine, Jilt Sietsma and A, van den Beukel, Phy. Rev. B **48**, 6957 (1993).

[Du35] J. R. Dunning, G. B. Pegram, G. A. Fink, D. P. Mitchell and E. Segré, Phys. Rev. **48**, 704 (1935).

[Dz96] Z. Dzugutov, Nature **381**, 137 (1996).

[Eh99] H. Ehmler, K. Rätzke and F. Faupel, J. Non-Cryst. Solids **250-252**, 684 (1999).

[Fa72] T. E. Faber, *An Introduction to the Theory of Liquid Metals* Cambridge University press, Cmbridge, (1972).

[Fa04] G. J. Fan, J. F. Löffler, R. K. Wunderlich and H. -J. Fecht, Acta Materialia **52**, 667 (2004).

[Fe47] E. Fermi, J. Marshall and L. Marshall, Phys. Rev. **72**, 193 (1947).

[Fi99] P. Fielitz, M.-P. Macht, V. Naundorf, and G. Frohberg, J. Non-Cryst. Solids **250-252**, 674 (1990).

[Fr03] F. Faupel, W. Frank, M. P. Macht, H. Mehrer, V. Naundorf, K. Rätzke, H. R. Schober, S. K. Sharma and H. Teichler, Rev. Mod. Phys. **75**, 237 (2003).

[Fr87] G. Frohberg, K.-H. Kratz and H. Wever, Mater. Sci. Forum **15-18**, 529 (1987).

[Fr97] G. Frohberg, Defect and Diffusion Forum **143-147**, 869 (1997).

[Fu60] K. Furukawa, Sci. Rep. Res. Inst. Tohoku Univ. **12A**, 368 (1960).

[Fu94] M. Fuchs, J. Non-Cryst. Solids **172-174**, 241 (1994).

[Fu99] M. Fuchs, I. Hofacker and A. Latz, Phys. Rev. A **45**, 898 (1992).

[Ge55a] E. Gebhardt, M. Becker and E. Trügner, Z. Metallkde **46**, 90 (1955).

[Ge55b] E. Gebhardt, M. Becker and H. Sabastien, Z. Metallkde **46**, 669 (1955).

[Ge58] E. Gebhardt and K. Köstlin, Z. Metallik. **49**, 605 (1958).

[Go92] W. Götze and L. Sjögren, Rep. Prog. Phys. **55**, 241 (1992).

[Gr04] A. Griesche, M. P. Macht, J. P. Garandet, G. Frohberg, J. Non-Cryst Solid **336**, 173 (2004).

[Gr98] K. V. Grigorovitch and A. S. Krylov, Thermochem. Acta. **314**, 255 (1998).

[He60] E. Helfand and S. A. Rice, J. Chem. Phys. **32**, 1642 (1960).

[Hi90] K. Hilpert, M. Miller, H. Gerads and H. Nickel, Ber. Bunsenges. Phys. Chem. **94**, 40 (1990).

[Hy00] J. J. Hoyt, M. Asta, and B. Sadigh, Phys. Rev. Lett. **85**, 594 (2000).

[Il02] A. Ilinskii, S. Slyusarenko, O. Slukhovskii, I. Kaban and W. Hoyer, Mater. Sci. Eng. A **325**, 98 (2002).

[In89] A. Inoue, T. Zang and T. Masumoto, Mater. Trans. JIM **30**, 965 (1989).

[In01] A. Inoue, A. R. Yavari, W. L. Jonhson and R. H. Dauskardt, *Supercooled Liquid, Bulk glassy and Nanocrystalline States of Alloys.* Materials Research society symposium proceedings, Vol. **644**, Materials Research Society, Warrendale, PA (2001).

[Jo80] G. R. Johnson and L. D. Palmer, High Temp. High Press. **12**, 261 (1980).

[Jo99] W. L. Jonhson, A. Inoue and C. T. Liu, *Bulk Metallic Glasses.* Materials Research society symposium proceedings, Vol. **554**, Materials Research Society, Warrendale, PA (1999).

[Ji98] Q. Jingyu, B. Xiufang, S. I. Sliusarenko, and W. Weimin, J. Phys.: Condens. Matter. **10**, 1211 (1998).

[Ju87] J. Hafner, *From Hamiltonians to Phase Diagrams*, Springer (1987).

[Ju94] J. Brillo and I. Egry, Z. Metallkd. **95**, 691 (1994).

[Ko99] K. Knorr, M.-P. Macht, K. Freitag, and H. Mehrer, J. Non-Cryst. Solids **250**, 669 (1999).

[Ko00] K. Knorr, M.-P. Macht, and H. Mehrer, in *Materials Development and Processing Bulk Amorphous Materials, Undercooling and Powder Metallurgy*, edited by J. V. Wood, L. Schultz and D. M. Herlach (VCH, Weinheim), p. 22. (2000).

[Kr87] J. S. Kirkaldy and D. Y. Yang, *Diffusion in the condense state*, Institute of Metals London (1987).

[Ku79] O. Kubaschewski, C. B. Alcock, *Metallugrical thermochemistry*, Pergamon Press, Oxford (1979).

[Ku84] H. W. Kui, A. L. Geer and D. Turnbull, Appl. Phys. Lett. **45**, 615 (1984).

[La86] J. S. Langer, *Directions in Condensed Matter*, World Scientific, Singapore (1986).

[Le91] J. A. Leegwater, J. Chem. Phys. **94**, 7402 (1991).

[Li99] Z. Lin, W. Youshi, B. Xiufang, L. Hui, W. Weimin, L. Jingguo and L. Ning, J. Phys.: Condens. Matter **11**, 7959 (1999).

[Lu70] *Techniqus of metals research*, Vol. 4, Pat 2, Interscience Publishers, new york, (1970).

[Lu02] I. -R. Lu, G. P. Görler, H. J. Fecht, R. Willnecker, J. Non-Cry Solids **312-314**, 547 (2002).

[Lu99] I. -R. Lu, G. Wilde, G. P. Görler and R. Willnecker, J. Non-Cry. Solids **250-252**, 577 (1999).

[Ma77] Y. Marcus, *Introduction to liquids state chemistry. Ch. 8*, John. Wiley and sons, London (1977).

[Ma86] D. Mayou, D. Nguyen-Manh, A. Pasturel and F. Cyrot-Lackmann, Phys. Rev. B **33**, 3384 (1986).

[Ma90] M. Maret, T. Pomme, A. Pasturel and P. Chieux, Phys. Rev. B **42**, 1598 (1990).

[Ma95] T. Masumoto, Sci. Rep. RITU A **39**, 91 (1994); A. Inoue, Mater. Trans., JIM **36**, 866 (1995).

[Me90] H. Mehrer, Landolt-Brnstein New Series III, Springer-Berlin, Vol. 26 (1990).

[Mg63] P. J. McGonigal and A. V. Grosse, J. Phys. Chem. **85**, 197 (1963).

[Me01] A. Meyer, H. Schober and J. Neuhaus, Phys. Rev. B **63**, 212202 (2001).

[Me02] A. Meyer, Phys. Rev. B **66**, 134205 (2002).

[Me03] A. Meyer, W. Petry, M. Koza and M.-P. Macht, Appl. Phys. Lett. **83**, 3894 (2003).

[Me98] A. Meyer, J. Wuttke, W. Petry, O. G. Randl and H. Schober Phys. Rev. Lett. **80**, 4454 (1998).

[Me99] A. Meyer, R. Busch and H. Schober, Phys. Rev. Lett. **83**, 5027 (1999).

[Me93] Peter. A . Dunie, Jilit Sietsma and A. van den Beukel, Phys. Rev. B **48**, 6957 (1993).

[Me93] W. van Megen and S. M. Underwood, Phys. Rev. Lett. **70**, 2767 (1993).

[Mi02] Y. Mishin, M. J. Mehal and D. A. Papaconstantopoulos, Phys. Rev. B **65**, 224114 (2002).

[Mo64] E. A. Moelwyn-Hughes, *Physical Chemistry*, p 273, Perggamon, Oxford (1964).

[Mo76] Z. Morita, T. Iida, M. Ueda, *The 140th Committe the Japan Society for the promotion of Science* (JSPS), Rep. No. 45, Dec. (1976).

[Mo86] C. Morkel and W. Gläser, Phys. Rev. A **33**, 3383 (1986).

[Mo87] C. Morkel, C. Gronemeyer, W. Gläser and J. Bosse, Phys. Rev. Lett. **58**, 1873 (1987).

[Na67] N. H. Nachtrieb, Adv. Phys. **16**, 309 (1967).

[Ni85] Y. Nishi and A. Yoshihiro, Scripta Metallugrica **19**, 1023 (1985).

[Ni02] N. Nishiyama and A. Inoue, Appl. Phys. Lett. **80**, 586 (2002).

[Pa62] H. H. Paalman and C. C. J. Pring, J. Appl. Phys. **33**, 2635 (1962).

[Pa67] A.D. Pasternak and D.R. Olander. J. Am. Inst. Chem. Eng. **13**, 1052 (1967).

[Pa72] A. D. Pasternak, Phys. Chem. Liquids **3**, 41 (1972).

[Pa88] W. Paszkowicz, J. Phys. F: Met. Phys. **18**, 1761 (1988).

[Pe71] M.S. Petrushevskii, E.C. Levin, and P.V. Geld, Russ. J. Phys. Chem. **45**, 1719 (1971).

[Pe93] A. Peker und W. L. Johnson, Appl. Phys. Lett. **63**, 2342 (1993).

[Pi03] W. -C. Pilgrim and C. Morkel, Z. Phs. Chem. **217**, 957 (2003).

[Ph93] L. Do Phuong, D. Nguyen Manh and A. Pasturel, Phys. Rev. Lett. **71**, 372 (1993).

[Po72] D. Polk and D. Turnbull, Acta Metall. **20**, 493 (1972).

[Po78] D. Polk and B. C. Giessen, in *Metallic Liquids* (edited by J. J. Gillman and H. J. Leamy), Am. Soc. Metals. Metals Park, Ohio (1978).

[Pr73] P. Protopapas, H. C. Anderson and N. A. D. Parlee, J. Chem. Phys. **59**, 15 (1973).

[Pr03] B. Predel, edited by O. Madelung, *Phase Equilibria of Binary Alloys*, Springer, Berlin (2003).

[Ra64] A. Rahman, Phys. Rev. **159**, A405 (1964).

[Ra83] S. Ranganathan, Can. J. Phys. **61**, 1655 (1983).

[Re01] A. Rehmet, K. Rätzke, F. Faupel, P. D. Eversheim, K. Freitag, U. Geyer and S. Schneider, App. Phys. Lett. **79**, 2892 (2001).

[Ri80] M.R. Riazi and T.E. Daubert. J. Am. Inst. Chem. Eng. **26**, 386 (1980).

[Ro69] F. A. Rossini and W. D. Knight, Phys. Rev. **178**, 641 (1969).

[Ro77] Y. Rosenfeld, Phys. Rev. A **15**, 2545 (1977).

[Sa71] V. M. Sandakov, Yo. O. Esin and P. V. Geld, Russ. J. Phys. Chem. **45**, 1798 (1971).

[Sa94] S. Saadeddine, J. F. Wax, B. Grosdidier, J. Gasser, C. Regnaut and J. M. Dubois, Phys. Chem. Liq. **28**, 221 (1994).

[Sa00] Y. Sato, T. Nishizuka, K. Hara, T. Yamamura and Y. Waseda, Int. J. Thermophys. **21**, 1463 (2000).

[Sa02] Y. Sato, T. Nishizuka, K. Hara and T. Yamamura, *Proceedings of the 16th European Conference on Thermophysics*, London (2002).

[Sc00] J. Schroers, W. L. Johnson, and R. Busch, Appl. Phys. Lett. **77**, 1158 (2000).

[Sc01] H. R. Schober, Solid State Commun. **119**, 73 (2001).

[Sc02] T. Schenk, D. Holland-Moritz, V. Simonet, R. Bellissent and D. M. Herlach, Phys. Rev. Lett. **89**, 075507 (2002); T. Schenk, V. Simonet, D. Holland-Moritz, R. Bellissent, T. Hansen, P. Convert and D. M. Herlach. Europhys. Lett. **65**, 34 (2004).

[Sh74] W. Shommer, Solid Stat. Commun. **14**, 45 (1974).

[Sh85] M. Shimoji and T. Itami, *Atomic Transport in Liquid Metals* Diffusion and deffect data, Volume 43 (1986).

[Si66] K. S. Singwi and M. P. Tosi, Phys. Rev. **149**, 170 (1966).

[Sm04] S. Mavila Chathoth, A. Meyer, M.M. Koza, F. Juranyi Appl. Phys. Lett. **85**, 4881 (2004).

[Su72] C. T. Sims, N. S. Stoloff and W. C. Hagel, *Superalloys II*, John Wiley and Sons (1972).

[Su90] V. S. Sudovtsev, A. V. Shuvalv and N. O. Shrchina, Rasplavy No.4, 97 (1990).

[St93] U. K. Stolz, I. Arpshofn, F. Sommer and B. Predel, J. Phase Equilib. **14**, 473 (1993).

[To01] A. Tölle, Rep. Prog. Phys. 64, 1473 (2001).

[Ts85a] S. S. Tsao and F. Spaepen, Acta Metall. **33**, 881 (1985).

[Ts85b] S. S. Tsao and F. Spaepen, Acta Metall. **33**, 891 (1985).

[Ts91] K. H. Tsang, S. K. Lee and H. W. Kui, J. Appl. Phys. **70**, 4837 (1991).

[Tu61] D. Turnbull and M. H. Cohen, J. Chem. Phys. **31**, 1164 (1961).

[Tu70] D. Turnbull and M. H. Cohen, J. Chem. Phys. **52**, 3038 (1970).

[Ty84] H. J. V. Tyrrell and K. R. Harris, *Diffusion in Liquids*, Butterworths, London (1984).

[Va65] F. Vachet, P. Desre and E. Bonner, C. R. Acad. Sci. USSR 260, 453 (1965).

[Ve67] L. Verlet Phys. Rev. **159**, 98 (1967).

[Ve72] S. D. Veazey and W. C. Roe, J. Mater. Sci. **7**, 445 (1972).

[Vl74] J. J. van Loef, J. Phys. F **4**, L190 (1974).

[Vr64] A. A. Vertman, A. M. Samarin, E. S. Filippov, Dokl. Akad. Nauk SSSR **155**, 323 (1964).

[Wa75] Y. Waseda and S. Thamaki, Phil. Mag. **32**, 273 (1975).

[Wa77] M. Shimoji, *Liquid Metals*, Academic press, London and New York (1977).

[Wa80] Y. Waseda, *structure of non-crystalline materials : liquids and amorphous solids*, McGraw Hill, New York (1977).

[Wa82] G. Wahnström and L. Sjögren, J. Phys. C **15**, 401 (1982).

[Wi50] D. D. William and R. R. Miller, J. Am. Chem. Soc. **72**, 3821 (1950).

[Wi66] J. R. Wilson, Metall. Rev. **10**, 381, (1966).

[Wi81] C. G. Windsor, *Pulsed Neutron Scattering*, Tayloy and Francis, London (1981).

[Wi94] G. Wilde, G. P. Görler and R. Willnecker, App. Phys. Lett. **65**, 397 (1994).

[Wi93] R. Winter, C. Pilgrim, F. Hensel, C. Morkel, and W. Gläser, J. Non-Cryst. Solids **156-158**, 9 (1993).

[Wi98] G. Wilde, G. P. Görler, K. Jeropoulos, R. Willnecker and H. J. Fecht, Mate. Sci. Forum **269-272**, 541 (1998).

[Wi01] S. R. Williams and W. van Megen, Phys. Rev. E **64**, 041502 (2001).

[Wu95] J. Wuttke, W. Petry, G. Coddens, and F. Fujara, Phys. Rev. E **52**, 4026 (1995).

[Wu96] J. Wuttke, I. Chang, O. G. Randl, F. Fujara, and W. Petry, Phys. Rev. E **54**, 5364 (1996).

[Wu00] J. Wuttke, Phys. Rev. E **62**, 6531 (2000).

[Ya93] T. Yamasaki, S. Kanatani, Y. Ogino and A. Inoue, J. Non-Cry. Solids **156-158**, 441 (1993).

[Yo85] Y. Nishi and A. Yoshihiro, Scripta Metallurgica **19**, 1023 (1985).

[Zo95] R. Zorn, A. Arbe, J. Colmenero, B. Frick, D. Richter and U. Buchenau, Phys. Rev. E **52**, 781 (1995).

[Zo03] V. Zöllmer, K. Rätzke, F. Faupel and A. Meyer, Phys. Rev. Lett. **90**, 195502 (2003).

[Zu01] Th. Zumkley, V. Naundorf, M.-P. Macht, and G. Frohberg, Scr. Mater. **45**, 471 (2001).